

TECHNICAL UNIVERSITY OF CRETE
SCHOOL OF ELECTRICAL AND COMPUTER ENGINEERING
ELECTRONICS LABORATORY



Spectral Cube Reconstruction From Multiplexed Spatial and Spectral Data

by

Ioannis Gkouzionis

*A THESIS SUBMITTED IN PARTIAL FULFILLMENT OF THE REQUIREMENTS
FOR THE DIPLOMA OF ELECTRICAL AND COMPUTER ENGINEERING*

Thesis Committee

Professor Balas Constantinos, *Thesis Supervisor*

Assistant Professor Samoladas Vasileios

Dr. Kortsalioudakis Nathanail

Chania, September 2017

Abstract

Hyper-spectral imaging is a non-destructive detection technology that integrates conventional imaging and spectroscopy to get both spatial and spectral information of a target. This technique has in recent times become a powerful tool for scientific and industrial analysis in many different fields. Its applications range from aerial agricultural surveillance, through food safety and forensics to space exploration and biomedical applications. Hyper-spectral images represent observations of a scene at many different wavelengths and most importantly associate to each pixel in the imaged scene a full spectral vector or spectral signature. The work presented in this thesis deals with a new method in acquiring and reconstructing the spectral cube in hyper-spectral imaging. The method employs a linearly variable band-pass optical filter, which is translated over the image sensor's area. That way, the sensor's pixel columns acquire optical information captured at different wavelengths at a time. By translating the variable filter, all the spectral bands are captured by the sensor's pixels in time sequence. After completing the acquisition process of the spectral cube, the spatial and spectral information are stored in a multiplexed fusion. The next step is to disentangle the multiplexed information, so that the spectral cube to contain a stack of images each one captured at a different wavelength. Two methods for the reconstruction of the spectral cube were implemented and analyzed in the present diploma dissertation. The first one is based on image interpolation, while the second one is based on the diagonal connection of the spectral bands (tomographic reconstruction). Image interpolation refers to the estimation of intensity values at unknown locations, while tomographic reconstruction relies on the resampling of the stored data with the aid of geometrical transformations. In this way, we achieve a straightforward de-multiplexing of the dataset and the reconstructed spectral cube consists of hundreds of narrow band spectral images. The above features make our approach suitable in demanding spectral imaging applications, such as microscopic images and non-destructive analysis.

Acknowledgements

It is a great opportunity to bestow my heartfelt regards to all people who have been either directly or indirectly involved in the fulfillment of this diploma dissertation.

First and foremost, I would like to express my sincerest gratitude to my professor and supervisor, Professor Constantinos Balas, for giving me the opportunity to deal with such an interesting topic. Not only did he help me completing my studies, but also motivated me to work more efficiently and professionally by conducting a lot of extra research, being familiar with experimental devices and gaining valuable knowledge.

Besides my supervisor, I would like to thank the rest of my thesis committee: Assistant Prof. Vasilis Samoladas and Dr. Nathanail Kortsalioudakis, for their insightful comments and encouragement, but also for the hard question which incited me to widen my research from various perspectives.

My sincere thanks also goes to the whole team of the “Optoelectronics & Imaging Diagnostics Lab”, whose contribution and support have been instrumental. I am really grateful to Tsapras Athanasios (PhD Candidate) for his invaluable help and cooperation, his time, advice and support through the research and implementation of this diploma thesis. I would also like to thank Kastrinakis Marios (Postgraduate Student), Papathanasiou Athanasios (Postgraduate Student), and Vardoulakis Emmanouil (Postgraduate Student) for their numerous brainstorming discussions, and selfless advice.

Finally, I must express my very profound gratitude to my beloved parents, Thanasis and Vasiliki, and my sister, Maria, for providing me with unfailing support and continuous encouragement throughout my years of study and through the process of researching and writing this thesis. This accomplishment would not have been possible without them.

Contents

Abstract	i
Acknowledgements	ii
List of Figures	vii
List of Tables	xi
1 Introduction	1
1.1 Introduction	1
1.2 Thesis Outline	2
2 Theoretical Background	3
2.1 Imaging	3
2.2 Spectroscopy	4
2.2.1 Electromagnetic Spectrum	5
2.2.1.1 Range of the spectrum	5
2.2.1.2 Visible spectrum	6
2.3 Spectrometry	6
2.4 Spectral Imaging (SI)	7
2.4.1 Spectral Reflectance	9
2.4.2 Spectral Cubes	9
2.4.2.1 Acquisition of hyper-spectral images	11
2.4.2.2 Image sensing modes	13
2.4.3 Color vs. Spectral Imaging	14
2.4.4 Multi-Spectral Imaging	16
2.4.5 Hyper-Spectral Imaging	17
2.4.6 Multi-Spectral vs. Hyper-Spectral Imaging	17
2.5 Hyper-Spectral Analysis	18
2.6 Hyper-Spectral Cameras	18
2.6.1 Hardware Configuration and Calibration	18
2.7 Scanning Spectral Imaging Systems Based on Electronically Tunable Filters	21
2.8 Hyper-Spectral Imaging Applications	22
2.9 Measures of Spectral Similarity	23
2.9.1 Euclidean Distance	23
2.9.2 Root Mean Squared Error (RMSE)	24

2.9.3	Goodness-of-Fit Coefficient (GFC)	24
3	Image Interpolation	25
3.1	Introduction	25
3.2	Background and Concept	26
3.3	Different Interpolation Methods	27
3.3.1	Nearest Neighbor	28
3.3.2	Linear Interpolation	29
3.3.3	Cubic Convolution	30
3.3.4	B-Splines	33
3.3.4.1	Definition of B-Splines	34
3.3.4.2	Cubic B-Splines	35
4	Hyper-Spectral Imager	39
4.1	Detector Response Modeling	39
4.1.1	Methodology	39
4.1.2	Image Acquisition System Model	39
4.1.3	Basics of Interference Filters	41
4.1.3.1	Interference	41
4.1.3.2	Interference Filter Parameters	42
4.2	Image Acquisition System	43
4.2.1	Set Up	43
4.2.1.1	Technical Specifications and Features	44
4.2.2	Calibration and Scanning Procedure	56
5	Spectral Cube Reconstruction Methods	63
5.1	Introduction	63
5.2	Related Work	63
5.3	Tomographic Reconstruction Method	66
5.3.1	Acquired Spectral Cube Images	68
5.3.2	Reconstructed Spectral Cube Images	70
5.4	Reconstruction Method based on Image Interpolation	76
5.4.1	Acquired Spectral Cube Images	77
5.4.2	Reconstructed Spectral Cube Images	79
5.5	Results	93
5.6	Brief Summary	94
6	Hyper-spectral Skin Imaging	95
6.1	Introduction	95
6.2	Tissue Optics Principles	95
6.3	Spectral Imaging for Skin Assessment	99
6.3.1	Cutaneous Melanoma	99
6.3.2	Melanoma Biology	100
6.4	Experimental Procedure	101
6.4.1	Acquired Spectral Cube Images	102
6.4.2	Reconstructed Spectral Cube Images	103
6.5	Results	105

7 Conclusion and Future Work	107
A Algorithms	109
A.1 Reconstruction Algorithm based on Diagonal Connection of Spectral Bands . . .	109
A.2 Reconstruction Algorithm based on Image Interpolation	110
Bibliography	115

List of Figures

2.1	How spectroscopy works	5
2.2	Electromagnetic spectrum showing the visible light region.	6
2.3	Hyper-spectral Cubes	10
2.4	Schematic representation of a hypercube showing the relationship between spatial and spectral dimensions.	11
2.5	Schematic diagram of hyper-spectral image (hyper-spectral cube) for a piece of fish fillet.	12
2.6	The file layout of the: (A) BSQ, (B) BIL, and (C) BIP interleave.	13
2.7	Acquisition approaches of hyper-spectral images and image sensing modes	14
2.8	Image data capturing and representation in color (a-c) and spectral (d-f) cameras	15
2.9	Spectral imaging opens one new dimension	16
2.10	Multi-Spectral vs. Hyper-Spectral Imaging	17
2.11	Typical spectral imaging techniques. (A) Whishbroom. (B) Pushbroom. (C) Staring. (D) Snapshot.	20
2.12	Linearly Variable Filters	21
2.13	Design principle of standard and Linearly Variable Filters	22
3.1	Interpolation of a single point	26
3.2	Two processes of resampling	27
3.3	Nearest neighbor interpolation	28
3.4	Linear interpolation	30
3.5	Cubic convolution: (a) kernel, (b) Fourier transform	33
3.6	The centered B-splines of degree 0 to 3	35
3.7	Cubic B-spline interpolation	36
3.8	Cubic B-spline interpolation (a=-1.3)	37
3.9	Cubic B-spline interpolation (a=-0.5)	37
4.1	Schematic view of the image acquisition process. The camera response depends on the spectral sensitivity of the sensor, the spectral transmittance of the filter and optical path, the spectral reflectance of the objects in the scene, and the spectral radiance of the illumination.	40
4.2	Interference at a thin layer	42
4.3	Interference filter parameters	43
4.4	Optical elements	44
4.5	The HSI system	44
4.6	Sofradir-EC	44
4.7	Linearly Variable Filter	45
4.8	Linear Dispersion	46

4.9	Transmission characteristics of linearly variable band-pass filter.	47
4.10	Blocking characteristics of linearly variable band-pass filter.	47
4.11	ZWO ASI178MM Monochrome Astronomy Camera	48
4.12	Mono 178 sensor Relative QE Curve	49
4.13	Read noise, full well, gain and dynamic range for ASI178	50
4.14	Halogen OSL1-EC Fiber Light Source	51
4.15	Halogen OSL1-EC Emission Diagram	51
4.16	Liquid Light Guide	52
4.17	Principle of the Liquid Light Guide	52
4.18	Spectral Characteristics of Liquid Light Guides	53
4.19	Specifications of Liquid Light Guides	53
4.20	Color Checkers	54
4.21	X-Rite ColorChecker [®] Patch Targets Numbering	55
4.22	Cross sectional sketch of the proposed HSI system. Each strip of the image on the 1 st image plane is filtered by the LVF. The filtered images are reproduced on the sensor by the relay lens. The whole spectrum is reconstructed strip by strip as the LVF translates.	56
4.23	Relay lens. The symmetry of the layout of the relay lens leaves unaltered the image quality at the 2 nd image plane on the image sensor.	57
4.24	The image-matrix sensor and the two outermost positions of the LVF. Each column of the image sensor colliding on a LVF strip is filtered at a selected wavelength depending on the filter position.	57
4.25	Objective (C-mount) lens. The objective lens creates an image of a scene where it has to provide almost uniform. This is achieved with almost parallel, to the optical axis, off-axis chief ray directions. Besides good correction of aberrations in the visible light, the lens must be well corrected for distortion, to accomplish pixel correspondence on the image.	58
4.26	X-Rite ColorChecker [®] patch targets of scanning procedure.	59
4.27	Acquisition mode - Scanning procedure	60
4.28	Acquisition mode - Capture spectral image at preferred wavelength	60
4.29	View mode - View preferred acquired spectral image	61
4.30	View mode - View acquired spectral cube & spectra per pixel	61
5.1	MDN spectral reflectance curve estimation	65
5.2	Schematic Diagonal (Tomographic) Reconstruction of Spectral Cube.	67
5.3	Acquired spectral images \mapsto 5 nm tuning step.	68
5.4	Acquired spectral images \mapsto 10 nm tuning step.	69
5.5	Reconstructed spectral images from 5.3 acquired spectral images with tomographic reconstruction.	70
5.6	Spatial profiles of a row for the red patch target from 5.3 with tomographic reconstruction.	71
5.7	Reference and estimated spectra from 5.3 with tomographic reconstruction.	72
5.8	Reconstructed spectral images from 5.4 acquired spectral images with tomographic reconstruction.	73
5.9	Spatial profiles of a row for the red patch target from 5.4 with tomographic reconstruction.	74
5.10	Reference and estimated spectra from 5.4 with tomographic reconstruction.	75
5.11	Acquired spectral images \mapsto 5 nm tuning step.	77

5.12	Acquired spectral images \rightarrow 10 nm tuning step.	78
5.13	Reconstructed images from 5.11 acquired spectral images with linear interpolation.	79
5.14	Spatial profiles of a row for the red patch target from 5.11 with linear interpolation.	80
5.15	Reference and estimated spectra from 5.11 with linear interpolation.	81
5.16	Reconstructed images from 5.11 acquired spectral images with spline interpolation.	82
5.17	Spatial profiles of a row for the red patch target from 5.11 with spline interpolation.	83
5.18	Reference and estimated spectra from 5.11 with spline interpolation.	84
5.19	Reconstructed images from 5.12 acquired spectral images with linear interpolation.	85
5.20	Spatial profiles of a row for the red patch target from 5.12 with linear interpolation.	86
5.21	Reference and estimated spectra from 5.12 with linear interpolation.	87
5.22	Reconstructed images from 5.12 acquired spectral images with spline interpolation.	88
5.23	Spatial profiles of a row for the red patch target from 5.12 with spline interpolation.	89
5.24	Reference and estimated spectra from 5.12 with spline interpolation.	90
5.25	Acquired (a-c) & reconstructed (d-f) spectral images of the red patch target	91
5.26	Reference vs. Estimated Spectra. RMSE=0.015, GFC=0.9994	91
5.27	Spatial profiles of a row for the red patch target with linear interpolation	92
5.28	Flowchart of the HSI implementation	94
6.1	The composition of epidermis	96
6.2	The composition of dermis	97
6.3	Absorption spectra of skin constituents	97
6.4	The penetration of light of different wavelengths in the skin	98
6.5	The stages of melanoma development	101
6.6	Acquired spectral images \rightarrow 10 nm tuning step.	102
6.7	Reconstructed images from 6.6 acquired spectral images with linear interpolation.	103
6.8	Reference and estimated spectra from 6.6 with linear interpolation.	104

List of Tables

2.1	Characteristic parameters of a spectral imaging system.	4
4.1	Sofradir-EC Specifications	45
4.2	Linearly Band-pass Filter Specifications	46
4.3	ZWO ASI178MM Camera Technical Specifications	49
4.4	Halogen OSL1-EC Fiber Light Source Specifications	51
4.5	X-Rite ColorChecker [®] Specifications	55
4.6	X-Rite ColorChecker [®] SG Specifications	55

To my family...

Chapter 1

Introduction

1.1 Introduction

Spectral imaging combines spectroscopy and imaging. Each of these fields is well developed and is being used intensively in many fields including life sciences. The combination of these two is, however, not trivial, mainly because it requires creating a three-dimensional (3D) data set that contains many images of the same object, where each one of them is measured at a different wavelength. It also means that the total acquisition time is long, which stands in contrast to the requirements of many biomedical applications. Therefore, compromises must be made for high quality images in a limited amount of time.

The task assigned to this thesis does require an innovative reconstruction of the three-dimensional data structure, known to us, as spectral cube (see [2.4.2](#)). This kind of spectral cube is going to result from the spectral distinction in the images provided by a hyper-spectral scanning procedure. This form of distinction aims at creating a set of images, where each one responds to a specific rather than multiple spectral bands. Although it may seem to be a simple task to deal with, there is a wide variety of aspects to be implemented and factors that must be taken into consideration, in order to provide an efficient solution. The diversity of activities that has to be covered gives a multilateral potential to the nature of the required work.

First of all, a spectral cube is consisted of a great number of images captured in very close narrow bands. These images are acquired by the hyper-spectral imaging system, which is available at the Optoelectronics & Imaging Diagnostics Laboratory. After having successfully acquired the images, which must be noiseless and well focused, from the experimental set up, we proceed with the reconstruction of the spectral cube. Being more specific, the reconstruction refers to the acquisition of a new set of images, in which a single one wavelength is represented by each one of the new reconstructed images.

1.2 Thesis Outline

Chapter 2 provides general information about the theoretical background of the problem, including spectroscopy and spectral imaging.

In Chapter 3 we discuss the most commonly used image interpolation methods.

Chapter 4 deals with the problem specifications, such as the modeling of the proposed acquisition system as well as the hardware devices used for the experimental process and their technical specifications.

Chapter 5 is the most important one, because it consists of a summary of previous work, the two reconstruction methods that implemented in this thesis and the results obtained from them. A plethora of figures are provided to cover the topic.

In Chapter 6 we present a medical application of hyper-spectral imaging, and specifically we use the reconstruction algorithms presented in Chapter 5 to reconstruct a spectral cube we got from human nevi.

In Chapter 7 we summarize the conclusions we were guided towards and the possible future research directions on the problem.

Finally, Appendix A includes source code that provides additional information to topics covered in this report.

Chapter 2

Theoretical Background

For explaining the characteristics of spectral imaging, it is better to start with an introduction of the two elements of spectral imaging; imaging and spectroscopy.

2.1 Imaging

Imaging is the representation or reproduction of an object's form; especially a visual representation (i.e., the formation of an image). At this time, digital imaging is the most advanced and applicable method where data are recorded using a digital camera, such as a charged coupled device (CCD).

In biological studies, the images can be captured either by common optical methods, such as optical microscopy, or by more advanced methods that provide additional physical or chemical information about the objects; examples include optical coherence tomography and life-time imaging. Because of the broad usage of imaging, we limit the following discussion to optical microscopy, mainly in the visible-light range of the electromagnetic spectrum.

The amount of information that can be extracted from an image is determined by the quality of it, and the following list describes the most common parameters that characterize the acquired images.

- **Spatial resolution** determines the closest distinguishable features in the objects. It depends mainly on the wavelength (λ), the numerical aperture (NA) of the objective lens, the magnification, and the pixel size of the array-detector, usually a CCD camera. The latter two play an important role because they determine the sampling frequency which must be sufficiently high to achieve full resolution. Spatial resolution also depends on the signal quality.

- Lowest detectable signal depends on the **quantum efficiency** of the detector (the higher the better), the **noise level** of the system (the lower the better), the **NA** (numerical aperture) of the optics (the higher the better), and the **quality** of the optics.
- **Dynamic range** of the acquired data determines the number of different intensity levels that can be detected in an image. It depends on the maximal possible number of electrons at each pixel and on the lowest detectable signal (basically it is the ratio of these two values). If, however, the measured signal is low, so that the CCD well associated with a pixel is only partially filled, the dynamic range will be limited accordingly. As an example, if a CCD well is fulfilled to only 10% of its maximum capacity, the dynamic range will be reduced to 10% of its nominal value.
- **Field of view (FOV)** determines the maximal area that can be imaged.
- Other parameters include the exposure time range (usually determined by the detector) and the binning of the CCD pixels to gain sensitivity (by trading-off spatial resolution).

See Table 2.1 for a summary and typical parameters values.

<i>Category</i>	<i>Property</i>	<i>Typical</i>
Imaging	Spatial resolution	250 nm (in plane) at $\lambda = 500$ nm
	Field of view	~ 50 μm (high magnification)
	Dynamic range	8 – 16 bits (256 – 65,536 intensity levels)
	Lowest detectable signal	Shot-noise limited
Spectroscopy	Spectral resolution	1 – 20 nm (may depend on λ)
	Spectral range	400 – 900 nm

Table 2.1: Characteristic parameters of a spectral imaging system.

2.2 Spectroscopy

If it had been for a single scientific term that could thoroughly describe the topic of this project, that would be **spectroscopy**¹. Spectroscopy responds to the field of study including the interaction between matter and radiated energy. Historically, it is originated from the dispersion of visible light according to its wavelength. Later on, the concept was greatly expanded to comprise any interaction with radiative energy as a function of its wavelength (λ) or frequency (ν). As a result, the definition of spectroscopy was expanded to an alternative field, that one of frequency ν . A further extension added energy (E) as a variable, due to the equation $E = h \cdot \nu$. Spectroscopic data is often represented by a spectrum, meaning the plot of the response in proportion of wavelength or frequency.

¹http://loke.as.arizona.edu/~ckulesa/camp/spectroscopy_intro.html

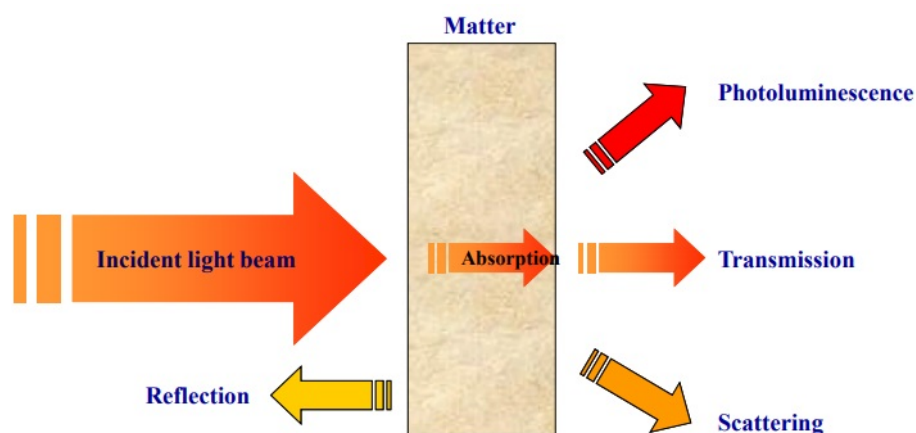


Figure 2.1: How spectroscopy works

As it has been mentioned above, spectroscopy is strictly associated with the measurement of radiation intensity with reference to the wavelength or frequency. This sort of measurements can be conducted by experimental spectroscopic devices such as spectrometers, spectrophotometers, spectrographs or spectral analyzers.

2.2.1 Electromagnetic Spectrum

The **electromagnetic spectrum** is the complete range of the wavelengths of electromagnetic radiation, beginning with the longest radio waves (including those in audio range) and extending through visible light (a very small part of the spectrum) all the way to the extremely short gamma rays that are a product of radioactive atoms. Visible light lies toward the shorter end, with wavelengths from 400 to 700 nanometers. Nearly all types of electromagnetic radiation can be used for spectroscopy, to study and characterize matter.

2.2.1.1 Range of the spectrum

Electromagnetic waves are typically described by any of the following three physical properties: the frequency f , wavelength λ , or photon energy E . Wavelength is inversely proportional to the wave frequency, so gamma rays have very short wavelengths that are fractions of the size of atoms, whereas wavelength on the opposite end of the spectrum can be of thousand kilometers. Photon energy is directly proportional to the wave frequency, so gamma ray photons have the highest energy (around a billion electron volts), while radio wave photons have very low energy (approximately a femtoelectronvolt). These relations are illustrated by the following equations:

$$f = \frac{c}{\lambda}, \text{ or } f = \frac{E}{h}, \text{ or } E = \frac{hc}{\lambda} \quad (1.1)$$

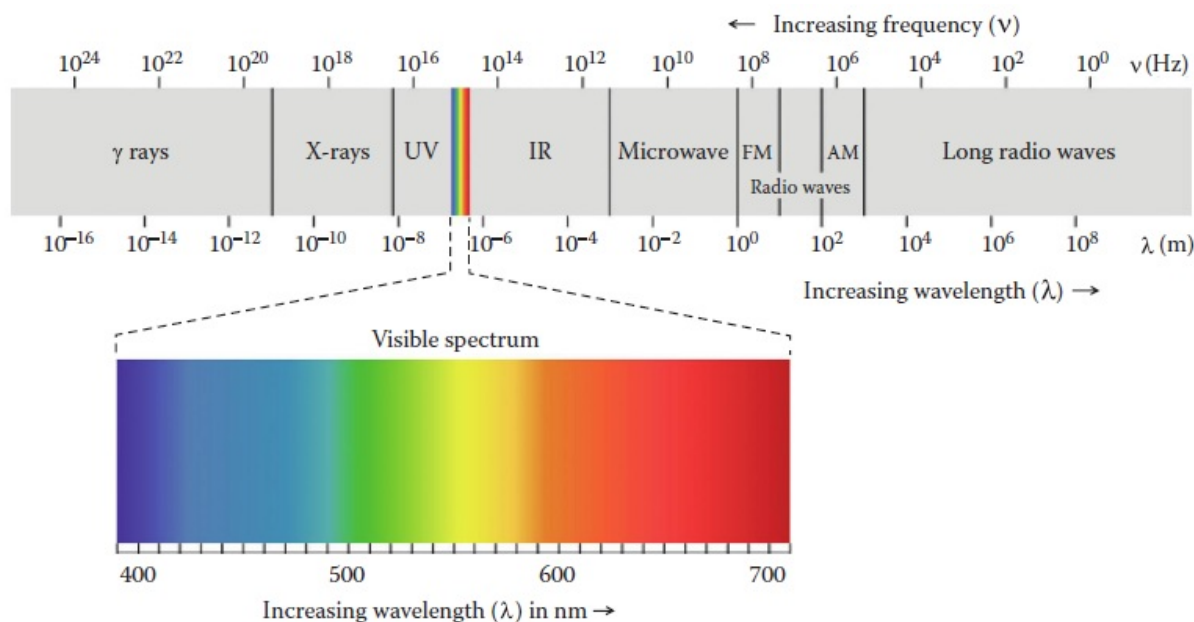


Figure 2.2: Electromagnetic spectrum showing the visible light region.

The behavior of EM radiation depends on its wavelength. When EM radiation interacts with single atoms and molecules, its behavior also depends on the amount of energy per quantum (photon) it carries.

2.2.1.2 Visible spectrum

The **visible spectrum** is the part of the electromagnetic spectrum that is visible to the human eye. Electromagnetic radiation with a wavelength between 390 nm and 700 nm is detected by the human eye and perceived as visible light.

2.3 Spectrometry

Spectrometry constitutes the technique that is being used so as to assess the concentration or amount of a specific chemical compound. It is a common practice to combine spectrometry along with spectroscopy, mentioned above, in physical and analytical chemistry for the identification of substances through the spectrum either emitted from or absorbed by them. In addition, they contribute to the field of astronomy and remote sensing as well. The majority of large telescopes is equipped with spectrometers, since the last ones have been instrumental to measurements, as far as chemical compositions and natural properties of astronomical objects are concerned.

2.4 Spectral Imaging (SI)

Spectral imaging is a combination of spectroscopy and photography in which a complete spectrum or partial spectral information (such as the Doppler shift or Zeeman splitting of a spectral line) is acquired at each position of an image plane. Spectral imaging allows extraction of additional information the human eye fails to capture with its receptors for red, green and blue. Applications related to astronomy, solar physics, analysis of plasmas in nuclear fusion experiments, planetology, and Earth remote sensing are sparked by the benefits of spectral imaging.

Various distinctions among techniques are applied, based on criteria including spectral range, spectral resolution, number of bands, width and contiguousness of bands, and application. The terms include **Multi-Spectral Imaging** (see 2.4.4), **Hyper-Spectral Imaging** (see 2.4.5), full spectral imaging, imaging spectroscopy or chemical imaging. These terms are seldom applied to the use of only four or five bands that are all within the visible light range.

Important new developments in the field of Biomedical Optical Imaging (OI) allow for unprecedented visualization of tissue microstructure and enable quantitative mapping of disease-specific endogenous and exogenous substances [1]. Spectral imaging (SI) is one of the most promising OI modalities, belonging to this general field, and it will be reviewed in more detail in this section of chapter 1.

A spectral imager provides spectral information at each pixel of an image sensor array. The SI systems acquire a three-dimensional (3D) data set of spectral and spatial information, known as spectral cube. The spectral cube can be considered as a stack of images, each of them acquired at a different wavelength. Combined spatial and spectral information offers great potential for the non-destructive/invasive investigation of a variety of studied samples.

Spectroscopy finds application in analytical chemistry since a long time. Different spectroscopy types and modalities exist, depending on the optical property that it is intended to be measured, namely, absorption, spontaneous emission (fluorescence, phosphorescence), scattering (Rayleigh elastic, Raman inelastic) spectroscopy, etc. As the light travels into the sample, photons are experiencing absorption, which may result in fluorescence emission and multiple scattering due to the local variation of the index of refraction. Spectrometers measure the intensity of the light emerging from the sample as a function of the wavelength. The collected light passes through a light-dispersing element (grating), which spatially splits the light wavelengths onto the surface of an optical sensor array, interfaced with a computer for recording and processing the spectrum. Sample illumination can be provided by either a broadband (e.g., white light) or a narrow-band light source. In the first case, the measured spectra provide information for the absorption and scattering characteristics of the tissue. In the second case, the measured spectra probe the fluorescence characteristics of the sample. Particularly, in steady-state fluorescence

spectroscopy, a narrow-band light source is used for fluorescence excitation, such as lasers, LEDs, or filtered light sources, emitting typically in the blue-ultraviolet band. A sensitive optical sensor is used for collecting the emission spectra [2].

The collected emission spectra can provide diagnostic information for the composition of the sample. This makes spectroscopy an indispensable tool for non-destructive analysis and for the development of novel, non-invasive diagnostic approaches. Particularly, in biomedical sciences, *the diagnostic potential of tissue spectroscopy is based on the assumption that the absorption, fluorescence, and scattering characteristics of the tissue change during the progress of the disease.*

Over the last 20 years, spectroscopy has been extensively investigated as a tool for identifying various pathologic conditions on the basis of their spectral signatures. It had been demonstrated that spectroscopy can successfully probe intrinsic or extrinsic chromophores and fluorophores, the concentration of which changes during the development of the disease. In its conventional configuration, spectroscopy uses single-point probes that cannot easily sample large areas or small areas at high spatial resolution (SR). It is obvious that this configuration is clearly suboptimal when solid and highly heterogeneous materials, such as the biological tissues, are examined. In these cases, the collected spectrum is the result of the integration of the light emitted from a great number of area points. This has the effect of mixing together signals originating from both pathologic and healthy areas, which makes the spectral signature-based identification problematic. Looking at the same problem from another perspective, point spectroscopies are considered as inefficient in cases where the mapping of some characteristics, spectrally identifiable property, is of the utmost importance.

Spectroscopy probes optical signals with **high spectral resolution** but with **poor spatial resolution (SR)**. The vastly improved computational power together with the recent technological developments in tunable optical filter and imaging sensor technologies have become the catalysts for merging together imaging and spectroscopy. Both areas, imaging and spectroscopy, continue to be affected by technological innovations that enable faster acquisition of superior-quality data. **SI has the unique feature of combining the advantages of both imaging and spectroscopy (high spatial and spectral resolution) in a single instrument.** In SI, light intensity is recorded as a function of both wavelength and location. In the image domain, the data set includes a full image at each individual wavelength. In the spectroscopy domain, a fully resolved spectrum at each individual pixel can be recorded. These devices can measure the spectral content of light energy at every point in an image. Multiple images of the same scene at different wavelengths are acquired for obtaining the spectra. As an example, an SI device integrating an imaging sensor with 1000×1000 pixels provides 1 million individual spectra. A spectrum containing 100 data points results from an equal number of spectral images. Assuming that the intensity in each pixel is sampled at 8 bits, then the size of the resulting spectral cube equals to 100 Mbytes. Due to the huge size of the collected data sets, SI data

processing, analysis, and storage require fast computers and huge mass memory devices. Several mathematical approaches are used for spectral classification and image segmentation on the basis of the acquired spectral characteristics. The spectra are classified using spectral similarity measures, and the resulting different spectral classes are recognized as color-coded image clusters. SI can be easily adapted to a variety of OI instruments such as camera lenses, telescopes, microscopes, endoscopes, etc. For this reason, applications of SI span from earth observation including ground and atmosphere (remote sensing) to general medicine and molecular biology [1].

2.4.1 Spectral Reflectance

It has already been mentioned how materials print a spectral signature on the light they reflect. In order to get this signature, a parameter called **spectral reflectance** is of interest. It represents the ratio between reflected and incident light, as a function of wavelength. This dependence is due to the fact that light is scattered or absorbed to different degrees at certain wavelengths, and it exists for almost every material.

There are several physical processes involved that determine the nature of the reflected light, and thus, the spectral signature of the material. In the first place, almost every object shows some degree of specular reflection, which means that some of the light rebounds directly on the surface of the material, as on a mirror. In this case, the spectrum of the reflected light remains the same as that of the incident light. There is no signature printed. In the second place, part of the light diffuses into the material where some is absorbed and some is randomly scattered, which is known as diffuse reflection. Finally, fluorescence, which is the emission of light by a substance that has absorbed light or other electromagnetic radiation, may also take place. In this case, a photon at shorter wavelength is absorbed and a photon at longer wavelength is emitted consequentially.

A white-colored material, for example, does not absorb any wavelength while a multi-colored material will absorb some wavelengths and diffusely reflect others. These reflected wavelengths are responsible for the color of the material. In a way, they shape the nature of the incident light to create what we perceive as color. This effect can be thought from the continuous spectrum point of view: it explains why matter prints a signature on the incident light depending on how different spectral components of light are absorbed or reflected.

2.4.2 Spectral Cubes

The information that is primarily collected by spectral imagers and then appropriately processed based on the kind of application running, is stored in 3D data structures for further analysis.

This sort of data structures are known as **Spectral Cubes (SC)**. A spectral cube consists of the three dimensional projection of a great number of consecutive and registered sets of hyper-spectral or multi-spectral images. Being more specific, the first two dimensions respond to spatial dimensions, for account of pixel coordinates and the third one refers to spectral dimension, meaning a specific wavelength of the electromagnetic spectrum. A glance at Fig. 2.3a and Fig. 2.3b offer profound perception of how a spectral cube does look like.

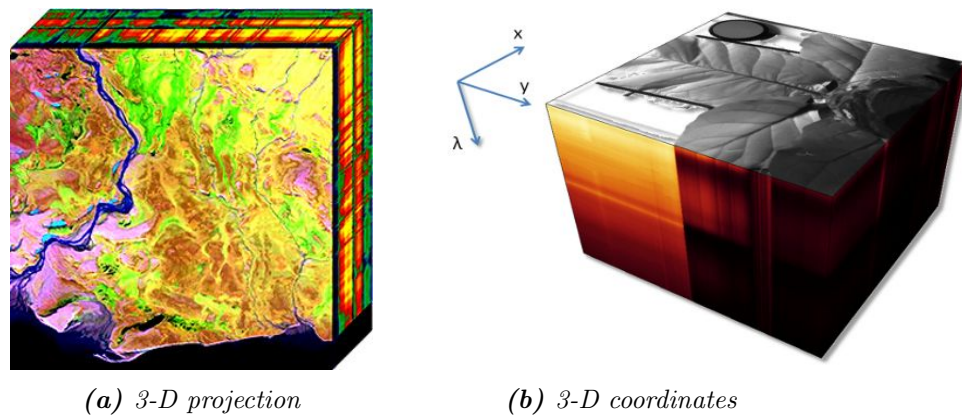


Figure 2.3: *Hyper-spectral Cubes*

Simply put, an imaging spectrometer acquires the spectrum of each pixel in a two-dimensional spatial scene. As shown in Fig. 2.4, the easiest way to think of such a scheme is as band sequential imaging, in which multiple images of the same scene at different wavelengths are acquired. A key point is that the spectra be sampled densely enough to reassemble a spectrum (commensurate with the need for analysis). There are many technological means of obtaining these data. The images are typically stacked in a computer, from the lowest wavelength to the highest, to create an image cube of the data set. The spectrum of a selected pixel is obtained by skewering it in its third dimension, wavelength, as the inset in Fig. 2.4 shows.

As an example, the hyper-spectral cube of a fish fillet acquired using reflectance mode is illustrated in Fig. 2.5. The raw hyper-spectral cube consists of a series of contiguous sub-images one behind each other at different wavelengths (Fig. 2.5.a). Each sub-image provides the spatial distribution of the spectral intensity at a certain wavelength. That means a hyper-spectral image described as $I(x, y, \lambda)$ can be viewed either as a separate spatial image $I(x, y)$ at each individual wavelength (λ), or as a spectrum $I(\lambda)$ at each individual pixel (x, y) . From the first viewpoint, any spatial image within the spectral range of the system can be picked up from the hyper-spectral cube at a certain wavelength within the wavelength sensitivity (Fig. 2.5.b). The gray scale image shows the different spectral intensity of the imaged object at a certain wavelength due to the distribution of its corresponding chemical components. For example, an image within the hypercube at a single waveband centered at 980 nm with bandwidth of 5 nm (Fig. 2.5.b) can relatively show the information of moisture distribution in the fish fillet, which

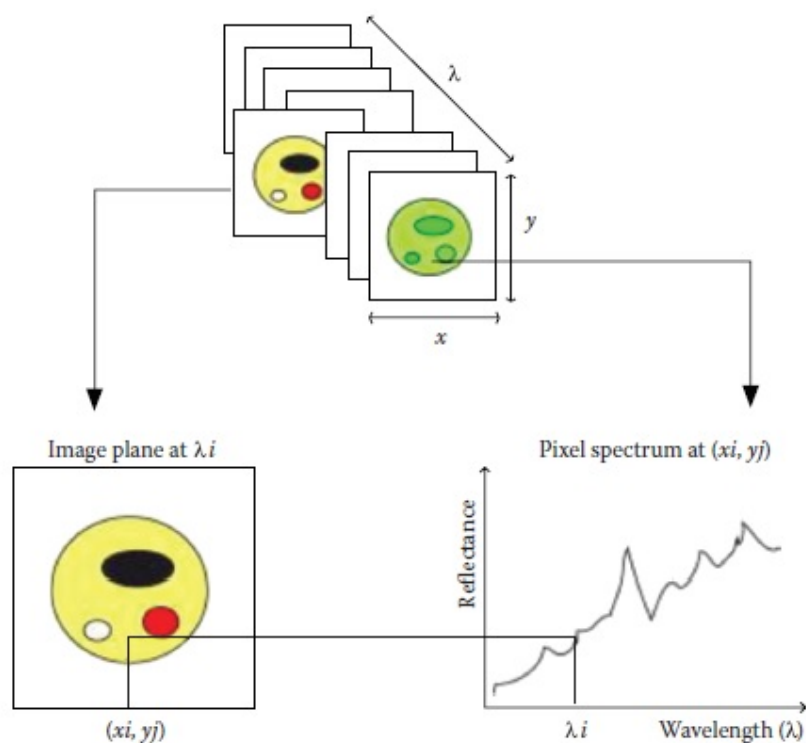


Figure 2.4: Schematic representation of a hypercube showing the relationship between spatial and spectral dimensions.

is difficult to be observed in RGB image (Fig. 2.5.c). From the second viewpoint, the resulting spectrum of a certain position within the specimen can be considered as its own unique spectral fingerprint of this pixel to characterize the composition of that particular pixel (Fig. 2.5.d).

2.4.2.1 Acquisition of hyper-spectral images

There are four approaches to acquire 3-D hyper-spectral image cubes ($I(x, y, \lambda)$), which are **point scanning**, **line scanning**, **area scanning**, and the **single shot** method, as illustrated in the upper half of Fig. 2.7. In the point scanning method (also known as the whiskbroom method), a single point is scanned at one pixel to provide the spectrum of this point (Fig. 2.7.a), and other points are scanned by moving either the detector or the sample along two spatial dimensions (x and y). Its obtained hyper-spectral cube is stored in the band-interleaved-by-pixel (BIP) format. For an image stored in BIP format, the first pixel for all bands is in sequential order, followed by the second pixel for all bands, followed by the third pixel for all bands, etc., interleaved up to the number of pixels. This format is optimal for accessing the spectral information of each pixel. The disadvantages of whiskbroom are very time-consuming for positioning the sample and need advanced repositioning hardware to ensure repeatability. The second approach illustrated in Fig. 2.7.b is called as line scanning method or pushbroom

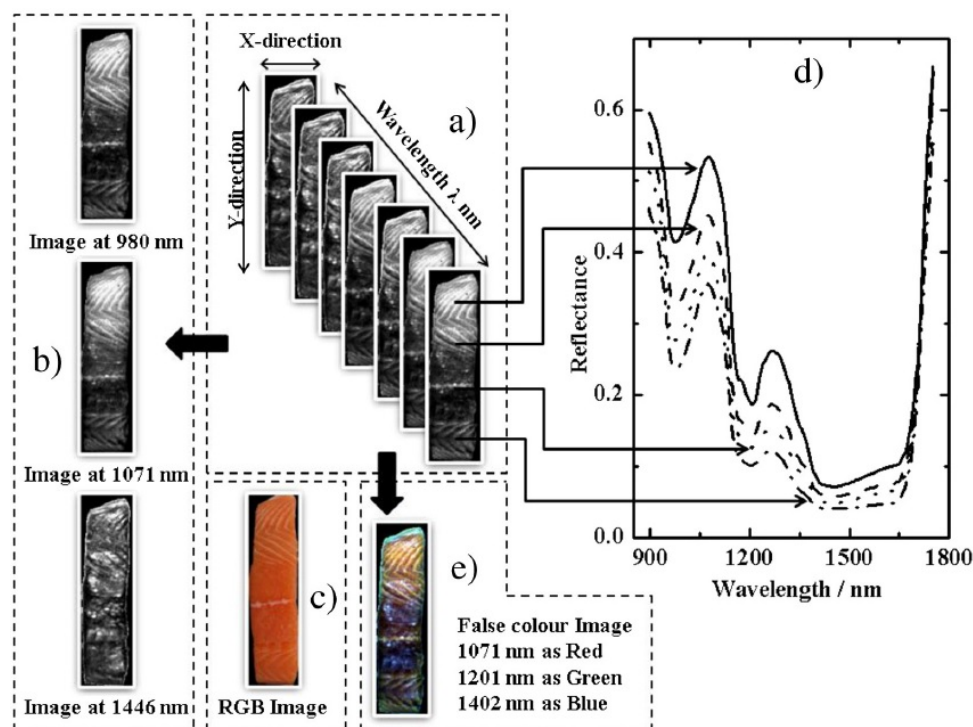


Figure 2.5: Schematic diagram of hyper-spectral image (hyper-spectral cube) for a piece of fish fillet.

method, which records a whole line of an image as well as spectral information simultaneously corresponding to each spatial pixel in the line. A complete hyper-spectral cube can be obtained as the line is scanned along the direction of x dimension (Fig. 2.7.b), and the obtained cube is stored in the format of band-interleaved-by-line (BIL). BIL format is a scheme for storing the pixel values of an image in a file band for each line, or row, of the image. Because of its characteristics of continuous scanning in one direction, line scanning is particularly suitable in conveyor belt systems that are commonly used in food process lines. Therefore, line scanning is the most popular method of acquiring hyper-spectral images for food quality and safety inspection. The disadvantage of the pushbroom technique is that the exposure time can be set at only one value for all wavelengths. Such exposure time has to be short enough to avoid saturation of spectrum at any wavelength, resulting in underexposure of other spectral bands and low accuracy of their spectral measurement.

The above two methods are spatial scanning methods, while the area or plane scanning (also known as band sequential method or wavelength scanning) is a spectral scanning method as illustrated in Fig. 2.7.c. This approach keeps the image field of view fixed and acquires a 2-D monochrome image (x, y) with full spatial information at a single wavelength at a time. Such scanning repeats over the whole wavelength range, results in a stack of single band images stored in the band sequential (BSQ) format. As a simple format, BSQ encodes each line of the image at the first band is followed immediately by the next line in the same spectral band, followed

by the second band for all lines, followed by the third band for all lines, etc., interleaved up to the number of bands. This format provides an easy access of spatial (x, y) access of at a single spectral band. As the detector is exposed to only a single wavelength each time, a suitable exposure time can be set for each wavelength. In addition, the area scanning does not need to move either sample or detector and is suitable for the applications where the object should be stationary for a while, such as excitation-emission in fluorescence imaging. A disadvantage of area scanning is that it is not suitable for a moving sample or the inspection of real-time delivery. At last, the single shot method records both spatial and spectral information using a large area detector with one exposure to capture the images (Fig. 2.7.d), making it very attractive when fast hyper-spectral imaging is required. However, it is still in the early stage of development and has limited resolutions for spatial dimension and narrow ranges for spectral dimension.

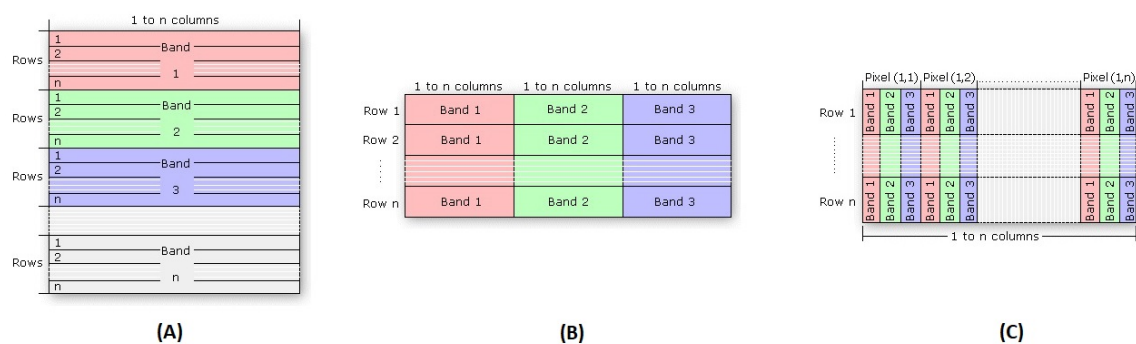


Figure 2.6: The file layout of the: (A) BSQ, (B) BIL, and (C) BIP interleave.

2.4.2.2 Image sensing modes

There are three common sensing modes for hyper-spectral imaging, namely **reflectance**, **transmittance**, and **interactance** as illustrated in lower half of Fig. 2.7. Positions of light source and the optical detector (camera, spectrograph, and lens) are different for each acquisition mode. In reflectance mode, the detector captures the reflected light from the illuminated sample in a specific conformation to avoid specular reflection (Fig. 2.7.e). External quality features are typically detected using reflectance mode, such as size, shape, color, surface texture and external defects. In transmittance mode, the detector is located in the opposite side of the light source (Fig. 2.7.f), and captures the transmitted light through the sample which carries more valuable internal information but is often very weak. Transmittance mode is usually used to determine internal component concentration and detect internal defects of relative transparent materials. However, transmittance mode has a low signal level from light attenuation and is affected by the thickness of sample. In interactance mode, both light source and the detector are located in the same side of sample and parallel to each other (Fig. 2.7.g). On the basis of such setup, the interactance mode can detect deeper information into the sample and has less

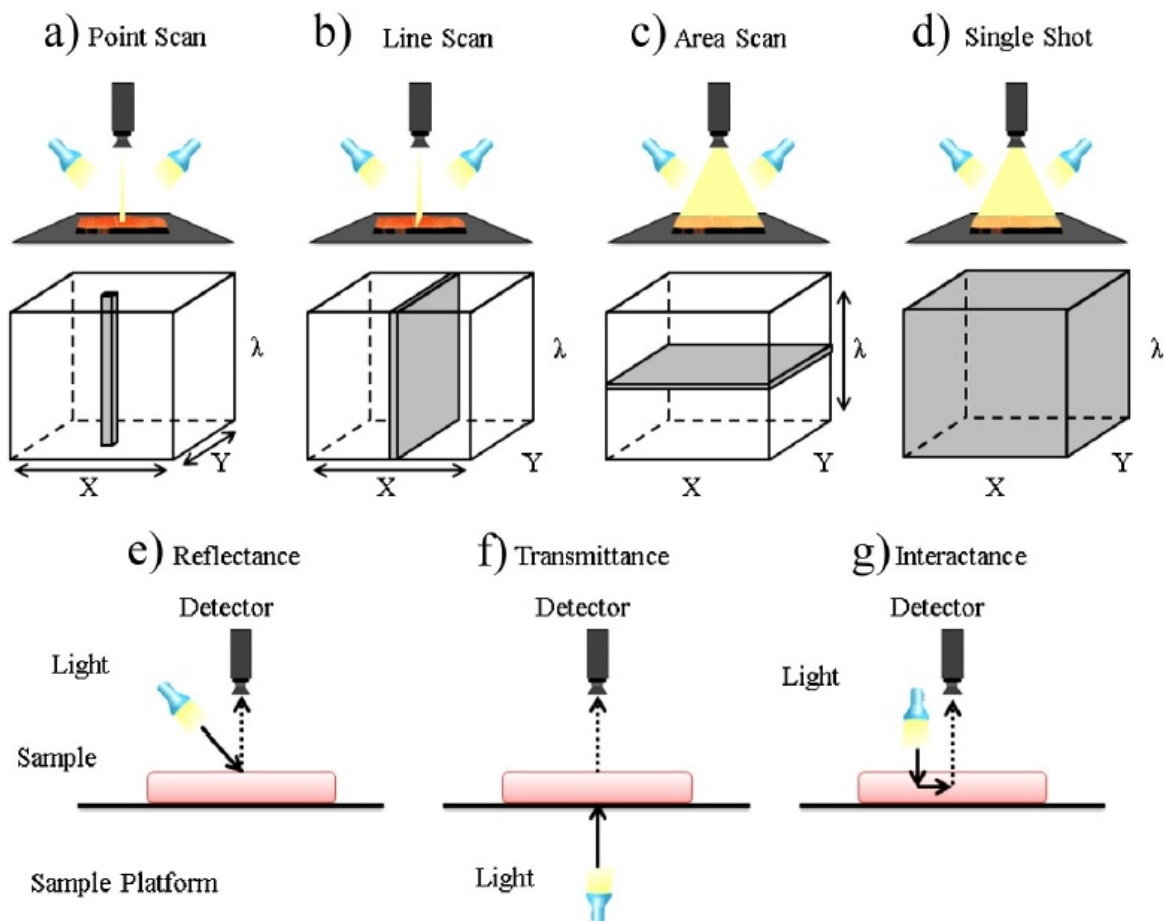


Figure 2.7: Acquisition approaches of hyper-spectral images and image sensing modes

surface effects compared to reflectance mode. Meanwhile, the interactance mode reduces the influence of thickness, which is a practical advantage over transmission. It should be noted that a special setup is required in the transmittance mode to seal light in order to prevent specular reflection directly entering the detector.

2.4.3 Color vs. Spectral Imaging

Photons encountering the pixels of an imaging sensor create electrons in pixel cells (**photoelectric effect**); **thereby, the number of photons is proportional to the number of electrons**. The photon's wavelength information, however, is not “transferred” to the electrons. Hence, unfiltered imaging chips are color blind. Color or SI devices employ optical filters placed in front of the imaging chip. Color imagers use either Si charge coupled devices (CCD) or C-MOS sensors, which are sensitive in the visible and in the near-infrared (NIR) part of the spectrum (400 – 1000 nm). A band-pass filter is used for rejecting the NIR band (700 – 1000 nm). In 3-chip configurations, three photon channels are created with the aid of a thichroic

prism assembly, which directs the appropriate wavelength ranges of light to their respective sensors. Camera electronics combine the red, green, and blue (R, G, B) imaging channels composing a high-quality color image, which is delivered to external devices through an analog or digital interface. An alternative, cheaper, and more popular color camera configuration employs a single chip, where the color filters are spread, similar to a mosaic, across all pixels of the sensor. Due to the fact that each pixel “sees” only one primary color, three pixels are required to record the color of the corresponding area of the object. This reduces significantly the SR of the imager. This unwanted effect is partially compensated with a method called “**spatial color interpolation**” carried out by the camera electronics. The interpolation algorithm estimates the two missing primary color values for a certain pixel by analyzing the values of its adjacent pixels. In practice, even the most excellent color space interpolation methods cause a low-pass effect. Thus, single chip cameras yield images that are more blurred than those of 3-chip or of monochrome cameras. This is especially evident in cases of subtle, fiber-shaped image structures.

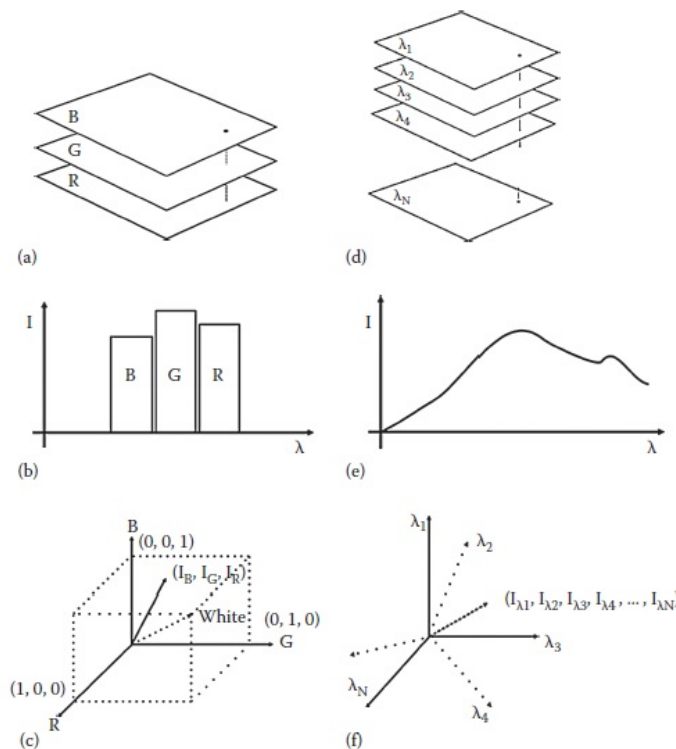


Figure 2.8: Image data capturing and representation in color (a-c) and spectral (d-f) cameras

Color cameras emulate the human vision for color reproduction and are real-time devices since they record three spectral bands simultaneously at very high frame rates. Human vision-emulating color imaging devices usually describe color with three parameters (RGB values), which are easy to interpret since they model familiar color perception processes. They share, however, the limitations of human color vision. Color cameras and human color vision allocate

the incoming light to three color coordinates, thus missing significant spectral information. Due to this fact, objects emitting or remitting light with completely different spectral components can have precisely the same RGB coordinates, a phenomenon known as **metamerism**. The direct impact of the metamerism is the inability of the color imaging systems to distinguish between materials having the same color appearance but different chemical composition. This sets serious limitations to their analytical power and consequently, to their capabilities [1].

Unlike images taken with standard color (RGB) cameras, SI information is not discernible to the human eye. In SI, a series of images is acquired at many wavelengths, producing a spectral cube. Each pixel in the spectral cube, therefore, represents the spectrum of the scene at that point. The nature of imagery data is typically multidimensional, spanning spatial and spectral dimensions (x, y, λ).

A color camera captures typically three images corresponding to the band-pass characteristics of the RGB primary color filters. Color image pixels miss significant spectral information as it is integrated into three, broad spectral bands. The color of a pixel can be represented as vector in a three-dimensional “color space” having the RGB values as coordinates. SI systems collect a stack of pictures, where each image is acquired at a narrow spectral band and all together compose the spectral cube. A complete spectrum can be calculated for every image pixel, which can be otherwise represented as a vector in a “multidimensional spectral space”.

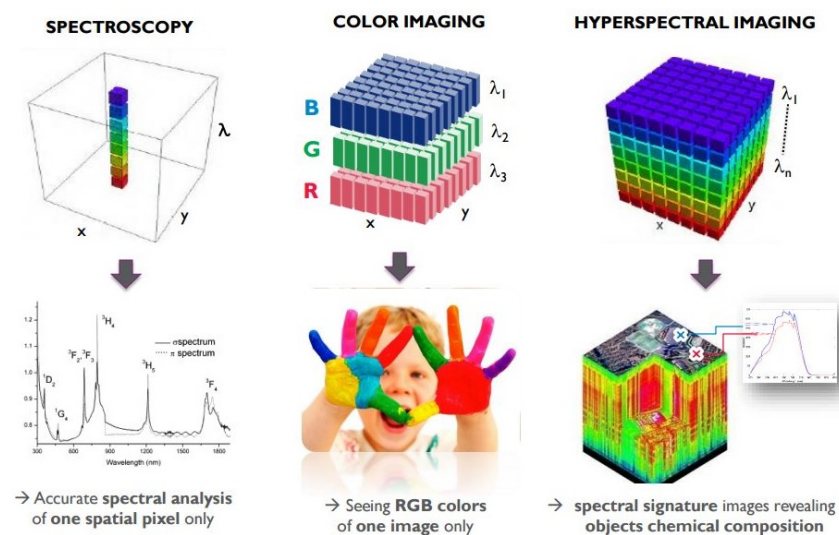


Figure 2.9: Spectral imaging opens one new dimension

2.4.4 Multi-Spectral Imaging

Multi-Spectral Imaging (MI) is responsible for capturing image data at specific frequencies across the electromagnetic spectrum. The wavelengths may be separated by filters or by the

use of instruments that are sensitive to particular wavelengths, including light from frequencies beyond the visible light range, such as infrared. MI images are the main type of images acquired by remote sensing (RS) radiometers. Dividing the spectrum into many bands, MI is the opposite of panchromatic, which records only the total intensity of radiation falling on each pixel. Spectral imaging with more numerous bands, finer spectral resolution or wider spectral coverage may be called **Hyper-Spectral** or **Ultra-Spectral** (see 2.4.5).

2.4.5 Hyper-Spectral Imaging

Hyper-Spectral Imaging (HI) is a technology widely used for remote imaging, so as to extract a maximum of information out of images captured under strongly varying imaging conditions. It provides options for three-dimensional data generation with high spectral resolution across the full electromagnetic spectrum of frequencies, beyond the visible. This visual extension beyond the scope of human eye renders **HI** a powerful analytical tool, which has been extensively used in a wide variety of fields including *agriculture, medicine, artistic* [3], *satellite imaging* [4], *astronomy, surveillance* [5], [6], *chemical imaging, physics and environment* [4].

2.4.6 Multi-Spectral vs. Hyper-Spectral Imaging

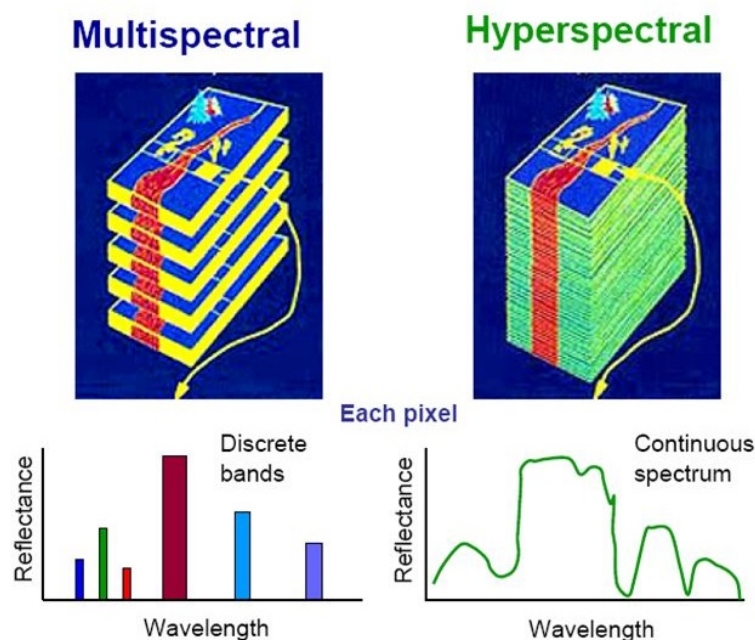


Figure 2.10: Multi-Spectral vs. Hyper-Spectral Imaging

The distinction between **Hyper-Spectral** and **Multi-Spectral** pertains to the number of narrow bands or the type of measurement. **Multi-Spectral** deals with several images at discrete and somewhat narrow bands. Being “discrete and somewhat narrow” is what distinguishes MI

in the visible from color photography. A MI sensor may have many bands covering the spectrum from the visible to the long wave infrared. MI images do not produce the “spectrum” of an object. On the other hand, **Hyper-Spectral** deals with imaging narrow spectral bands over a continuous spectral range, and produce the spectra of all pixels in the scene. So, a sensor with only 20 bands can also be HI when it covers the range from 500 to 700 nm with 20 bands each 10 nm wide. Fig. 2.10 helps us looking at the differences pinpointed above more closely.

2.5 Hyper-Spectral Analysis

Spectral analysis when combined with spatial data adds a significant amount of information that can be used to improve image exploitation and interpretation. To combine spectral information with spatial imagery, the sensor or camera has to be able to create images within the user defined narrow spectral bands rather than the wide-band imagery that the conventional cameras produce. Compared to conventional filter based imaging systems, spectral cameras provide higher spectral and spatial resolution, flexible wavelength selections in software, broader spectral coverage and shorter acquisition times.

2.6 Hyper-Spectral Cameras

Hyper-spectral analysis can be achieved by a hyper-spectral camera system that includes optics, an imaging spectrograph, a camera displaying the spectral information and a software package to display and calculate the results. Hyper-spectral cameras are used to acquire the hyper-spectral target image at tens or hundreds of wavelengths simultaneously. Such developed softwares create new possibilities for imaging applications where spectroscopy methods can be totally attuned to standard and efficient image processing methods. The recorded full spectrum for each pixel of the image can be leveraged to a wide variety of purposes, such as classification, material detection, accurate color calculations or chemometrics over the full range [1].

2.6.1 Hardware Configuration and Calibration

SI camera systems, either HSI or MSI, consist of a monochrome sensor, an electronically controlled spatial or spectral scanning mechanism, imaging optics, and a computer platform for storage, display analysis, and processing of imaging data. Control electronics synchronize the scanning and the data capturing processes, so that a set of spectral images are collected as members of the spectral cube [1].

The number of the spectral bands that an SI system is capable of acquiring determines the distinction between multi-spectral imaging (MSI) and hyper-spectral imaging (HSI). MSI devices typically acquire 5 – 20 spectral bands, while HSI systems acquire up to a few hundreds of spectral bands (see 2.4.5). Ultra-spectral imaging (USI) devices are currently under development with the capacity of acquiring thousands of very narrow spectral bands.

SI systems use monochrome sensors or sensor arrays, which can capture only two of the three spectral dimensions of the spectral cube at a time. To capture the third dimension, spatial or spectral scanning is required. Depending on the method employed for building the spectral cube, SI devices are classified in different categories. The categorization is as follows:

1. **Whiskbroom** SI devices, where a linear sensor array is used to collect the spectrum (λ dimension) from a single point at a time; the other two spatial coordinates are collected with (x, y) spatial scanning.
2. **Pushbroom** SI devices, in which a 2D sensor array is used, the one dimension of which captures the first spatial (x) coordinate and the other the spectral coordinate in each camera frame; the second spatial coordinate (y) is captured with line (slit) scanning.
3. **Staring** SI devices, where a 2D sensor array is coupled with an imaging monochromator, which is tuned to scan the spectral domain and in each scanning step, a full spectral image frame is recorded.

Whiskbroom and Pushbroom imagers utilizing spatial scanning for building the spectral cube do not provide live display of spectral images, since they are calculated from the spectra after the completion of the spatial scanning of the corresponding area. Staring imagers, on the other hand, are based on the tuning of the imaging wavelength and the spectra are calculated from the spectral cube composed by the spectral images that are captured in time sequence. Compared to the other approaches, staring imagers have the advantage of displaying live spectral images, which is essential for aiming and focusing.

Selecting the SI camera optimal configuration and components requires a “systems” approach. The intended application determines the SI system’s spectral range and resolution. Si CCD detectors can be used to cover the spectral range ultraviolet (UV), visible and NIR up to 1 μm . InGaAs detectors are suitable for the up to 1.7 μm NIR range. For longer infrared wavelengths, HgCdTe or InSb cameras must be used. Ideally, the wavelength range of the monochromators should match at least a significant part of the spectral range within which the selected detector is sensitive. Narrow-band imaging and monochromator optics reduce the overall light throughput of an SI system. Moreover, the light throughput of the monochromator depends on the wavelength. Furthermore, the quantum efficiency (QE) of the detector also changes with the wavelength.

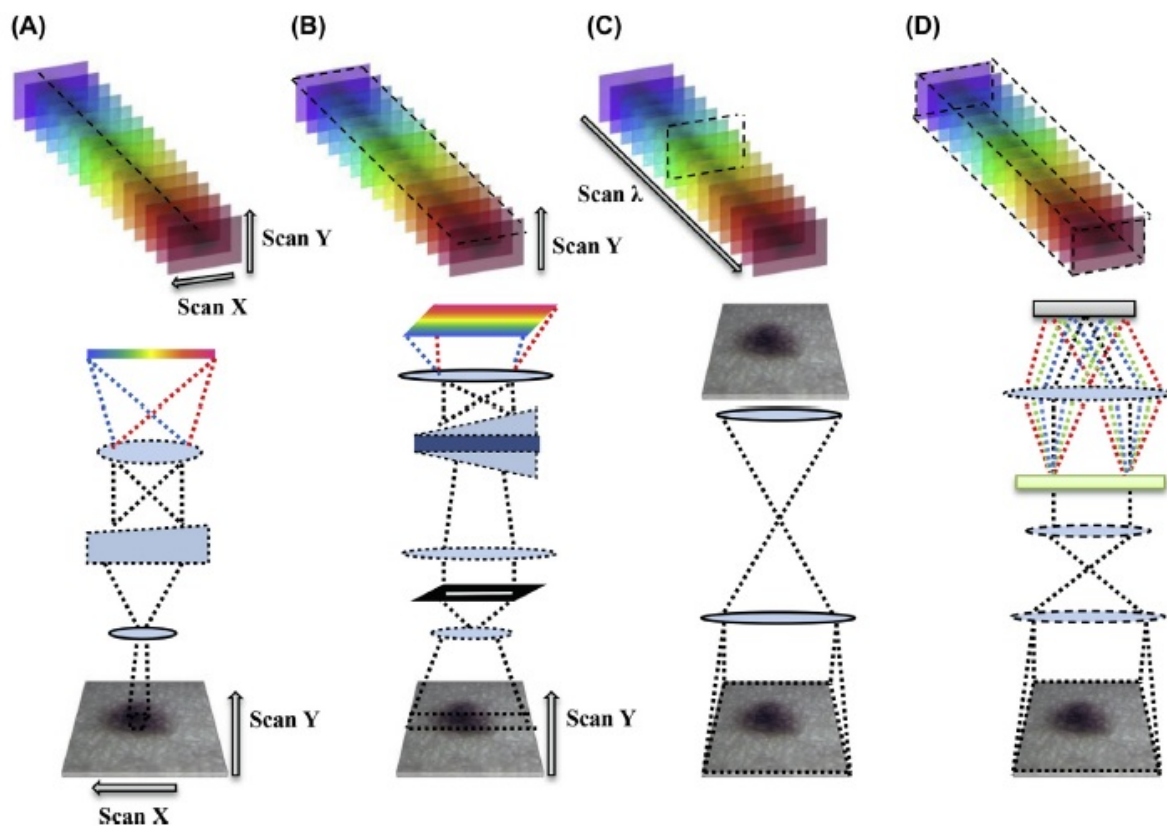


Figure 2.11: Typical spectral imaging techniques. (A) Wishbroom. (B) Pushbroom. (C) Staring. (D) Snapshot.

Appropriate calibrations for a hyper-spectral imaging system are essential to ensure the reliability of the acquired hyper-spectral image data and to guarantee the consistent performance of the system. Even if the environment of data measurement is carefully controlled, inconsistent spectral profiles of reference spectra may be acquired by some systems. Therefore, it is necessary to eliminate this variability by using a standardized and objective calibration, and a validation protocol. The goals of calibration process are to standardize the spectral and spatial axes of the hyper-spectral image, validate the acceptability and reliability of the extracted spectral and spatial data, determine whether the hyper-spectral imaging system is in running condition, evaluate accuracy and reproducibility of the acquired data under different operating conditions, and diagnose instrumental errors if necessary.

SI system's calibration is very essential in order to achieve "device-independent" spectral measurements. Calibration can be performed with the aid of a reference sample displaying a known or a flat spectrum over the entire operating wavelength range. A calibration curve or a lookup table can be obtained by comparing the known spectral characteristics of the calibration sample with that measured by the SI system spectra. Image brightness can be corrected on the basis of the calibration data, after spectral image acquisition. The calibration curve or the lookup table can also be integrated into the system's software for controlling the detector's exposure time

during image acquisition, in all tuning steps of the filter. By changing the detector's exposure or gain settings, the wavelength dependence of the SI system's response is compensated and the spectral images that are acquired and captured are calibrated [1].

2.7 Scanning Spectral Imaging Systems Based on Electronically Tunable Filters

Spectral scanning SI systems can be categorized on the basis of the technological approaches employed for tuning the imaging wavelength. Two general classes of devices can be defined depending on whether their imaging monochromator contains or not moving parts. In the first case, mechanical parts, onto which filters or mirrors, etc. are mounted, are spatially translated for selecting the imaging wavelength. We can therefore name this category as **electromechanical tunable filters (EMTF)**. The second category refers to systems based on non-moving optical modules whose spectral transmission can be electronically controlled through the application of voltage or acoustic signal, etc. For this reason, the members of this class of instruments are known as **electronically tunable filters (ETF)**.

A simple and rather trivial EMTF is a set of discrete band-pass filters, which are swapping in front of the sensor. The filters can be mounted on a rotating disk or on a translating stage. **Linearly variable filters (LVF)**, with transmission centre wavelength varying linearly along their surface, comprise alternative to discrete filters option, but they are more suitable as monochromators of the illuminating source. In all these cases, the motion of the filter arrangements is driven by a stepper motor, and in most cases, it is synchronized with the successive image capturing.

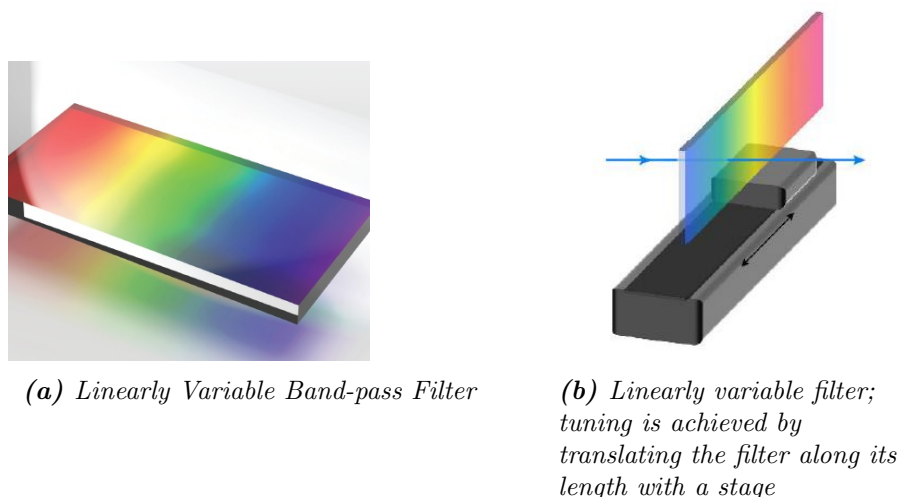


Figure 2.12: *Linearly Variable Filters*

A **Linearly Variable Filter (LVF)** is an optical interference filter whose spectral functionality varies along one direction of the filter, compared to a traditional optical filter whose spectral functionality is intended to be identical at any location of the filter. The term linear relates to the goal of making the wavelength variation a linear function of the position of the filter. The wavelength variation is achieved by an interference coating that is intentionally wedged in one direction, creating a linear shift of the center or edge wavelength along the same direction of the filter (see Fig. 2.13).

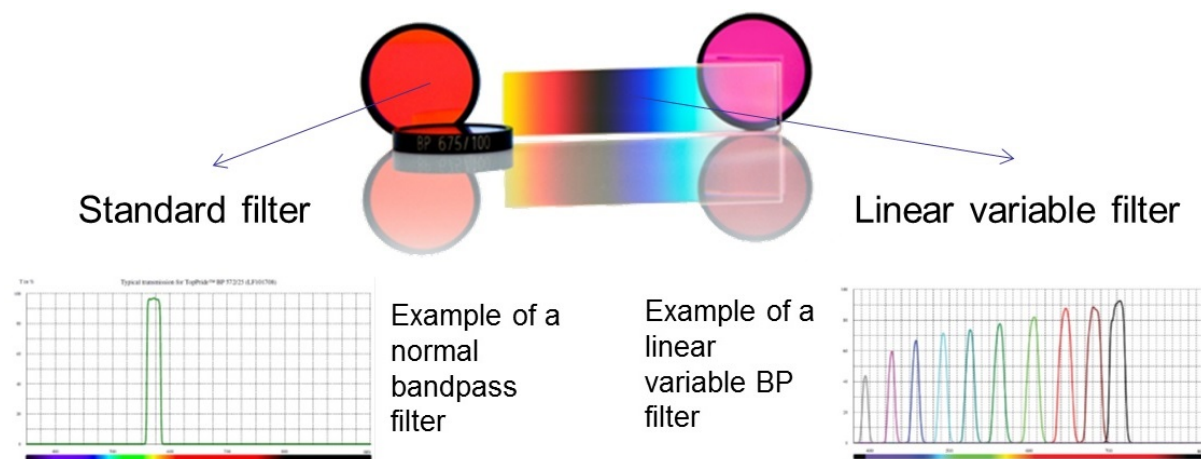


Figure 2.13: Design principle of standard and Linearly Variable Filters

2.8 Hyper-Spectral Imaging Applications

As it has already been mentioned, there are numerous applications emerging from the spectral analysis that is being provided by hyper-spectral imaging. For nearly a decade, this technology was primarily used for purposes like surveillance, reconnaissance, environmental and geological studies. However, the application of hyper-spectral imaging in the biomedical area has been negligible due to high-instrumentation costs and problems arising from the clinical use of hyper-spectral sensors. With recent achievements in sensor technology and increasing affordability of high performance spectral imagers, hyper-spectral imaging systems constitute one of the most important key areas in medical imaging. The early diagnosis of cancer, one of the most thorniest medical problems, is now possible, since the evolution of hyper-spectral sensors allows the scanning of a patient's body to identify precancerous lesions or to provide critical spectral data through endoscopic procedures. The extension and improvement of hyper-spectral imaging in biomedical and clinical diagnosis is within the grasp of researchers [7].

The advantages of this technology regarding diagnostic health care applications include a high-resolution imaging of tissues either at macroscopic or cellular levels and the capability to generate

highly accurate spectral information related to the patient, tissue sample, or any other disease condition. In particular, the vast investment of hyper-spectral imaging in medicine lies on the generation of wavelength-specific criteria for disease conditions on spectral features. As a consequence, an ideal technology for high-throughput patient screening and non-invasive diagnosis is begotten.

Due to their unparalleled ability to reveal abnormal spectral signatures, hyper-spectral medical instruments hold great potential for non-invasive diagnosis of cancer, retinal abnormalities and assessment of wound conditions, for instance diabetes. A portable hyper-spectral imager could also aid the analysis of human body fluids, such as blood, urine, saliva, semen and determine blood oxygenation levels of tissues, which could be of prime importance during surgeries. Yet importantly, it could perform diagnosis for dental diseases. It is a great advantage for a patient the fact that not only does an early diagnosis of an ailment take place, but an appropriate treatment may also be applied at the same time [1].

Hyper-spectral signatures when combined with targeting algorithms would in essence offer unique diagnostic information. There is an increasing level of interest on the part of health care providers to investigate possible ways of reducing health care costs by providing timely treatments for many types of disease conditions. **Hyper-Spectral scanning imaging** is expected to contribute a lot in this pursuit [2].

2.9 Measures of Spectral Similarity

Considering the spectral nature of this research work, it is essential to be able to compare the estimated spectra with the reference spectra, in order to probe the efficiency of the system. The spatial information is perceived as a group of n -dimensional vectors in the processing procedure, where n responds to the total number of different spectra being measured. As a consequence, a wide variety of statistic measures can be applied in order to measure the degree of similarity between the achieved and expected results. The metrics, which has been used for the needs of this implementation, are the following.

2.9.1 Euclidean Distance

In mathematics, the **Euclidean Distance** or **Euclidean Norm** is the ordinary distance between two points that one would measure with a ruler. In Cartesian coordinates, if $p = (p_1, p_2, \dots, p_n)$ and $q = (q_1, q_2, \dots, q_n)$ are two points in Euclidean n -space, then the distance from p to q or from q to p is given by the formula:

$$\begin{aligned}
d(p, q) = d(q, p) &= \sqrt{(q_1 - p_1)^2 + (q_2 - p_2)^2 + \cdots + (q_n - p_n)^2} \\
&= \sqrt{\sum_{i=1}^n (q_i - p_i)^2} \\
&= \|q - p\|
\end{aligned} \tag{1.2}$$

2.9.2 Root Mean Squared Error (RMSE)

Mean Squared Error (MSE) is one of many ways to quantify the difference between values implied by an estimator and the true values of the quantity being estimated. MSE measures the average of the squares of errors. The error is the amount by which the value implied by the estimator differs from the quantity that is being estimated. Taking the square root of MSE yields the **Root Mean Squared Error (RMSE)** or **Root Mean Squared Deviation (RMSD)**, which has the same units as the quantity being estimated. If $p = (p_1, p_2, \dots, p_n)$ and $q = (q_1, q_2, \dots, q_n)$ are two vectors, then the RMSE between them is given by the formula:

$$RMSE(p, q) = \sqrt{\frac{\sum_{i=1}^n (q_i - p_i)^2}{n}} \tag{1.3}$$

2.9.3 Goodness-of-Fit Coefficient (GFC)

Another metric for the evaluation of the results of spectral reconstruction algorithms is the **Goodness-of-Fit Coefficient (GFC)**. GFC is a metric developed in [36] to test reconstructed daylight spectra. The GFC is based on the inequality of Schwartz and it is calculated by:

$$GFC = \frac{|\sum_{i=1}^N q_i p_i|}{\sqrt{|\sum_{i=1}^N (q_i)^2|} \sqrt{|\sum_{i=1}^N (p_i)^2|}} \tag{1.4}$$

This metric is interesting because its value is bounded to the interval [0,1] and it provides an easy interpretation. From [36], if $GFC \geq 0.999$ the spectral match is considered as good and if $GFC \geq 0.9999$ the match is considered as excellent.

Chapter 3

Image Interpolation

3.1 Introduction

Image interpolation is involved in almost all applications where digital images are involved. Applications include image transformation (rotation, scaling); image magnification; lossy image compression and reconstruction; medical image generation and so on.

Interpolation is the process of determining the values of a function at positions lying between its samples. This process is achieved by fitting a continuous function through the discrete input samples. This permits input values to be evaluated at arbitrary positions in the input, not just those defined at the sample points. While sampling generates an infinite bandwidth signal from one that is band-limited, interpolation plays an opposite role: it reduces the bandwidth of a signal by applying a low-pass filter to the discrete signal. That is, interpolation reconstructs the signal lost in the sampling process by smoothing the data samples with an interpolation function.

For equally spaced data, interpolation can be expressed as:

$$f(x) = \sum_{k=0}^{K-1} c_k h(x - x_k) \quad (2.1)$$

where h is the interpolation kernel weighted by coefficients c_k and applied to K data samples, x_k . Eq. 2.1 formulates interpolation as a convolution operation. In practice, h is nearly always a symmetric kernel, i.e. $h(-x) = h(x)$.

The computation of one interpolated point is illustrated in Fig. 3.1. The interpolating function is centered at x , the location of the point to be interpolated. The value of that point is equal to the sum of the values of the discrete input scaled by the corresponding values of the discrete

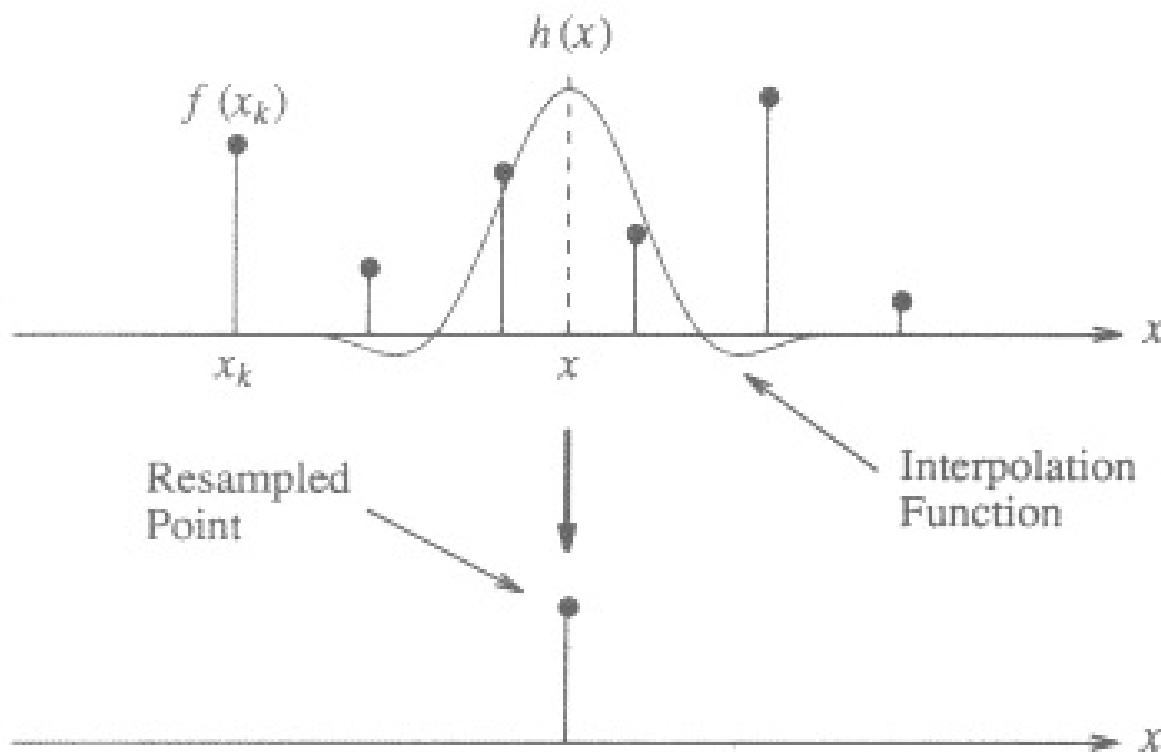


Figure 3.1: Interpolation of a single point

input scaled by the corresponding values of the interpolation kernel. This follows directly from the definition of convolution.

The interpolation function shown in Fig. 3.1 extends over four points. If x is offset from the nearest point by distance d , where $0 \leq d < 1$, we sample the kernel at $h(-d)$, $h(-1-d)$, $h(1-d)$, and $h(2-d)$. Since h is symmetric, it is defined only over the positive interval. Therefore, $h(d)$ and $h(1+d)$ are used in place of $h(-d)$ and $h(-1-d)$, respectively. Note that if the resampling grid is uniformly spaced, only a fixed number of points on the interpolation kernel must be evaluated. Large performance gains can be achieved by precomputing these weights and storing them in lookup tables for fast access during convolution.

3.2 Background and Concept

Interpolation arises from the concept of resampling which is the process of transforming a discrete image that is defined at one set of coordinate locations to a new set of coordinate points. Conceptually, resampling is divided into two processes: interpolation of the discrete image to a continuous image and then sampling the interpolated image. Fig. 3.2 illustrates the two processes of resampling. In the interpolation process, a discrete function, $x[n]$, is convolved with an interpolating function, $h(t)$, to produce a continuous function, $y(t)$. In the sampling

process, the continuous function is multiplied by a sampling function to produce a discrete function resampled at a new set of points, $v(\hat{n})$.

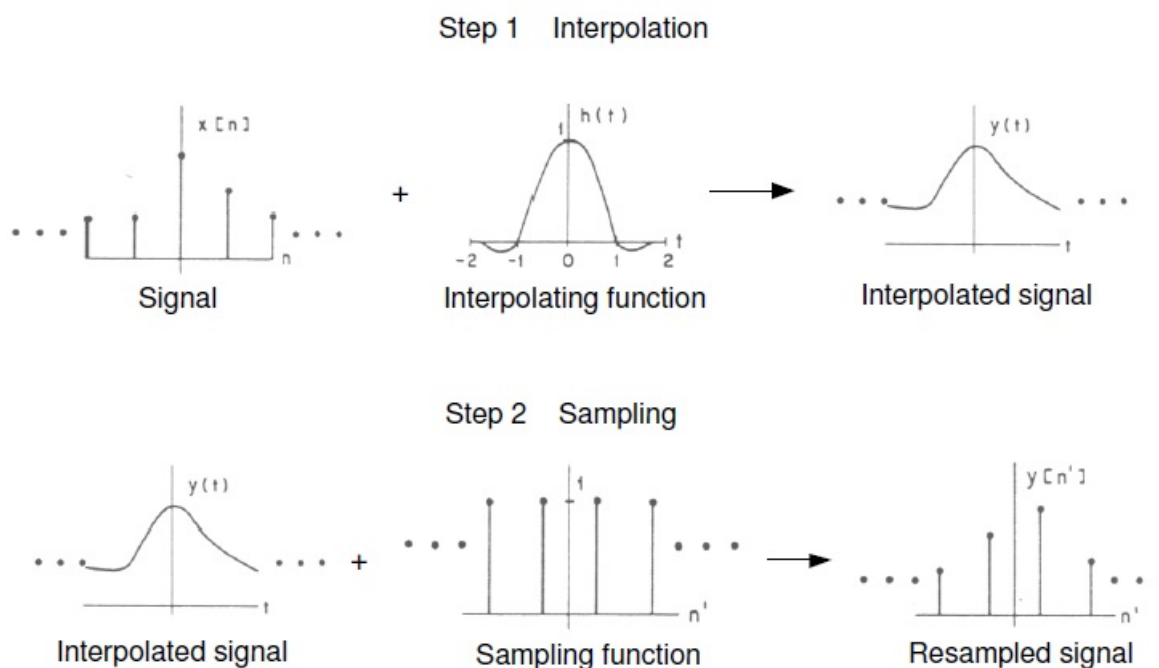


Figure 3.2: Two processes of resampling

The typical definition of interpolation is: model-based recovery of continuous data from discrete data with a known range of abscissa. In terms of digital image, the process of interpolation is to find the information for undefined pixels or missed pixels in an image based on the information provided by given pixels, so that the interpolated image is as close to the actual one as possible. The given information can be anything such as x or y coordination, color, gray level or density. Image can be any dimensions.

Several interpolation techniques have been developed and can be found in the literature. The most commonly used methods are the nearest neighbor, linear and spline interpolation techniques. Less common are the polynomial and Lagrange interpolation methods.

3.3 Different Interpolation Methods

The numerical accuracy and computational cost of interpolation algorithms are directly tied to the interpolation kernel. As a result, interpolation kernels are the target of design and analysis in the creation and evaluation of interpolation algorithms. In this section, the analysis is applied to the 1D case. Interpolation in 2D is a simple extension of the 1D case.

3.3.1 Nearest Neighbor

The simplest interpolation method from a computational standpoint is the **nearest neighbor** method which has a rectangular shape in space domain as shown in Fig. 3.3. This technique, also known as the **point shift** algorithm, is given by the following interpolating polynomial:

$$f(x) = f(x_k), \quad \frac{x_{k-1} + x_k}{2} \leq x \leq \frac{x_k + x_{k+1}}{2} \quad (2.2)$$

It can be achieved by convolving the image with a one-pixel width rectangle in the spatial domain. The interpolation kernel for the nearest neighbor algorithm is defined as:

$$h_0(x) = \begin{cases} 1 & |x| < 0.5 \\ 0 & \text{elsewhere} \end{cases} \quad (2.3)$$

The frequency response of the nearest neighbor kernel is:

$$H(\omega) = \text{sinc}\left(\frac{\omega}{2}\right) \quad (2.4)$$

The kernel and its Fourier transform are shown in Fig. 3.3.

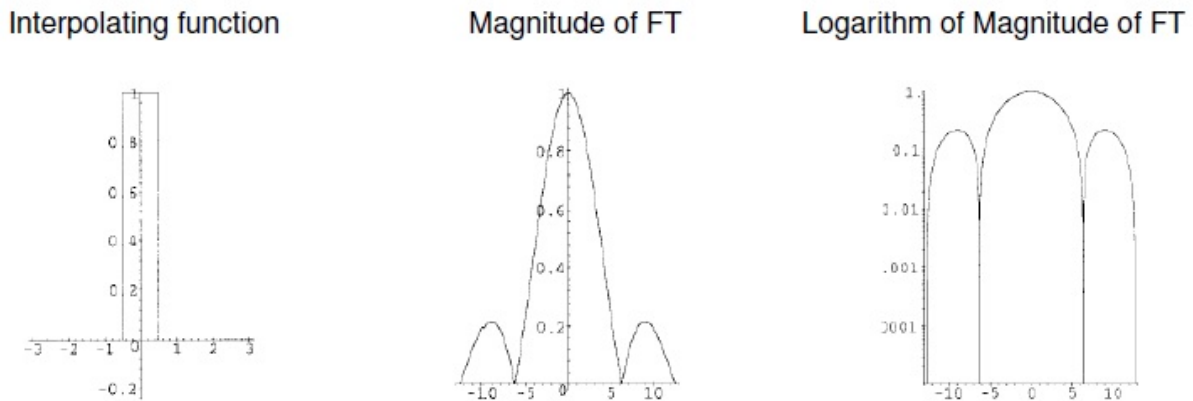


Figure 3.3: Nearest neighbor interpolation

The nearest neighbor method is the most efficient from the computation point of view but at the cost of poor quality as we can see from its frequency domain. The Fourier transformation of a square pulse is equivalent to a sinc function whose gain in the pass-band quickly falls off. Besides, it has prominent side lobes as illustrated in the logarithmical scale. These will result in strong blurring and aliasing effects in the interpolated image. Another effect caused by this

method is that the resampled image will be shifted with regard to the original image by the difference between the positions of the coordinate locations.

When applying nearest neighbor algorithm into image interpolation, the value of the new pixel is made the same as that of the closest existing pixel. The technique achieves magnification by pixel replication and minification by sparse point sampling. For large-scale changes, nearest neighbor interpolation produces images with a blocky appearance. In addition, shift errors of up to one-half pixel are possible. These problems make this technique inappropriate when sub-pixel accuracy is required.

3.3.2 Linear Interpolation

The next simple method is **linear interpolation** which has a triangle shape in space domain as shown in Fig. 3.4. Linear interpolation is a first-degree method that passes a straight line through every two consecutive points of the input signal. Given an interval (x_0, x_1) and function values f_0 and f_1 for the endpoints, the interpolating polynomial is:

$$f(x) = a_1x + a_0 \quad (2.5)$$

where a_0 and a_1 are determined by solving:

$$\begin{bmatrix} f_0 & f_1 \end{bmatrix} = \begin{bmatrix} a_1 & a_0 \end{bmatrix} \cdot \begin{bmatrix} x_0 & x_1 \\ 1 & 1 \end{bmatrix}$$

This gives rise to the following interpolating polynomial:

$$f(x) = f_0 + \left(\frac{x - x_0}{x_1 - x_0} \right) \cdot (f_1 - f_0) \quad (2.6)$$

Not surprisingly, we have just derived the equation of a line joining points (x_0, f_0) and (x_1, f_1) . In order to evaluate this method of interpolation, we must examine the frequency response of its interpolation kernel.

In the spatial domain, linear interpolation is equivalent to convolving the sampled input with the following interpolation kernel.

$$h_1(x) = \begin{cases} 1 - |x| & |x| < 1 \\ 0 & \text{elsewhere} \end{cases} \quad (2.7)$$

The frequency response of the linear interpolation kernel is:

$$H(\omega) = \text{sinc}^2\left(\frac{\omega}{2}\right) \quad (2.8)$$

The kernel and its Fourier transform are shown in Fig. 3.4.

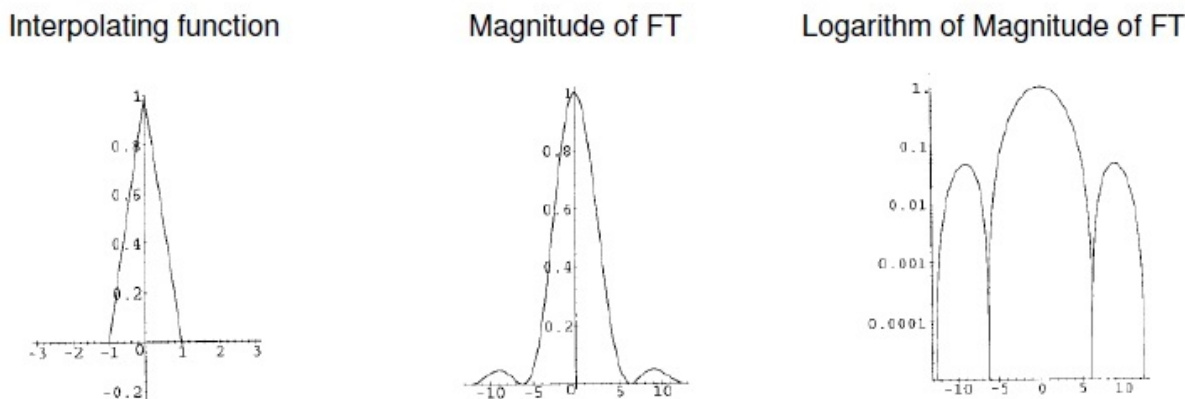


Figure 3.4: Linear interpolation

Comparing to the nearest neighbor function, this function is closer to the ideal square shape function so that more energy can be passed through. In particular, the side lobes in the stop-band are also much smaller, though still considerable. Therefore, the performance of linear interpolation is better than nearest neighbor interpolation. Nevertheless, according to its performance in frequency domain, we can see the drawbacks of this method are still the attenuation of high-frequency components and the aliasing of the data around the cut-off frequencies.

In image interpolation, the value of a new pixel is interpolated using the values from its four surrounding pixels in 2D. The new pixel value is a distance-based normalized linear combination of the four closest pixel values. Compared to the nearest neighbor approach, the apparent stair-step effect is significantly reduced and the image looks smoother.

It is the most widely used interpolation algorithm for reconstruction since it produces reasonably good results at moderate cost. Often, though, higher fidelity is required and thus more sophisticated algorithms have been formulated.

3.3.3 Cubic Convolution

Cubic convolution is a third-degree interpolation algorithm originally suggested by Rifman and McKinnon [12] as an efficient approximation to the theoretically optimum sinc interpolation function. Its interpolation kernel is derived from constraints imposed on the general cubic spline

interpolation formula. The kernel is composed of piecewise cubic polynomials defined on the unit subintervals $(-2,-1)$, $(-1,0)$, $(0,1)$, and $(1,2)$. Outside the interpolation interval $(-2,2)$, the interpolation kernel is zero. As a result, each interpolated point is a weighted sum of four consecutive input points. This has the desirable symmetry property of retaining two input points on each side of the interpolating region. It gives rise to a symmetric, space-invariant, interpolation kernel of the form:

$$h(x) = \begin{cases} a_{30}|x|^3 + a_{20}|x|^2 + a_{10}|x| + a_{00} & 0 \leq |x| < 1 \\ a_{31}|x|^3 + a_{21}|x|^2 + a_{11}|x| + a_{01} & 1 \leq |x| < 2 \\ 0 & \text{elsewhere} \end{cases} \quad (2.9)$$

We assume that our data points are located on the integer grid. The values of the coefficients can be determined by applying the following set of constraints to the interpolation kernel.

- $h(0)=1$ and $h(x)=0$ for $|x|=1$ and 2 .
- h must be continuous at $|x|=0, 1$, and 2 .
- h must have a continuous first derivative at $|x|=0, 1$, and 2 .

The first constraint states that when h is centered on an input sample, the interpolation function is independent of neighboring samples. This permits f to actually pass through the input points. In addition, it establishes that the c_k coefficients in Eq. 2.1 are the data samples themselves. This follows from the observation that at data point x_j ,

$$\begin{aligned} f(x_j) &= \sum_{k=0}^{K-1} c_k h(x_j - x_k) \\ &= \sum_{k=j-2}^{j+2} c_k h(x_j - x_k) \end{aligned} \quad (2.10)$$

According to the first constraint listed above, $h(x_j - x_k) = 0$ unless $j = k$. Therefore, the right-hand side of Eq. 2.10 reduces to c_j . Since this equals $f(x_j)$, we see that all c_k coefficients must equal the data samples in the four-point interval.

The first two constraints provide four equations for these coefficients:

$$\begin{aligned}
 1 &= h(0) = a_{00} \\
 0 &= h(1^-) = a_{30} + a_{30} + a_{30} + a_{30} \\
 0 &= h(1^+) = a_{31} + a_{21} + a_{11} + a_{01} \\
 0 &= h(2^-) = 8a_{31} + 4a_{21} + 2a_{11} + a_{01}
 \end{aligned} \tag{2.11}$$

Three more equations are obtained from constraint (3):

$$\begin{aligned}
 -a_{10} &= h'(0^-) = h'(0^+) = a_{10} \\
 3a_{30} + 2a_{20} + a_{10} &= h'(1^-) = h'(1^+) = 3a_{31} + 2a_{21} + a_{11} \\
 12a_{31} + 4a_{21} + a_{11} &= h'(2^-) = h'(2^+) = 0
 \end{aligned} \tag{2.12}$$

The constraints given above have resulted in seven equations. However, there are eight unknown coefficients. This requires another constraint in order to obtain a unique solution. By allowing $a = a_{31}$ to be a free parameter that may be controlled by the user, the family of solutions given below may be obtained.

$$h(x) = \begin{cases} (a + 2) \cdot |x|^3 - (a + 3) \cdot |x|^2 + 1 & 0 \leq |x| < 1 \\ a \cdot |x|^3 + 5a \cdot |x|^2 + 8a \cdot |x| - 4a & 1 \leq |x| < 2 \\ 0 & \text{elsewhere} \end{cases} \tag{2.13}$$

Additional knowledge about the shape of the desired result may be imposed upon Eq. 2.13 to yield bounds on the value of a . The heuristics applied to derive the kernel are motivated from properties of the ideal reconstruction filter, the sinc function. By requiring h to be concave upward at $|x| = 1$ and concave downward at $x = 0$, we have:

$$\begin{aligned}
 h''(0) &= -2(a + 3) < 0 \rightarrow a > -3 \\
 h''(1) &= -4a > 0 \rightarrow a < 0
 \end{aligned} \tag{2.14}$$

Bounding a to values between -3 and 0 makes h resemble the sinc function. In [12], the authors use the constraint that $a = -1$ in order to match the slope of the sinc function at $x = 1$. This choice results in some amplification of the frequencies at the high-end of the pass-band. As stated earlier, such behavior is characteristic of image sharpening.

Other choices for a include -0.5 and -0.75 . *Keys* selected $a = -0.5$ by making the Taylor series approximation of the interpolated function agree in as many terms as possible with the original

signal [10]. He found that the resulting interpolating polynomial will exactly reconstruct a second-degree polynomial. Finally, $a = -.75$ is used to set the second derivatives of the two cubic polynomials in h to 1 [13]. This allows the second derivative to be continuous at $x = 1$.

Of the three choices for a , the value -1 is preferable if visually enhanced results are desired. That is, the image is sharpened, making visual detail perceived more readily. However, the results are not mathematically precise, where precision is measured by the order of the Taylor series. To maximize this order, the value $a = -.5$ is preferable. The kernel and spectrum of a cubic convolution kernel with $a = -.5$ is shown in Fig. 3.5.

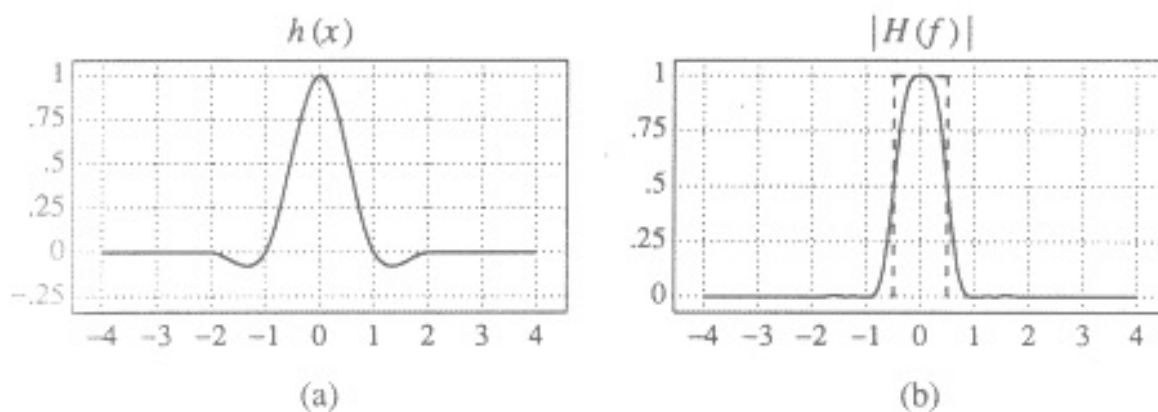


Figure 3.5: Cubic convolution: (a) kernel, (b) Fourier transform

It is important to note that in the general case, cubic convolution can give rise to values outside the range of the input data. Consequently, when using this method in image processing, it is necessary to properly clip or rescale the results into the appropriate range for display.

3.3.4 B-Splines

From the above analyses in frequency domain, we know that both nearest neighbor and linear interpolation have a large deviation from the ideal rectangular shape in the pass-band and considerable side lobes in the stop-band. The image interpolated by nearest neighbor method will exhibit jaggedness while linear interpolator will cause the image to be blurred. **B-spline** interpolations have been regarded as a solution due to many attractive properties, such as compact support, sufficient regularity, smooth behavior and easy implementation. *Meijering* compared different interpolation methods and concluded that the spline interpolation constitutes the best trade-off between accuracy and computational cost [14].

The concept of splines and their mathematical representations were first described by *Schoenberg* in 1946 [15]. Researchers then studied and developed many algorithms of splines for different applications afterwards. Among these algorithms, cubic B-splines show the most optimum

characteristics. The use of cubic splines in image interpolation and digital filtering was pioneered by *Hou* and *Andrews* [11]. In the following, we give the fundamental definition of B-spline functions, introduce the three cubic B-spline model, compare their mathematical foundations and interpolation performance.

3.3.4.1 Definition of B-Splines

Splines are piecewise polynomials with pieces that are smoothly connected together. Basis splines (B-splines) are one of the most commonly used family of spline functions. They can be derived by several self-convolutions of a so called basis function as follows:

$$\beta^0(x) = \begin{cases} 1 & |x| < \frac{1}{2} \\ \frac{1}{2} & |x| = \frac{1}{2} \\ 0 & |x| > \frac{1}{2} \end{cases} \quad (2.15)$$

If we define B-spline of degree n as $\beta^n(x)$, it can be expressed as:

$$\begin{aligned} \beta^n(x) &= \underbrace{\beta^0 * \beta^0 * \dots * \beta^0(x)}_{n+1 \text{ times}} \\ &= \sum_{k=0}^{n+1} \frac{(-1)^k (n+1)}{(n+1-k)!k!} \left(\frac{n+1}{2} + x - k\right)_+^n, \quad \forall x \in \mathfrak{R}, \forall n \in \mathfrak{N}_* \end{aligned} \quad (2.16)$$

where by definition

$$(x)_+^n = (\max(0, x))^n, \quad n > 0 \quad (2.17)$$

B-spline functions are piecewise polynomials of degree n ; they are globally symmetric and $(n-1)$ times continuously differentiable. In Eq. 2.16, setting $n = 0$ will yield zero degree B-spline function represented explicitly in Eq. 2.15. Comparing Eq. 2.15 with Eq. 2.3, we can see that the zero degree B-spline is almost identical to the nearest neighbor function except the definition at the boundaries. When n is set to 1, the B-spline function of degree one is exactly identical to the linear condition. Likewise, $n = 2$ defines a quadratic B-spline and $n = 3$ defines a cubic B-spline. The B-spline functions with degree from 0 to 3 are illustrated in Fig. 3.6.

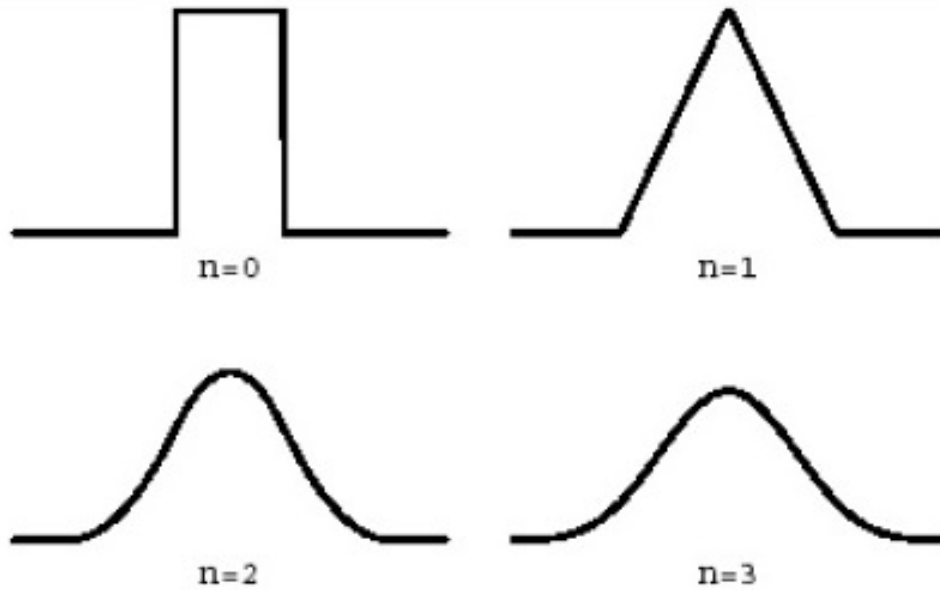


Figure 3.6: The centered B-splines of degree 0 to 3

3.3.4.2 Cubic B-Splines

Since the cubic B-spline provides the best trade-off between performance and computation efficiency in spline families, it is the mostly often used in practice. By setting $n = 3$ in Eq. 2.16, we get the common cubic B-spline expression:

$$\beta^3(x) = \begin{cases} \frac{2}{3} - \frac{1}{2}|x|^2(2 - |x|) & 0 \leq |x| < 1 \\ \frac{1}{6}(2 - |x|)^3 & 1 \leq |x| < 2 \\ 0 & 2 \leq |x| \end{cases} \quad (2.18)$$

The response of this interpolating function is shown in Fig. 3.7.

There are several properties of cubic B-splines worth noting. As in the cubic convolution method, the extent of the cubic B-spline is over four points. This allows two points on each side of the central interpolated region to be used in the convolution. Consequently, the cubic B-spline is shift-invariant as well. It is, also, an approximating function that passes near the points but not necessarily through them. This is due to the fact that the kernel is strictly positive.

Apparently it has better response in both pass-band and stop-band comparing with the nearest neighbor and linear functions. The positivity of the cubic B-spline kernel is actually attractive for our image processing application. When using kernels with negative lobes it is possible to generate negative values while interpolating positive data. Since negative intensity values are

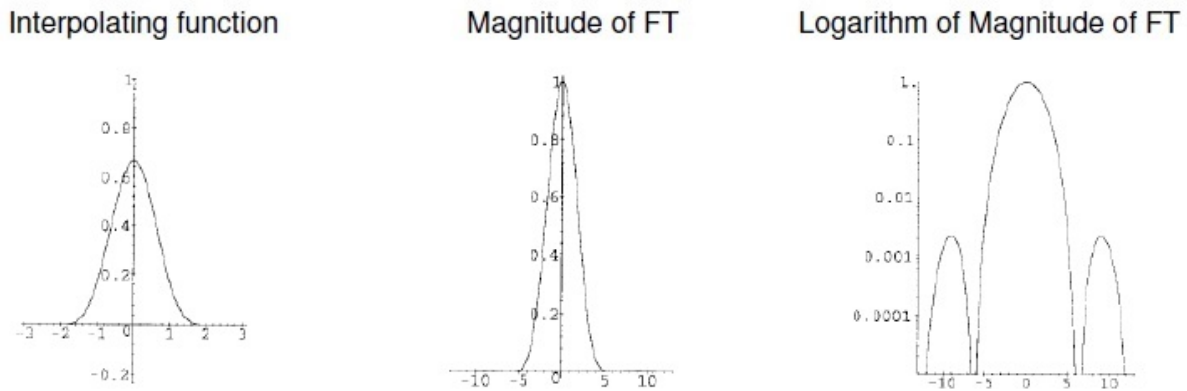


Figure 3.7: Cubic B-spline interpolation

meaningless for display, it is desirable to use strictly positive interpolation kernels to guarantee the positivity of the interpolated image.

However, the function is positive over the whole interval from -2 to 2 in the space domain, which translates to have more deviation from the constant gain within the pass-band in frequency domain. This will smooth more than is necessary below the cut-off frequency. Therefore, the cubic B-spline function needs to be modified to have negative values in the space domain. To derive such function, we first present the general cubic B-spline function as follows:

$$\beta^3(x) = \begin{cases} a_{30}x^3 + a_{20}x^2 + a_{10}x + a_{00} & 0 \leq x < 1 \\ a_{31}x^3 + a_{21}x^2 + a_{11}x + a_{01} & 1 \leq x < 2 \end{cases} \quad (2.19)$$

Since the function is symmetrical about zero, only interval between 0 and 2 are studied. Seven constraints can be used to solve the function:

$$\beta(0) = 1; \quad (2.20)$$

$$\beta(1) = 0; \quad (2.21)$$

$$\beta(2) = 0; \quad (2.22)$$

$$\beta'(0) = 0; \quad (2.23)$$

$$\beta'(2) = 0; \quad (2.24)$$

$$\beta(1)_- = \beta(1)_+; \quad (2.25)$$

$$\beta(1)'_- = \beta(1)'_+; \quad (2.26)$$

Solving 8 unknowns in Eq. 2.19 with 7 constraints leaves one constant in the equation. The function looks like following:

$$\beta^3(x) = \begin{cases} (a+2) \cdot x^3 - (a+3) \cdot x^2 + 1 & 0 \leq x < 1 \\ a \cdot x^3 + 5a \cdot x^2 + 8a \cdot x - 4a & 1 \leq x < 2 \end{cases} \quad (2.27)$$

The constant a has to be negative because we want the function positive in the interval $(0, 1)$ and negative in the interval $(1, 2)$. These modified functions are referred as the high-resolution cubic B-spline interpolating functions because they provide better high-frequency performance than the common cubic B-spline described above.

Two different constants, $a = -1.3$ and $a = -0.5$, are used to examine the modified functions. The performance of these two high-resolution cubic B-spline functions is better than that of the common cubic B-spline function as can be seen clearly in their frequency domain from Fig. 3.8 and Fig. 3.9.

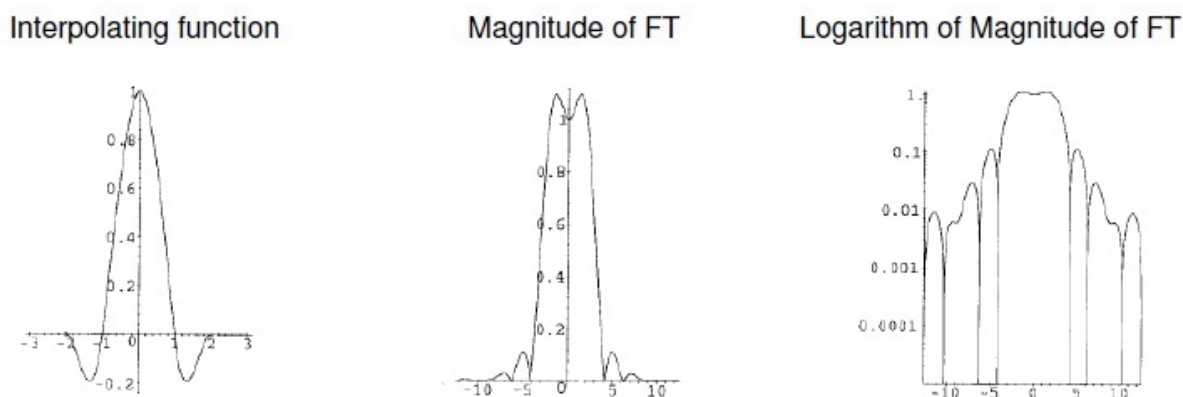


Figure 3.8: Cubic B-spline interpolation ($a=-1.3$)

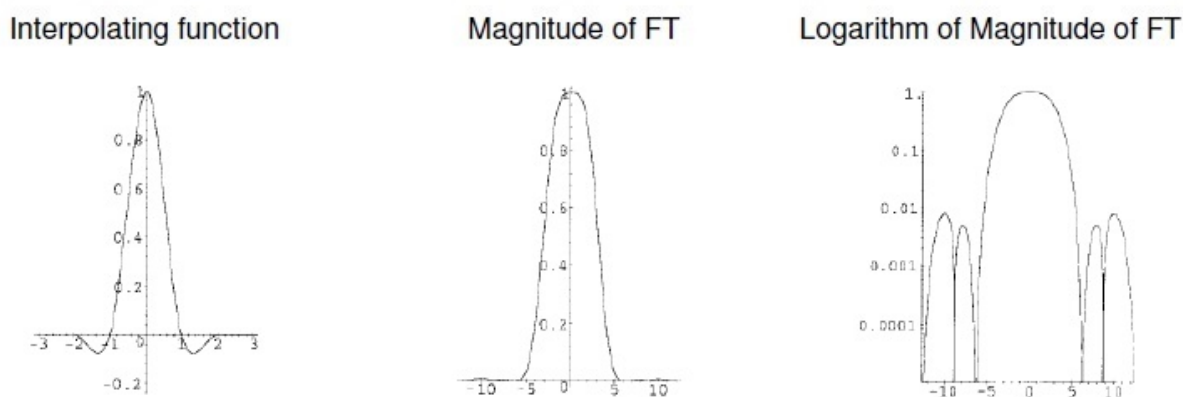


Figure 3.9: Cubic B-spline interpolation ($a=-0.5$)

When $a = -1.3$, the Fourier transform of the function deviates minimally from the ideal rectangular function in the pass-band and the transition between the pass-band and the stop-band is quite sharp. Though the amplitude of side lobes is still considerable. When $a = -0.5$, the overall response is the best. Thus, it is regarded to be the optimal function for image interpolation.

Chapter 4

Hyper-Spectral Imager

4.1 Detector Response Modeling

There are different approaches to acquire the spectral response of a digital camera. The most obvious one is to ask the sensor manufacturer for the data sheet. Unfortunately there are some shortcomings. First is that only some manufacturers publish the data sheets. Even if the data sheet is available, there are problems. Often the manufacturer does not give much information how the measurement was performed. In detail that means: What filters were used? Was a lens used? Additionally to these issues there might be variations in spectral response from device to device.

4.1.1 Methodology

In order to perform a spectral characterization of an electronic camera, it is necessary to establish a model of the system. In section 4.2.1 we describe a general spectral model of an image acquisition system. This model applies to several types of image acquisition systems, in particular to electronic CCD cameras.

4.1.2 Image Acquisition System Model

A camera response model is used to characterize how a digital camera responds to a spectral power distribution. The image sensors in digital cameras are inherently linear devices. So a linear camera response model is usually appropriate. The assumption of linearity has to be verified. If the device is not linear, the response model needs to be extended with a function that describes the non-linearity.

The main components involved in the image acquisition process are depicted in Fig. 4.1. We denote the spectral radiance of the illuminant by $l_R(\lambda)$, the spectral reflectance of the object surface imaged in a pixel by $r(\lambda)$, the spectral transmittance of the optical systems in front of the detector array by $o(\lambda)$, the spectral transmittance of the linearly variable band-pass filter by $\phi(\lambda)$ and the spectral sensitivity of the image sensor array by $a(\lambda)$.

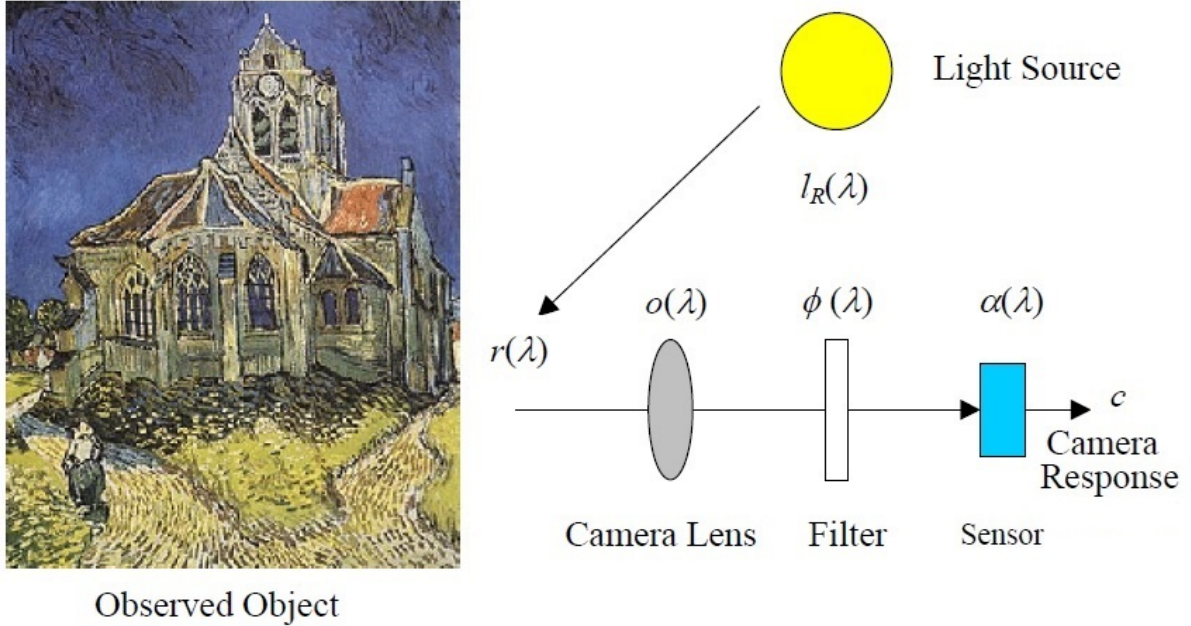


Figure 4.1: Schematic view of the image acquisition process. The camera response depends on the spectral sensitivity of the sensor, the spectral transmittance of the filter and optical path, the spectral reflectance of the objects in the scene, and the spectral radiance of the illumination.

Supposing a linear optoelectronic transfer function of the acquisition system, the camera response c to an image pixel is then equal to:

$$c = \int_{\lambda_{min}}^{\lambda_{max}} l_R(\lambda)r(\lambda)o(\lambda)\phi(\lambda)a(\lambda)d\lambda + \epsilon \quad (3.1)$$

where ϵ is the additive noise. The limits λ_{min} and λ_{max} enclose the sensitive spectral area of the image sensor. Often the limits of the human visual area are used (380 nm to 720 nm). The assumption of system linearity is founded on the fact that the image sensor is inherently a linear device. However, for real acquisition systems this assumption may not hold, due for example to stray light in the camera. Then, appropriate non-linear corrections may be necessary.

Eq. 3.1 is extended to:

$$\check{c} = \Gamma \left(\int_{\lambda_{min}}^{\lambda_{max}} l_R(\lambda) r(\lambda) o(\lambda) \phi(\lambda) a(\lambda) d\lambda + \epsilon \right) \quad (3.2)$$

Function Γ describes the non-linearity of the device. By modeling the non-linearities of the system, we may easily obtain the response:

$$c = \Gamma^{-1}(\check{c}) \quad (3.3)$$

By uniformly sampling the spectra at N equal wavelength intervals, we can rewrite Eq. 3.1 as follows:

$$c = r^T l_R(\lambda) o(\lambda) \phi(\lambda) a(\lambda) + \epsilon \quad (3.4)$$

4.1.3 Basics of Interference Filters

Interference filters are multilayer thin-film devices. They utilize the interferences of a single or multiple reflected beams of light to block certain wavelengths.

4.1.3.1 Interference

The incident light is passed through coated reflecting surfaces. The essential component of these filters is the simplest Fabry-Perot interferometer, two partially reflecting thin-film layers separated by a dielectric spacer. The distance between the reflective coatings determines which wavelength destructively interfere and which wavelengths are in phase and will ultimately pass through the coatings. If the reflected beams are in phase, the light is passed through two reflective surfaces. If the multiple reflections are not in phase, destructive interference reduces the transmission of these wavelengths through the device to near zero. This principle strongly attenuates the transmitted intensity of light at wavelengths that are higher or lower than the optimal wavelength for which the multiple reflections are in phase. Fig. 4.2 shows the interference at a thin layer. The transmittance of a double-layer setup according to Fig. 4.2 is:

$$\tau_\lambda = \frac{(1 - s_1^2) * (1 - s_2^2)}{1 + s_1^2 * s_2^2 + s_1 * s_2 * \cos(\phi)} \quad (3.5)$$

With:

$$s_1 = \frac{n_0 - n_1}{n_0 + n_1} \quad s_2 = \frac{n_1 - n_2}{n_1 + n_2} \quad \phi = 2\pi * n_1 * \frac{d}{\lambda}$$

The interference at the boundary layer causes a strong influence on the wavelength dependency of the transmittance. Interference filters with several layers utilize this effect. Usually these layers are made of translucent material. So the influence of the absorption can be neglected.

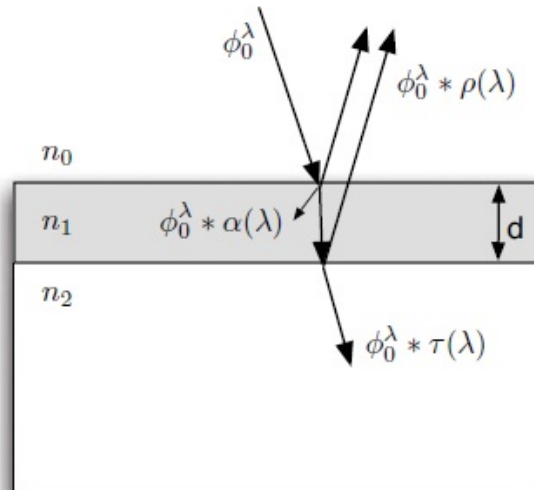


Figure 4.2: Interference at a thin layer

4.1.3.2 Interference Filter Parameters

Following terms are used to describe the characteristics of interference filters.

Passband: The range of wavelengths passed by the wavelength-selective filter.

Blocking: The degree of light attenuation at wavelengths outside the passband of the filter.

Center Wavelength (CWL): The wavelength at the middle of the half power bandwidth (FWHM).

Full-Width Half-Maximum (FWHM): The width of the passband at 50% of the maximum transmittance (τ_{max}).

Tenth-bandwidth (TBW): The width of the passband at 10% of τ_{max} .

Hundredth-bandwidth (HBW): The width of the passband at 1% of τ_{max} .

Filter Cavity: Most interference band-pass filters are designed with multiple cavities. The combination of several cavities determines the shape of the passband filter. Multiple cavities allow to get a nearly rectangular transmittance function.

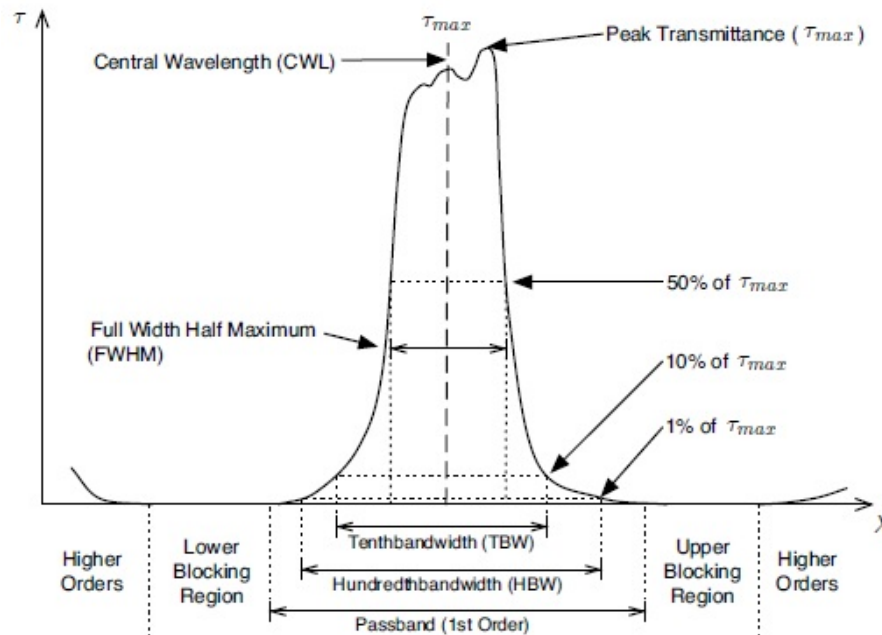


Figure 4.3: Interference filter parameters

4.2 Image Acquisition System

4.2.1 Set Up

The experimental set up is an imaging system that performs the hyper-spectral scanning procedure automatically. In this point, it should be mentioned that the calibration of camera takes place once, before the beginning of the hyper-spectral scanning. The single intervention along with the abolishment of the “slit-scan” technique are the two innovations we introduce in such a HSI. The used components and materials with all the necessary technical information, are included in the following tables and figures.

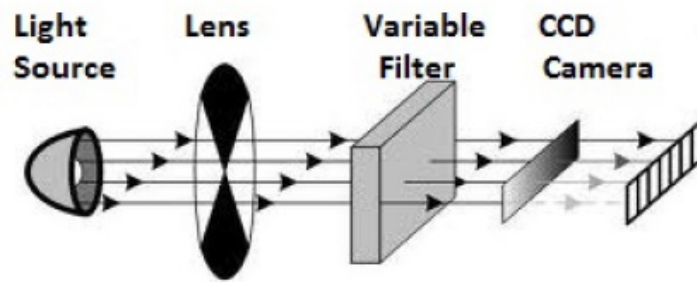


Figure 4.4: Optical elements

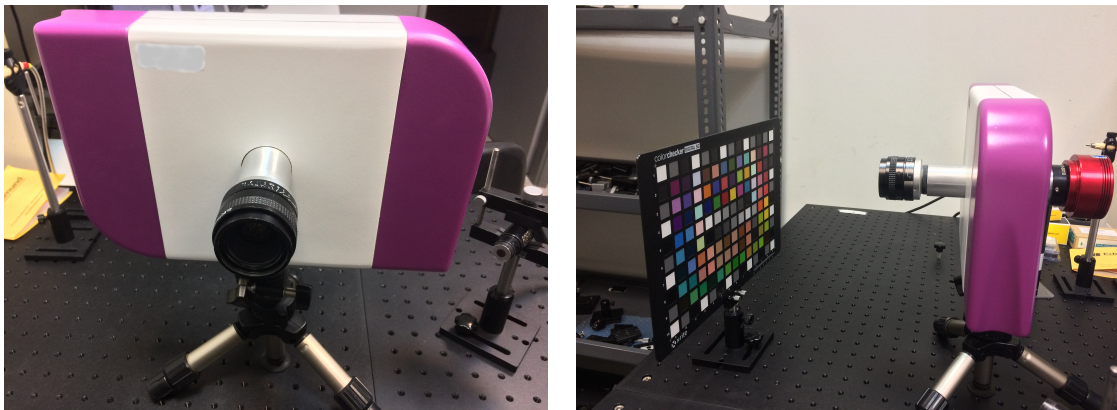


Figure 4.5: The HSI system

4.2.1.1 Technical Specifications and Features

Sofradir-EC (Electrophysics) L25F1.4 25mm f/1.4 C-Mount Objective Lens with Iris



Figure 4.6: Sofradir-EC

The Sofra L25F1.4 25mm F1.4 C-Mount Objective Lens features manual focus and an integrated adjustable iris diaphragm. These lenses also feature broadband lens coating making them ideal low cost solutions for imaging in the near-infrared spectral range with reduced flare and ghosting.

A C-Mount Extension Tube kit is also available for those applications requiring close focus and higher magnification.

FEATURES	Universal C-Mount for cameras and viewers, manual focus, integral adjustable iris diaphragm, broadband lens coating for near-infrared imaging.
TECH SPECS	Objective Lens \mapsto 25mm

Table 4.1: Sofradir-EC Specifications

Linearly Variable Band-Pass Filter (330 – 745 nm, #83 – 983, Edmund Optics)

Designed for both individual and combined use, long-wave and band-pass variable edge filters allow for blocking and passing of targeted wavelengths. Used independently, the short-wave linearly variable filter has a wavelength range of 330 – 750 nm with an average transmission of 97% from 400 – 750 nm. The long-wave linearly variable filter has a wavelength range of 300 – 845 nm and an average transmission of 97% across the entire range. Band-pass filters only transmit a certain wavelength band and block others. When combined, linearly variable filters can operate as a laser-line filter or a variable band-pass filter with tunable center wavelength and bandwidth.

A linearly variable filter (LVF) has an interference coating intentionally wedged in one direction to create a linear shift of the center wavelength across the length of the substrate. This shift allows for the broad filtering capabilities demonstrated by the short and long-wave variable filters. Short and long-wave variable filters work inversely of one another; the short-wave variable filter passes light throughout the filter's length until a blocking band is reached, whereas the long-wave variable filter blocks light until a transmission band is reached. Blocking and transmission bands are adjustable by reorienting the filter to the light source.

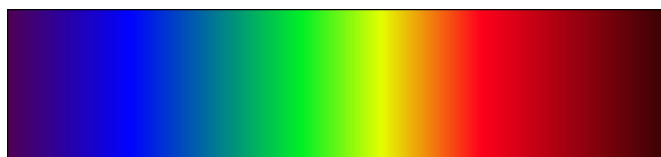


Figure 4.7: Linearly Variable Filter

With its broad blocking and transmission range, a single linearly variable filter can replace an entire filter set. When synchronized with a single moving grating spectrometer, combined long and short-wave linearly variable filters reduce scattered light and harmonics. In addition, combined linearly variable filters can be used as a single variable excitation filter for various fluorescence applications using white light sources.

Dimensions (mm)	15×60
Slope Factor (%)	1.6
Linear Dispersion (%)	0.57
Transmission (%)	
400 – 750 nm	97
Optical Density (OD)	> 4.0
Wavelength (nm)	330 – 750
RoHS	compliant

Table 4.2: Linearly Band-pass Filter Specifications

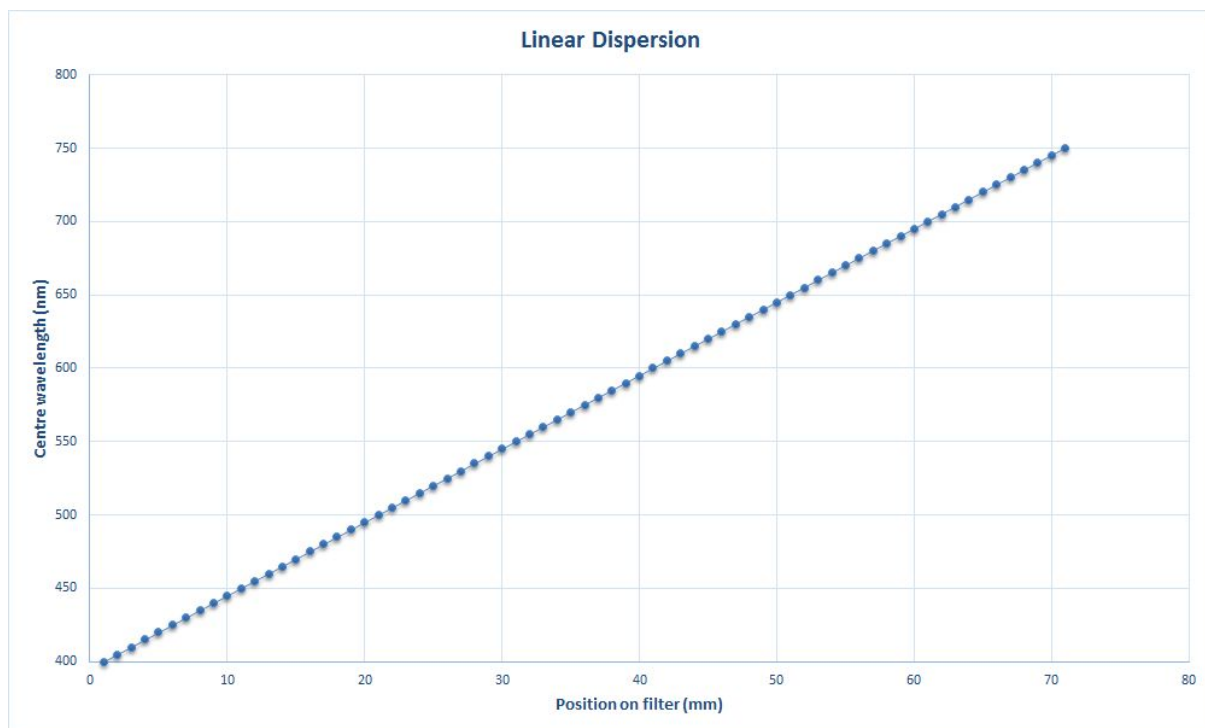


Figure 4.8: Linear Dispersion

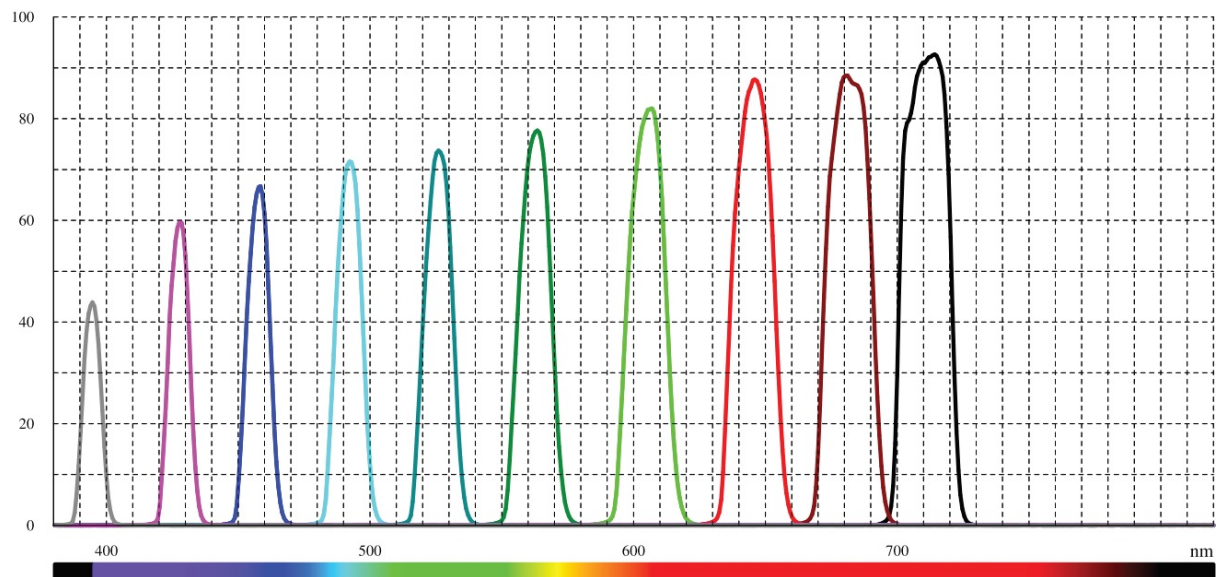


Figure 4.9: Transmission characteristics of linearly variable band-pass filter.

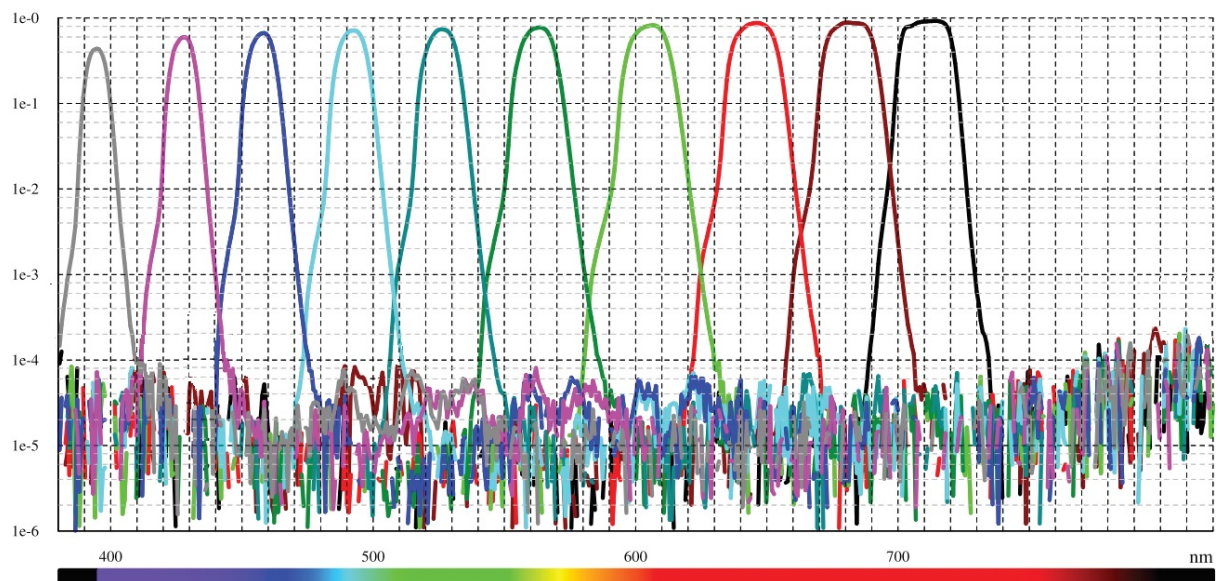


Figure 4.10: Blocking characteristics of linearly variable band-pass filter.

ZWO ASI178MM Monochrome Astronomy Camera

Figure 4.11: ZWO ASI178MM Monochrome Astronomy Camera

The ZWO ASI178MM is a sensitive and state-of-the-art monochrome astronomy camera with 6.4M resolution and USB 3.0 download speed. Built around the Sony IMX178 back-illuminated image sensor, this advanced camera has a resolution of 3096×2080 with $2.4 \mu\text{m}$ square pixel size. With 14-bit ADC and extremely low read noise ($2.2e - 1.4e$), this high-sensitivity camera is ideal for high-resolution astronomical imaging and works well for microscopy imaging as well.

The heart of this monochrome camera is a Type $1/1.8''$ CMOS sensor with 8.92 mm diagonal. This advanced sensor incorporates Sony's Exmor R technology that enables high-speed processing, low noise, and low power dissipation using column parallel A/D conversion with the back-illuminated sensor. The sensor also incorporates Sony's STARVIS technology features a sensitivity of 2000 mV+ per 1 micron square and allows high image quality in the visible-light and near-infrared light regions.

The 14-bit ADC enables high dynamic range and reduced quantization noise and dark random noise. This makes for cleaner image quality in light and dark areas when imaging objects with high contrast.

The rolling shutter and fast USB 3.0 interface on the camera allow transfer rates of up to 60 frames per second at full 3096×2080 resolution. At reduced resolution of 640×480 , download rates up to 253 fps become possible. The camera enables exposure times of $32 \mu\text{s}$ to 1000 s (16.7 minutes).

QE and Read Noise are the most important parameters to measure the performance of a camera. Higher QE and lower Read Noise are needed to improve the SNR of an image. Read Noise includes pixel diode noise, circuit noise and ADC quantization error noise, and the lower the better. The Read Noise of the ASI178 cameras is extremely lower when compared with

traditional CCD cameras. It is even lower when the camera is set at a higher gain. Depending on your target, you can set the Gain lower for higher Dynamic Range (longer exposure) or set the Gain higher for lower noise (such as short exposure or lucky imaging).

Sensor	1/1.8" CMOS IMX178
Resolution	6.4 Mega Pixels 3096×2080
Pixel Size	7.4mm×5mm
Diagonal	8.92mm
Exposure Range	32 μ s – 1000s
ROI	Supported
ST4 Guider Port	Yes
Focus Distance to Sensor	12.5mm
Shutter Type	Rolling Shutter
Protect Window	AR window
OS Compatibility	Mac, Windows, Linux
Interface	USB3.0/USB2.0
Bit Rate	14bit output (14-bit ADC)
Adaptor	2"/1.25"/M42X0.75
Dimension	ϕ 62mm×36mm
Weight	120g or 4.2 ounces (without lens)
Working Temperature	-5°C – 45°C
Storage Temperature	-20°C – 60°C
Working Relative Humidity	20% – 80%
Storage Relative Humidity	20% – 95%

Table 4.3: ZWO ASI178MM Camera Technical Specifications

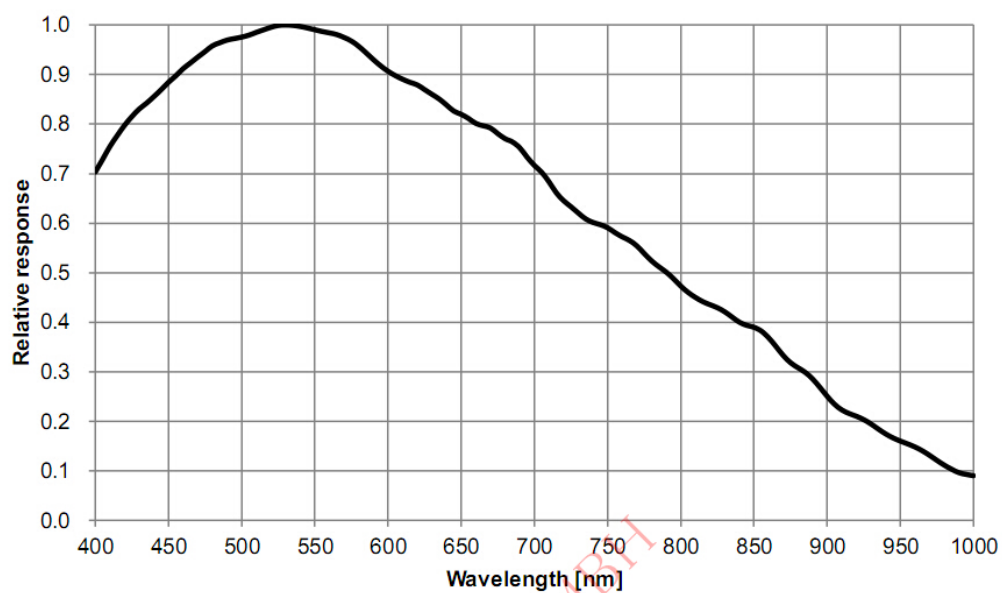


Figure 4.12: Mono 178 sensor Relative QE Curve

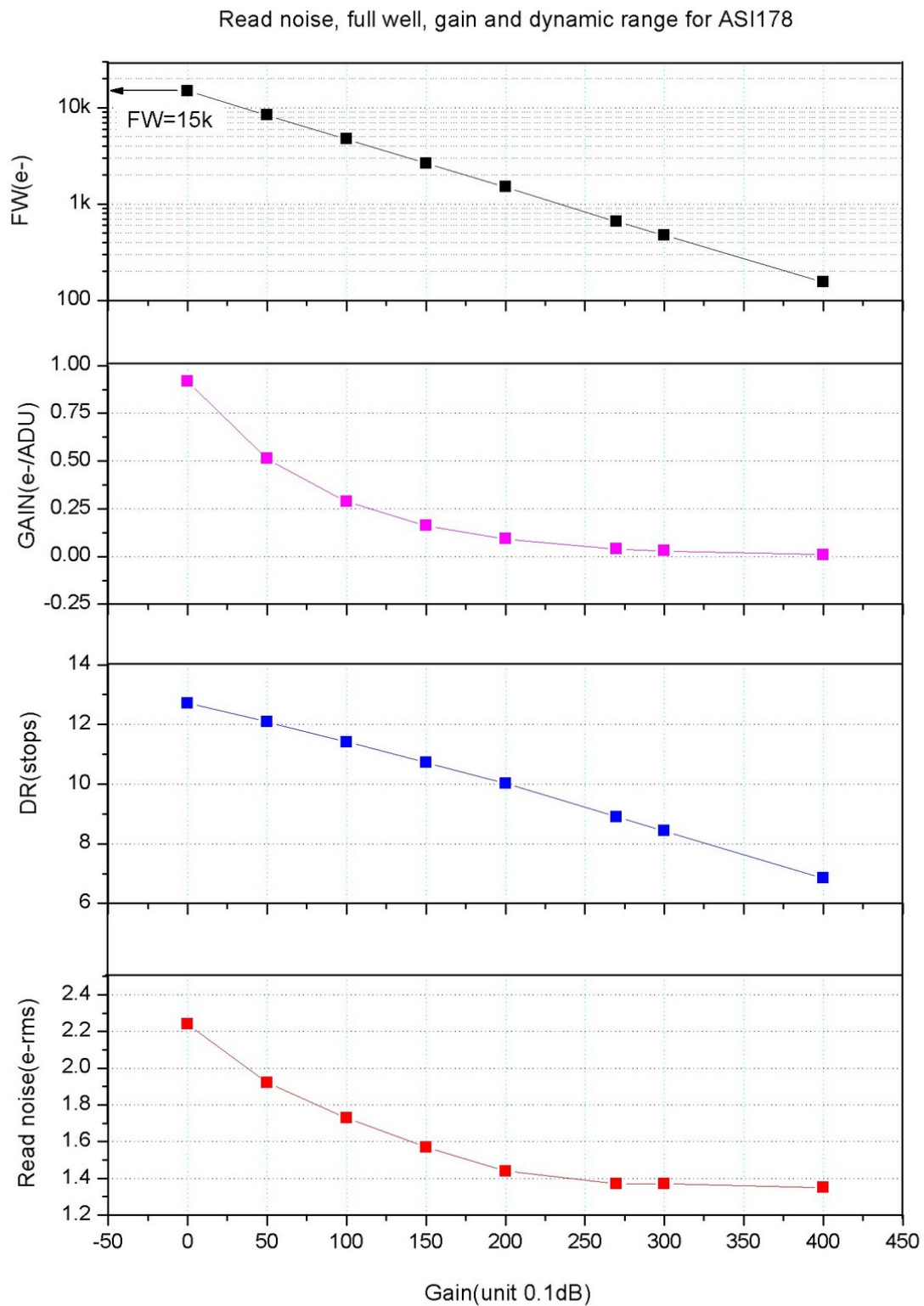


Figure 4.13: Read noise, full well, gain and dynamic range for ASI178

Halogen OSL1-EC Fiber Light Source

The experimental procedure of the hyper-spectral scanning has been held with the contribution of a light source. This unit is a high intensity fiber coupled light source that contains a 150 W halogen lamp with a 1000:1 exponentially variable control. It is designed to deliver strong, cool light for **microscopy** and **lab** applications.



Figure 4.14: *Halogen OSL1-EC Fiber Light Source*

Input Voltage	110 – 120 VAC or 220 – 240 VAC, 180 W Max
Light Output	40,000 Foot-Candles
Lamp Adjustment Range	1000:1 (0 to 100%)
Color Temperature	3200 K with Standard EKE Lamp at Max Intensity
Lamp Life	250 – 10,000 Hours
Operating Temperature	0 – 40°C
Humidity Range	0 – 80% Non Condensing
Weight (Light Source without Fiber Bundle)	7.5 lbs (3.4 kg)

Table 4.4: *Halogen OSL1-EC Fiber Light Source Specifications*

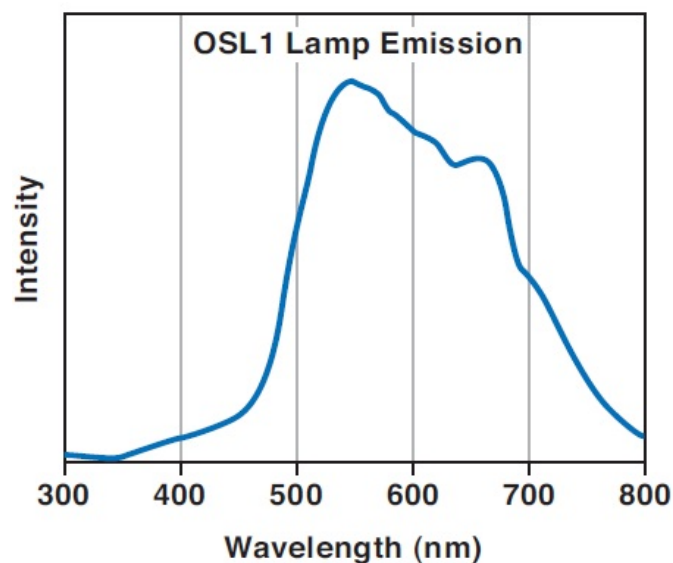


Figure 4.15: *Halogen OSL1-EC Emission Diagram*

Liquid Light Guide

Liquid light guides are clearly superior to light guides made of silica fiber bundles by the very nature of their design. A liquid light guide is much like a single silica fiber with a very large diameter. It has the cross-section of an open pipe, transmitting light with total reflectance using all the space available. Silica fiber bundles, in contrast, are like many small tubes in a larger pipe with spaces between the individual strands remaining unused. These dead spots do not transmit light. This is why liquid light guides are able to deliver light with much greater intensity to the target object.



Figure 4.16: *Liquid Light Guide*

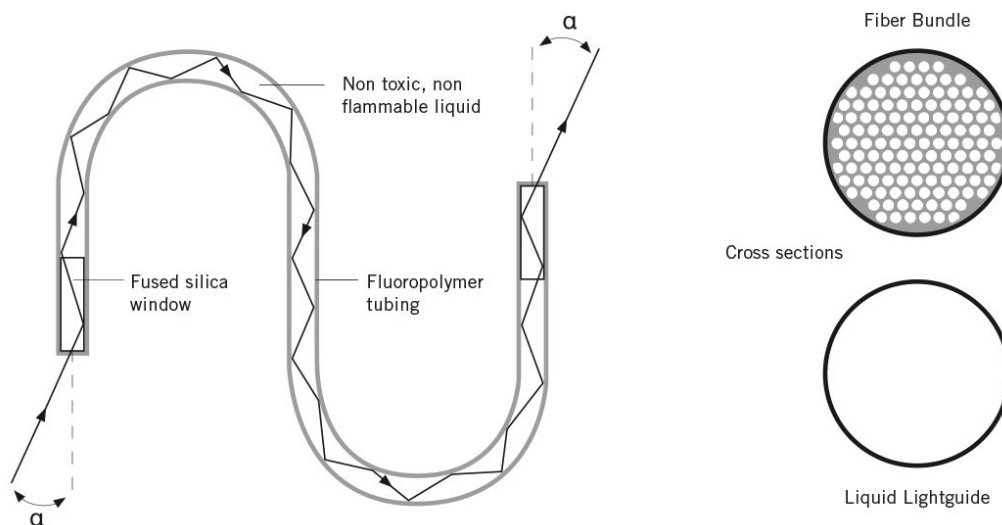


Figure 4.17: *Principle of the Liquid Light Guide*

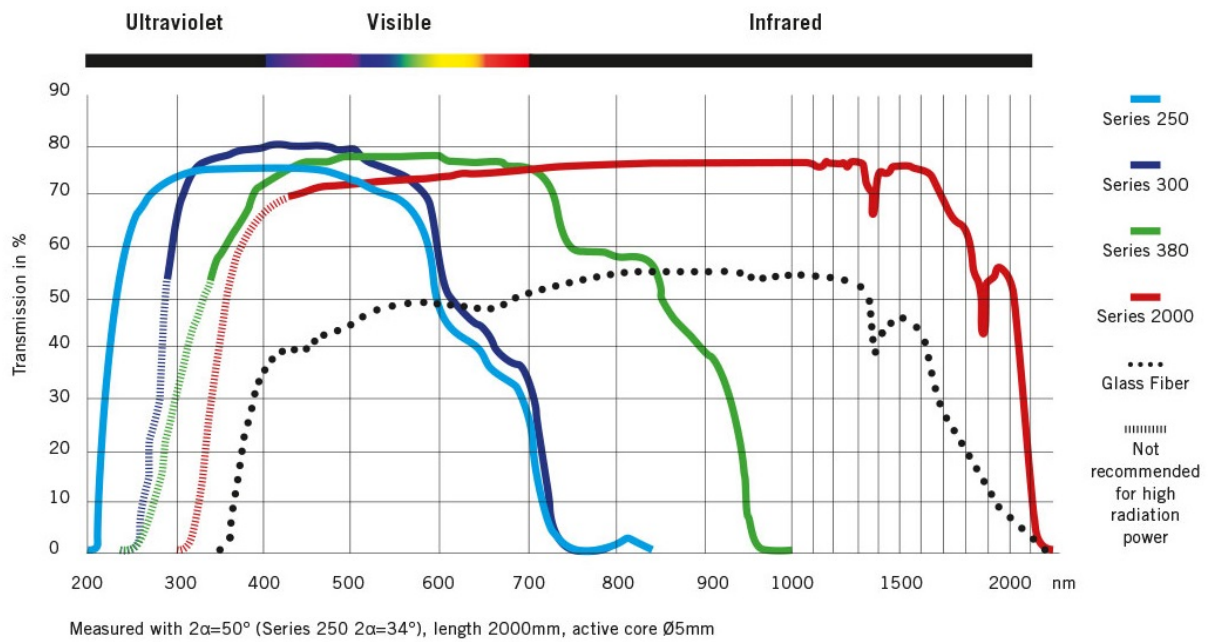


Figure 4.18: Spectral Characteristics of Liquid Light Guides

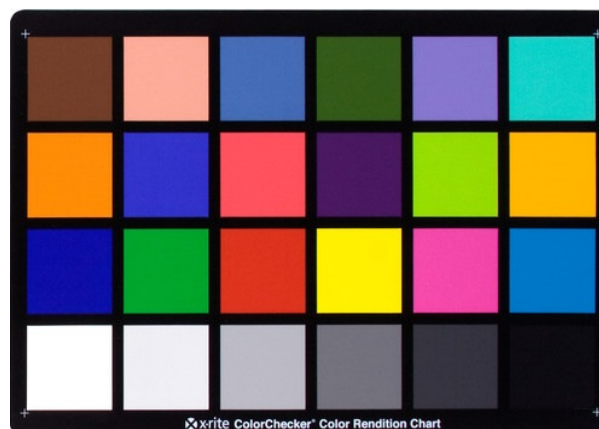
Series	Core Diameters	NA 2Cl	Application Examples and Spectrum	Specific Properties
250	3, 5, 8 mm	50°	Wafer manufacturing, curing of UV adhesives with tack free surfaces. Lengths up to 5m (15ft). 220 nm–650 nm	Outstanding photo stability even in the UVC range, suitable for high power UV lasers. Recommended light sources: Deep UV Mercury, Xenon, Excimer. Temperature range (long term): +5 °C to +30 °C
300	2, 3, 5, 6.5, 8, 10 mm	72°	UV adhesive curing and UV fluorescence inspection at lengths of up to 20 m (60 ft). 280 nm–650 nm	Superior transmission of up to 5W of UV radiation. Suitable for very rugged environments. Recommended light sources: Mercury and Xenon, Tungsten Halogen, LED. Temperature range (long term): -5 °C to + 35 °C
380	2, 3, 5, 6.5, 8, 10 mm	72°	Outstanding white light illumination at lengths of up to 30 m (100ft). 340 nm–800 nm	Excellent transmission from the near UV to the far red even at a length of 30 m. Suitable for very rugged environments. Recommended lightsources: Tungsten Halogen, LED, Xenon, Metal Halide. Temperature range (long term): -5 °C to +35 °C
2000	3, 5, 8 mm	62°	Visible and near infrared illumination. Lengths up to 4 m (12ft). 420 nm–2000 nm	Transmission of high power near infrared radiation in the multi-watt range. Integrated long pass filter for radiation below 420 nm. Recommended light sources: Xenon or Tungsten Halogen lamps, Nd-YAG or Diode Lasers. Temperature range (long term): +5 °C to +35 °C

Figure 4.19: Specifications of Liquid Light Guides

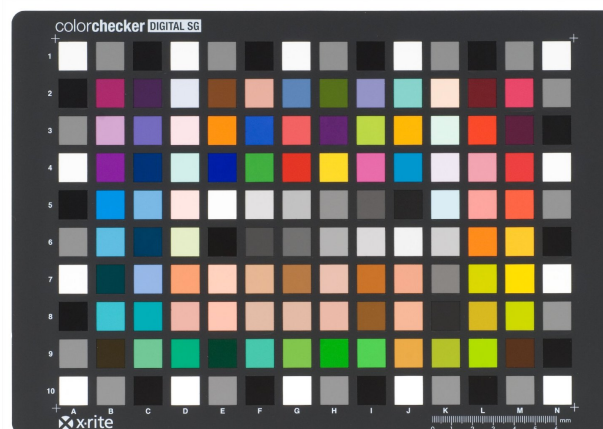
X-Rite ColorChecker[®]

The X-Rite ColorChecker[®] is a unique test pattern scientifically designed to help determine the true color balance or optical density of any color rendition system. It is an industry standard that provides a non-subjective comparison with a “test pattern” of 24 scientifically prepared colored squares. Each color square represents a natural object-human skin, foliage, blue sky, etc., providing a qualitative reference to quantifiable values. Each color will reflect light in the same way in all parts of the visible spectrum, thus maintaining color consistency over different illumination options. Some applications include spectroscopy, machine vision, photography, graphic arts, electronic publishing, and television.

The X-Rite ColorChecker[®] chart provides an easy way to recognize and evaluate the many factors that can affect color reproduction. To evaluate the effect of varying any given factor, simply compare the chart’s color image to the actual ColorChecker[®]. It is ideal for testing and standardizing color inspection and analysis systems.



(a) *X-Rite ColorChecker*[®]



(b) *X-Rite ColorChecker*[®] SG

Figure 4.20: Color Checkers

The X-Rite ColorChecker[®] SG improves on the original 24 patch design by offering a wide array of 140 colors. Specifically designed for digital photography, the X-Rite ColorChecker[®] SG provides a semi-gloss background with whiter whites, blacker blacks, and more saturated colors. Gloss gray patch targets have an extended dynamic range ($density = 2.4$) and can also be used to measure imaging noise. However, specular reflections from the gloss surface may occur for illumination geometries less than $45^\circ/0^\circ$. Matte gray patch targets have a small dynamic range ($density = 1.6$), but are more suited to narrow illumination geometries, such as those used in endoscope imaging.

Length (inches)	8
Width (inches)	11.5
Number of Patches	24
Color Patch Size	1 5/8"
RoHS	Compliant

Table 4.5: X-Rite ColorChecker[®] Specifications

Length (inches)	8
Width (inches)	11.5
Number of Patches	140
Color Patch Size	5/8"
RoHS	Compliant

Table 4.6: X-Rite ColorChecker[®] SG Specifications



Figure 4.21: X-Rite ColorChecker[®] Patch Targets Numbering

4.2.2 Calibration and Scanning Procedure

We present a hyper-spectral imaging system capable of acquiring and real-time displaying of spectral images, with 5 nm and 10 nm tuning step, in the range of 400 – 1000 nm. For the experimental tests in the context of this thesis, the spectral range selected to 450 – 700 nm. Synchronized spectral scanning and image storing enables the collection of a stack of calibrated spectral images, from which a fully resolved spectrum per image pixel can be calculated and displayed.

The instrument layout is shown in Fig. 4.22.

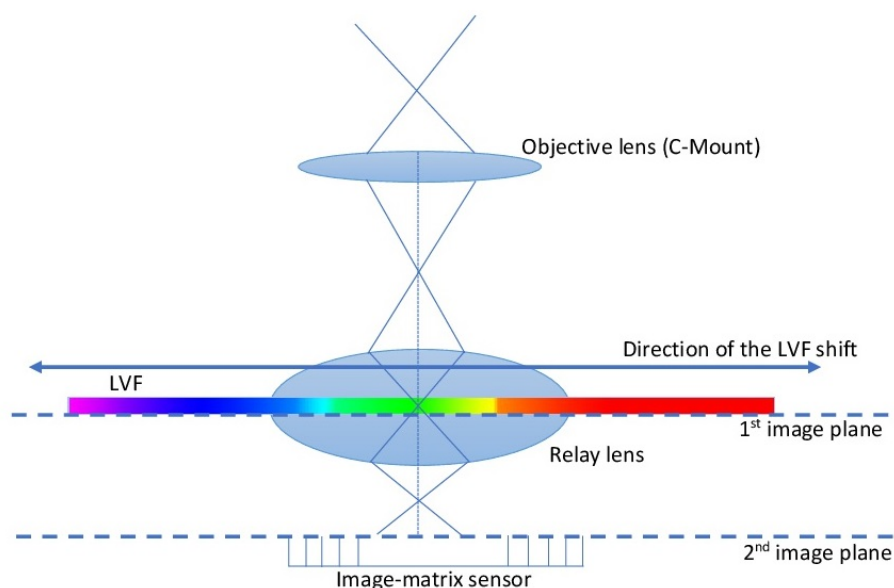


Figure 4.22: Cross sectional sketch of the proposed HSI system. Each strip of the image on the 1st image plane is filtered by the LVF. The filtered images are reproduced on the sensor by the relay lens. The whole spectrum is reconstructed strip by strip as the LVF translates.

The camera body is still, while the linearly variable filter translates. Its movement is supplied by a stepper stage with high accuracy and precision. The objective lens of the system focuses the image of a scene on an image plane. The lens is approximately telecentric image side, so as to have rays crossing the image plane within a narrow solid angle. The LVF on the 1st image plane transmits a spectral light band centered on the wavelength λ , which is continuously variable along a direction on the filter whereas remains constant orthogonally. The wavelength is changed on the image by shifting the LVF along the line where the transmission peak wavelength changes, as in Fig. 4.24. Image strips orthogonal to the shift direction are selected at the wavelength λ , for a particular position of the LVF. A relay lens, working with a 1:1 magnification ratio, transports the filtered images on the 2nd image plane, where are captured by an image-matrix

sensor. Subsequent, wavelength selections are effected through the displacement of the LVF. So, by iterating this procedure, the measurement of the spectral radiance of all the image strips is fully accomplished.

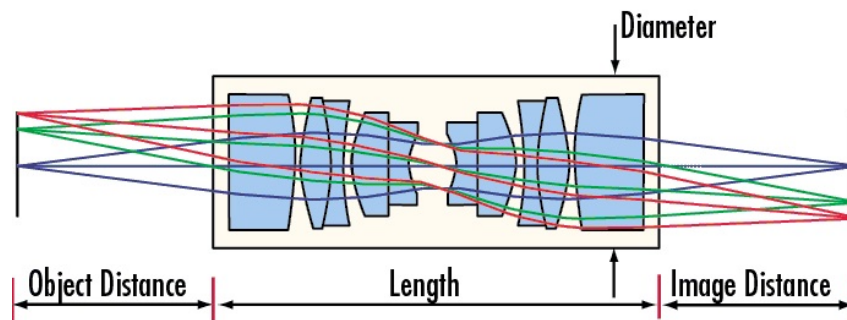


Figure 4.23: *Relay lens. The symmetry of the layout of the relay lens leaves unaltered the image quality at the 2nd image plane on the image sensor.*

This method, conveniently, allows:

1. the use of a standard relay lens
2. a simple alignment of the optical components
3. a simple arrangement of the moving LVF and of its motion supplier

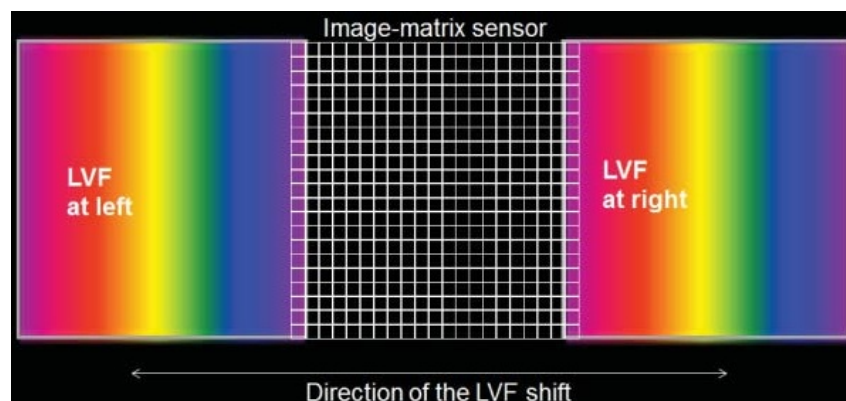


Figure 4.24: *The image-matrix sensor and the two outermost positions of the LVF. Each column of the image sensor colliding on a LVF strip is filtered at a selected wavelength depending on the filter position.*

The experimental hyper-spectral scanning procedure is conducted under darkness conditions (in a dark room), with the only light contribution that one of the selected light source. The patch targets of the X-Rite ColorChecker[®] shown in Fig. 4.26, are chosen to be the target of scanning.

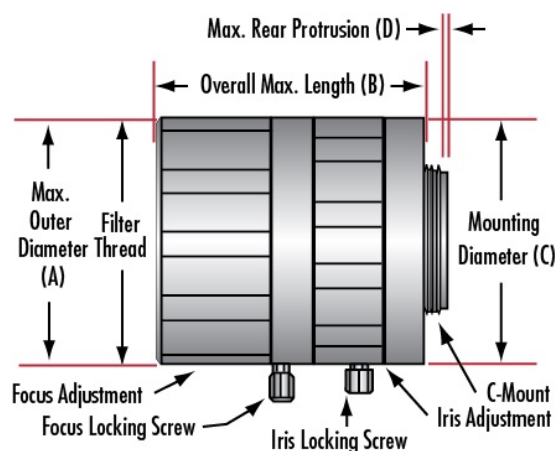


Figure 4.25: Objective (C-mount) lens. The objective lens creates an image of a scene where it has to provide almost uniform. This is achieved with almost parallel, to the optical axis, off-axis chief ray directions. Besides good correction of aberrations in the visible light, the lens must be well corrected for distortion, to accomplish pixel correspondence on the image.

The image acquisition with this system is completely computer controlled, so that the linearly variable filter is being moved automatically in front of the image sensor. The step of the filter movement depends on the wavelength tuning step of the scanning procedure. For 10 nm tuning step, the step of the filter movement responds to 2 mm on the stepper stage, while for 5 nm tuning step, it responds to 1 mm on the stepper stage. It needs to be mentioned that the procedure starts when the filter covers an initial small part of the image sensor and ends up when the whole filter has passed through it. In this way, a complete hyper-spectral cube of images is obtained.

From Fig. 4.24, it can be seen that the LVF travels step by step from left to right, while filtering the light that activates the pixels of each matrix column at the wavelength associated with the superimposed column of the filter itself. Any captured image is constituted by pixel columns, filtered at different wavelengths.

Specially developed software is employed for the control of the HSI system as well as for the spectral image analysis. The system operates in two modes: the view and the acquisition mode. The former enables the selection and real-time visualization of desired spectral images, while the latter performs synchronized spectral scanning and image capturing, and calculation of one full spectrum per image pixel. In both cases, a special calibration procedure, [33], is executed prior to these imaging procedures, in order to compensate for the wavelength dependence of the response of the electro-optical parts of the system, such as CMOS, illuminators, etc.

The quantum efficiency of the CMOS detector as well as the spectral emissivity of the light source are changing with the wavelength in the spectral range of interest. Consequently, the

brightness and the dynamic range of the captured images change with the wavelength. Quantitative assessment of the intensity of the backscattered light in several spectral bands requires compensation for the above factors.

A Ba_2SO_4 white plate with unity reflectance across the 400 – 1000 nm spectral range is used as calibration specimen. The specimen is placed in the field-of-view (FOV) of the lens and the gray value of the central area of the image is displayed in real-time. Then the monochromator scans the total spectral range and in each tuning step the camera shutter and gain is automatically regulated, so that the displayed gray value approaches the value of 255. This ensures that the dynamic range of the CMOS is fully exploited. The shutter and gain values, used to obtain a 255 gray level, are stored in each wavelength-tuning step, together with the image of the white specimen constituting the calibration data set of the system. These settings are determined the sensitivity level of the camera, which increases as the imaging wavelength is tuned to shorter or to longer wavelengths than the wavelength range at which the maximum light throughput and efficiency of the system is obtained. This makes the system's response almost independent from the wavelength.

By choosing the acquisition mode, which follows the calibration procedure, the system performs synchronized tuning of the imaging wavelength and image capturing and storing of the area under analysis. In each step, the sensitivity of the camera is automatically regulated according to the stored shutter and gain values. From the stored stack of spectral images, a spectrum can be calculated and displayed in any user-selected spatial point of the image. The spectra are calculated from the gray values of the selected pixel spectral column. The spatial resolution of the detector determines the number of the spectra that can be collected in one experiment run. With the described configuration, 6.5 million (3096×2080 sensor's resolution) spectra can be collected at approximately two minutes scanning time.

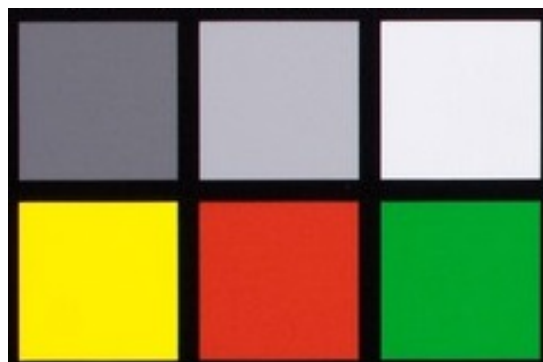


Figure 4.26: X-Rite ColorChecker[®] patch targets of scanning procedure.

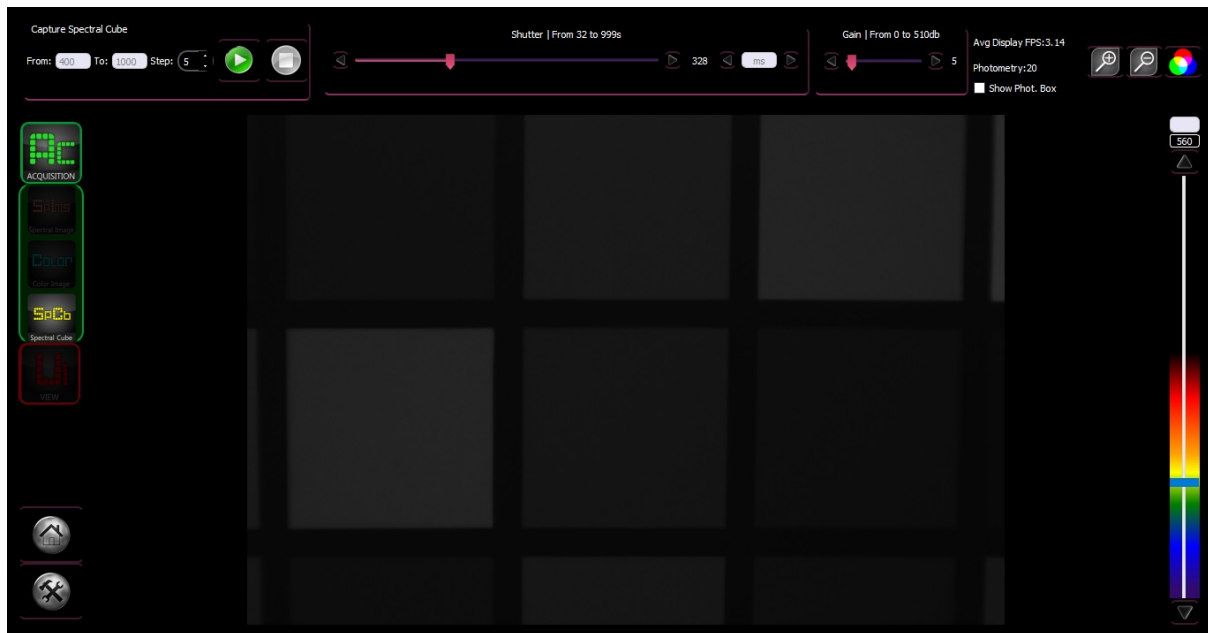


Figure 4.27: Acquisition mode - Scanning procedure

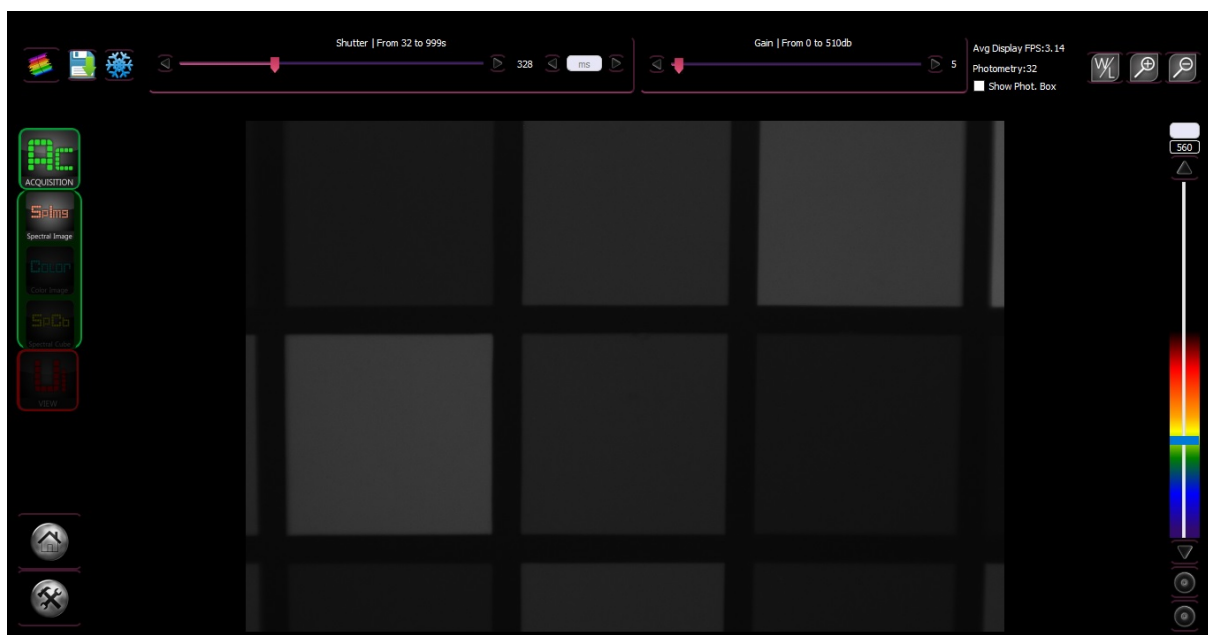


Figure 4.28: Acquisition mode - Capture spectral image at preferred wavelength

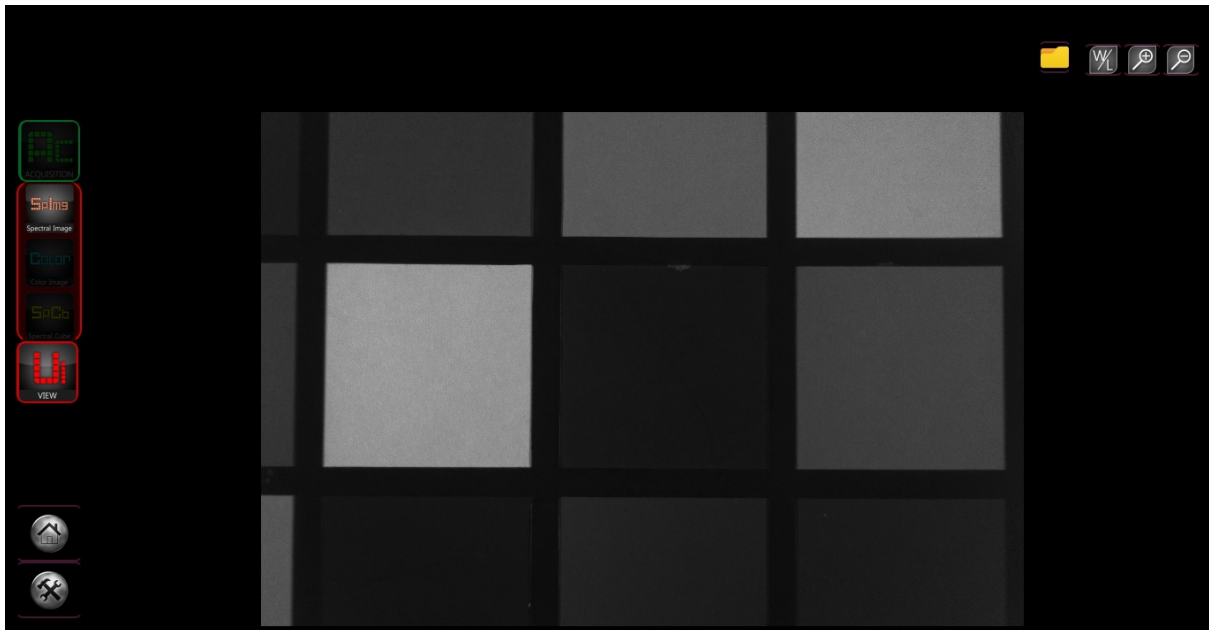


Figure 4.29: View mode - View preferred acquired spectral image

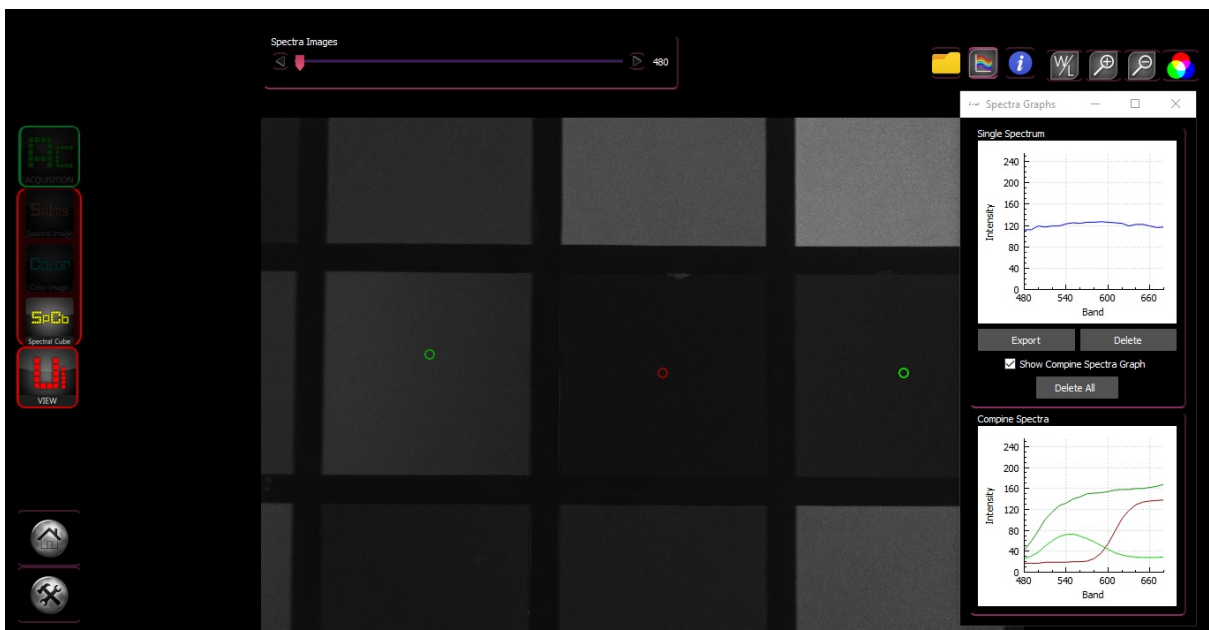


Figure 4.30: View mode - View acquired spectral cube & spectra per pixel

Chapter 5

Spectral Cube Reconstruction Methods

5.1 Introduction

We consider the problem of the reconstruction of spectral reflectance curves from hyper-spectral images. The pixel value in a hyper-spectral image is the result of:

1. the spectral interaction of the light radiant distribution with the reflectance of an object surface
2. the spectral sensitivity of the camera combined with the transmittance of the optical path including the filter

Retrieving the spectral reflectance function of the object surface at each pixel is highly desirable. We call this process spectral reflectance reconstruction or simply spectral reconstruction. It allows an intrinsic representation of an object surface property which is independent from light spectral distribution and from the spectral sensitivity of the camera used for the hyper-spectral image acquisition.

5.2 Related Work

There are several methods used for the reconstruction of spectral reflectance from hyper-spectral images. The technique described at [35] uses neural networks to estimate a probability distribution which is treated a posteriori to obtain a solution of the problem to be solved. The aim of the aforementioned project was the estimation of the spectral reflectance of pigments from

multi-spectral images of canvas paintings. The reconstruction of spectral curves takes place in the visible domain of the spectrum. Each curve considering as a sequence of s regularly sampled values taken from 400 nm to 760 nm at constant d nm intervals.

The main problem was the construction of a system that maps a vector c containing the camera values to a vector s representing a sampled spectral curve. As long as a sufficient large set of pairs (c, s) are known, this problem can be solved by the construction of a Mixture Density Network (MDN) system from this data.

In this context, the probability $prob(s|c)$ becomes the conditional probability of a spectral curve s being obtained from a particular camera response vector c . By minimizing the negative logarithm of the likelihood over a database of training pairs (c, s) , the weights of the neural network of the MDN can be fixed. Once the neural network trained, the MDN provides a mapping between a camera response vector c and a parameter vector v .

$$v = \{\alpha_1, \dots, \alpha_m, \sigma_1, \dots, \sigma_m, \mu_1, \dots, \mu_m\} \quad (5.1)$$

where m is the number of Gaussians used, α_i are mixing coefficients, σ_i are scalars for the standard deviation and μ_i are vectors of dimension s representing the centers of the multidimensional Gaussian functions.

The purpose is to find a single sampled spectral curve s that provides the best estimation given a vector c . So there is a need to choose a way to extract this vector s from the mixture model presented by the parameter vector v .

Maximizing the obtained conditional density would give the vector s with highest probability. The strategy used is to keep as solution the vector s associated to the Gaussian with bigger mixing coefficient:

$$\max_i \alpha_i(c) \quad (5.1)$$

such that $s = \mu_i(c)$. Then s corresponds to the centre of the dominant Gaussian function in the Mixture model. A graphical summary of the method is shown in Fig. 5.1.

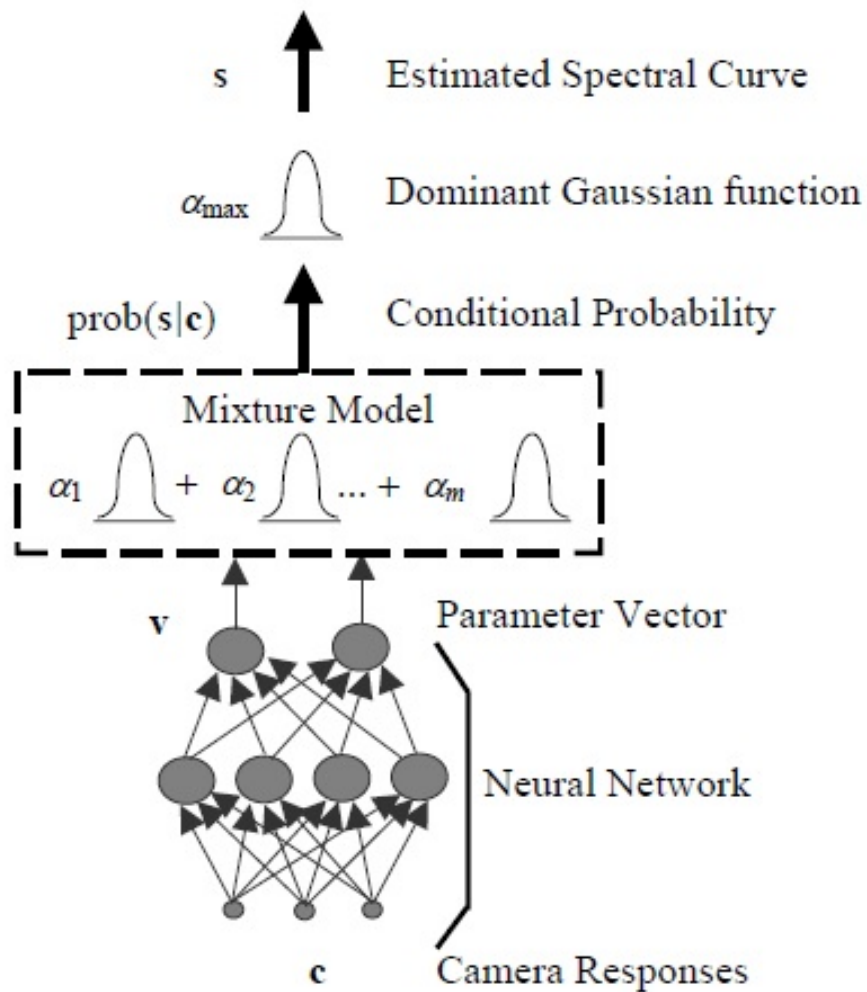


Figure 5.1: MDN spectral reflectance curve estimation

5.3 Tomographic Reconstruction Method

The main purpose of the reconstruction algorithm is to provide images that correspond to a single specific wavelength across the whole region of the scanned area of the filter. The images captured by the aforementioned hyper-spectral scanning procedure, except of the first and the last one, contain a great many of spectral bands on account of the serial movement of the linearly band-pass filter. In other words, the algorithm that is going to be developed, needs to be able to pinpoint and separate the different spectral bands in the consecutive images. After having successfully completed the separating section, the founded same bands in the hyper-spectral images must be processed and appropriately connected in order to result in the reconstruction of the initial target-image and thus, the acquisition of the reconstructed spectral cube.

In this point, it is important to state the criterion upon which the separation of different spectral bands takes place and the kind of connection that is required. As we mentioned above, the step of the filter movement depends on the tuning step of the scanning procedure. In this scanning procedure, the tuning step was set to 5 nm, which is translated to 1 mm step of the filter movement on the stepper stage. So, the step of the filter movement is corresponded to 387 columns, approximately, of each new scanned image. Being more specific, a step of 1 mm of the filter movement through the image sensor is algorithmically translated to a shift of 387 columns between two consecutive scanned images.

The construction of the final spectral cube is based on the diagonal connection of the spectral bands. This kind of connection refers to three different phases of scanning, that one till the total covering of image-target by the filter, that of total covering and that of uncovering. As far as the till-covering part is concerned, each image adds a fixed number of columns to the reconstruction till the maximum number of columns, provided by the type of image sensor used, is reached, whereas, the same number of columns are subtracted during the till-uncovering process.

Fig. 5.2 lends valuable insight to the conceptualization of the algorithmic concept mentioned above. In particular, it demonstrates the consecutive steps of filter leftwise or rightwise through the image sensor that should be pinpointed in the scanned images. Then, the following diagonal incorporation of all covering phases results in the reconstructed cube.

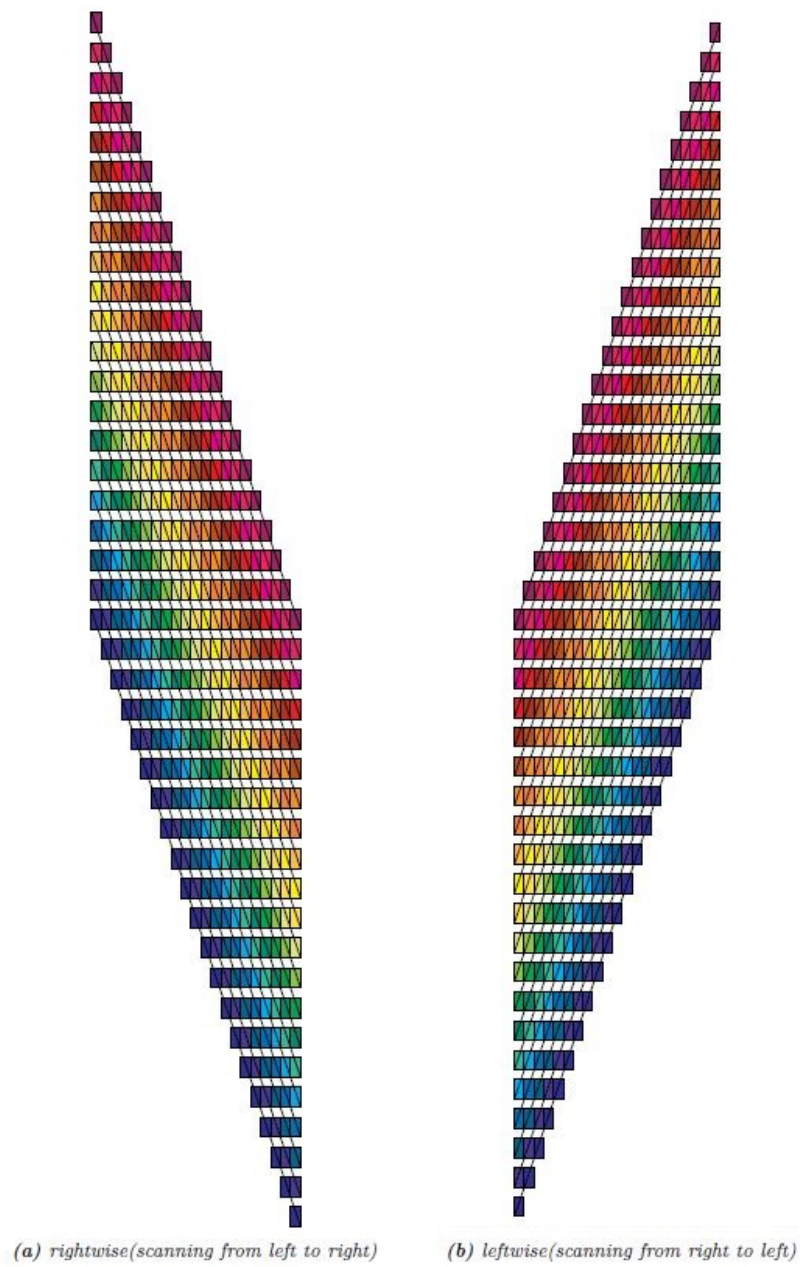


Figure 5.2: Schematic Diagonal (Tomographic) Reconstruction of Spectral Cube.

5.3.1 Acquired Spectral Cube Images

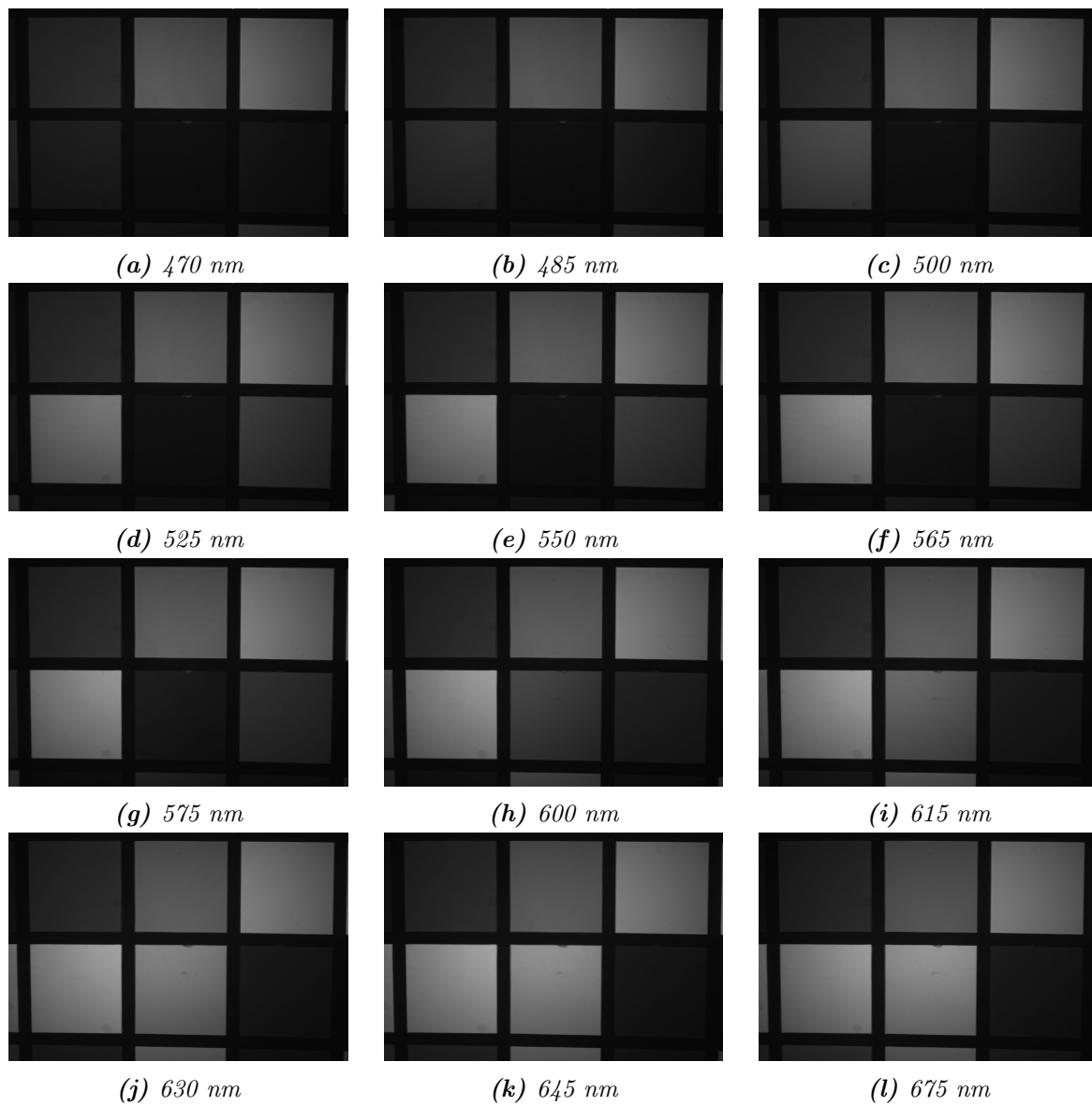


Figure 5.3: Acquired spectral images \mapsto 5 nm tuning step.

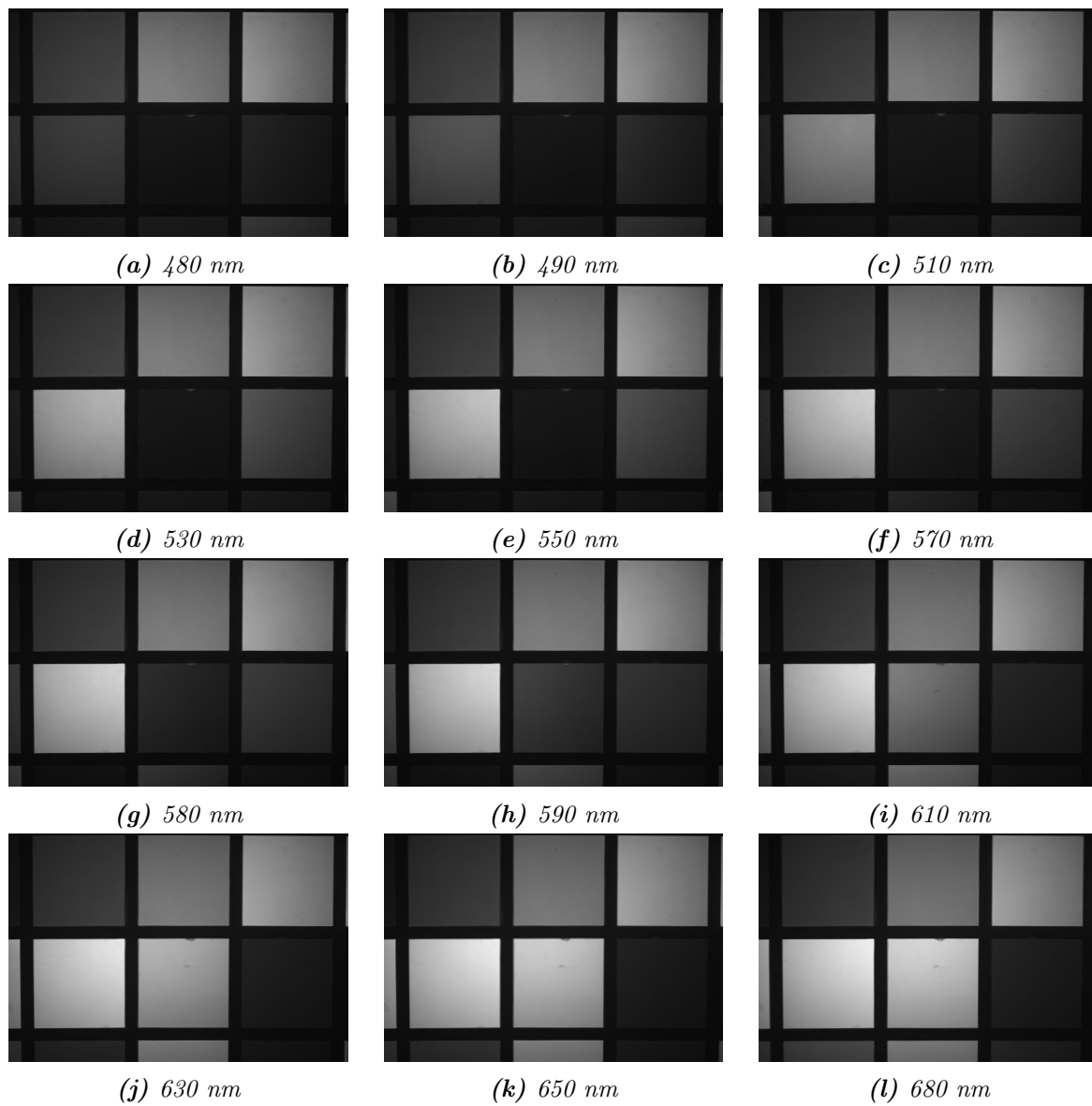


Figure 5.4: Acquired spectral images \mapsto 10 nm tuning step.

5.3.2 Reconstructed Spectral Cube Images

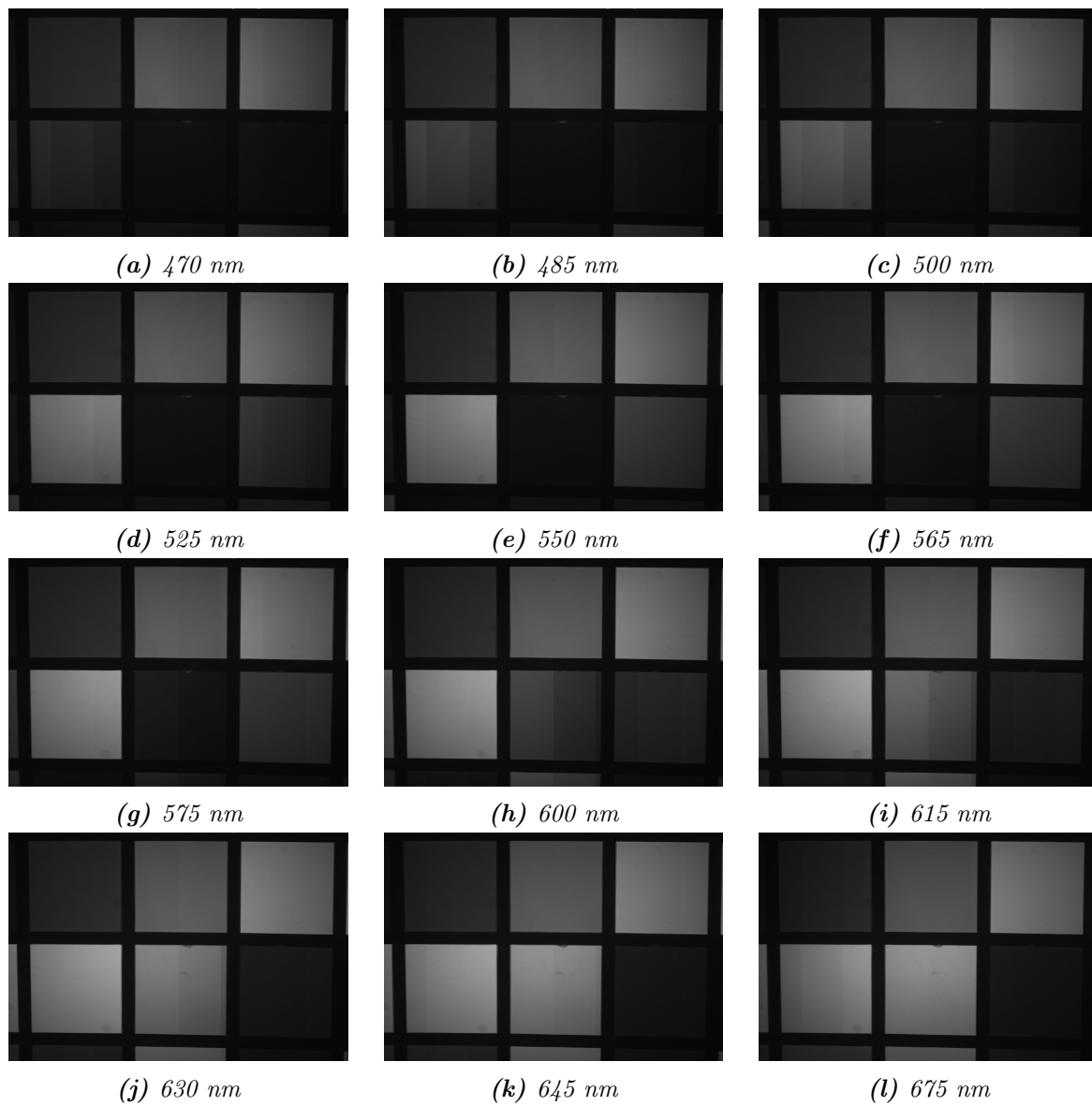
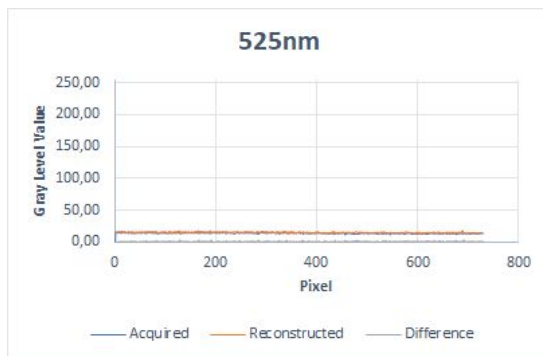
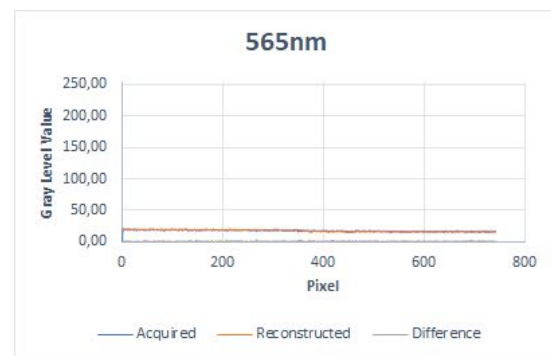


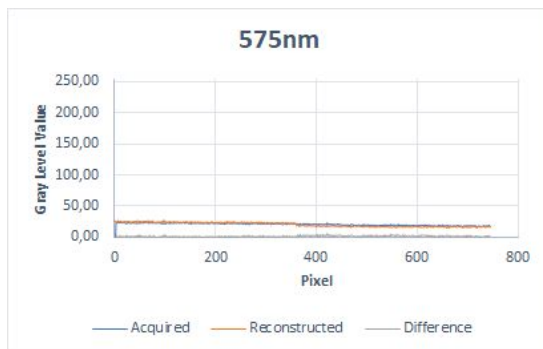
Figure 5.5: Reconstructed spectral images from 5.3 acquired spectral images with tomographic reconstruction.



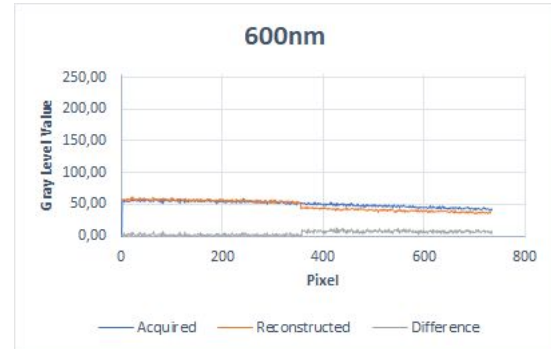
(a) Acquired image angle = -0.00192 ,
Reconstructed image angle = -0.00199



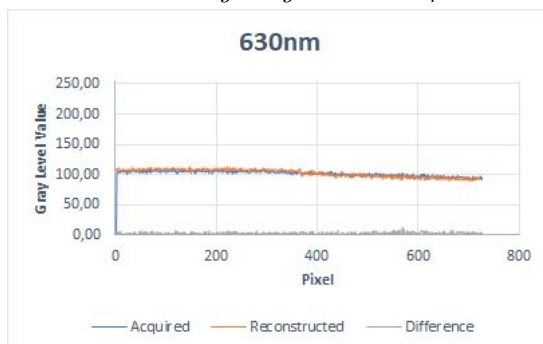
(b) Acquired image angle = -0.00517 ,
Reconstructed image angle = -0.00692



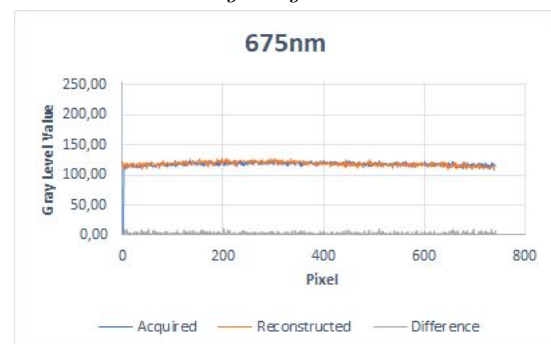
(c) Acquired image angle = -0.00838 ,
Reconstructed image angle = -0.0134



(d) Acquired image angle = -0.0209 ,
Reconstructed image angle = -0.0379

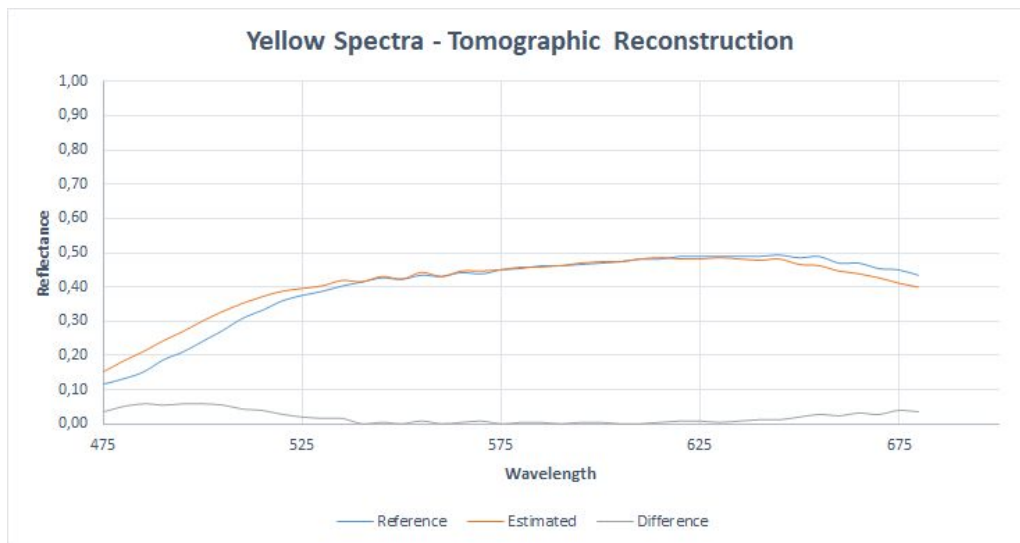


(e) Acquired image angle = -0.0178 ,
Reconstructed image angle = -0.0292

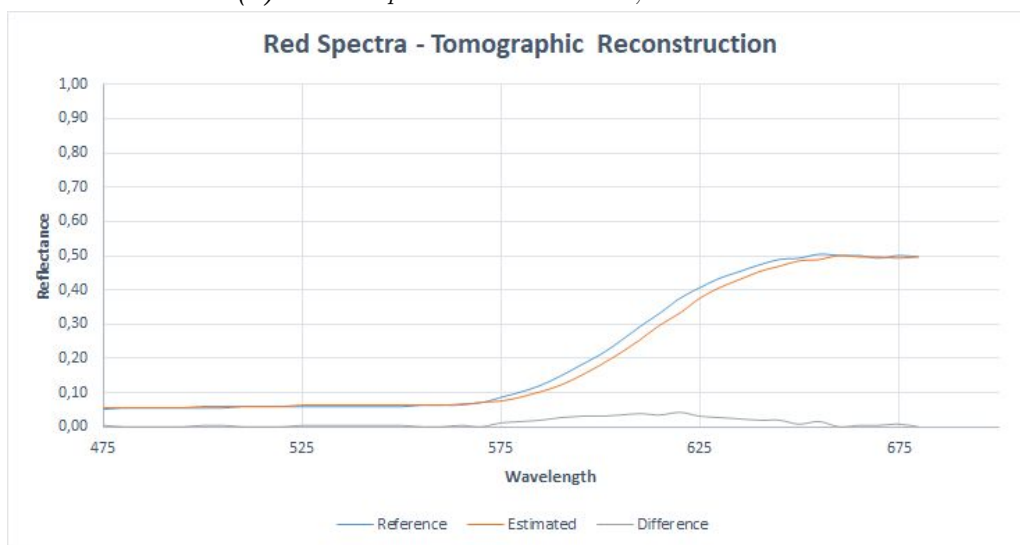


(f) Acquired image angle = -0.00094 ,
Reconstructed image angle = -0.00624

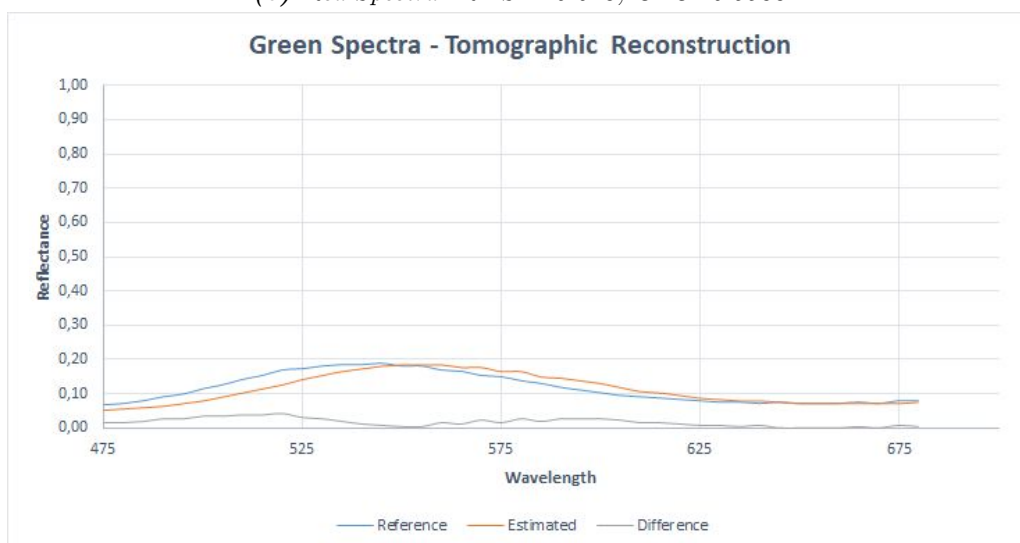
Figure 5.6: Spatial profiles of a row for the red patch target from 5.3 with tomographic reconstruction.



(a) Yellow Spectra. $RMSE=0.028$, $GFC=0.9978$



(b) Red Spectra. $RMSE=0.018$, $GFC=0.9988$



(c) Green Spectra. $RMSE=0.021$, $GFC=0.9855$

Figure 5.7: Reference and estimated spectra from 5.3 with tomographic reconstruction.

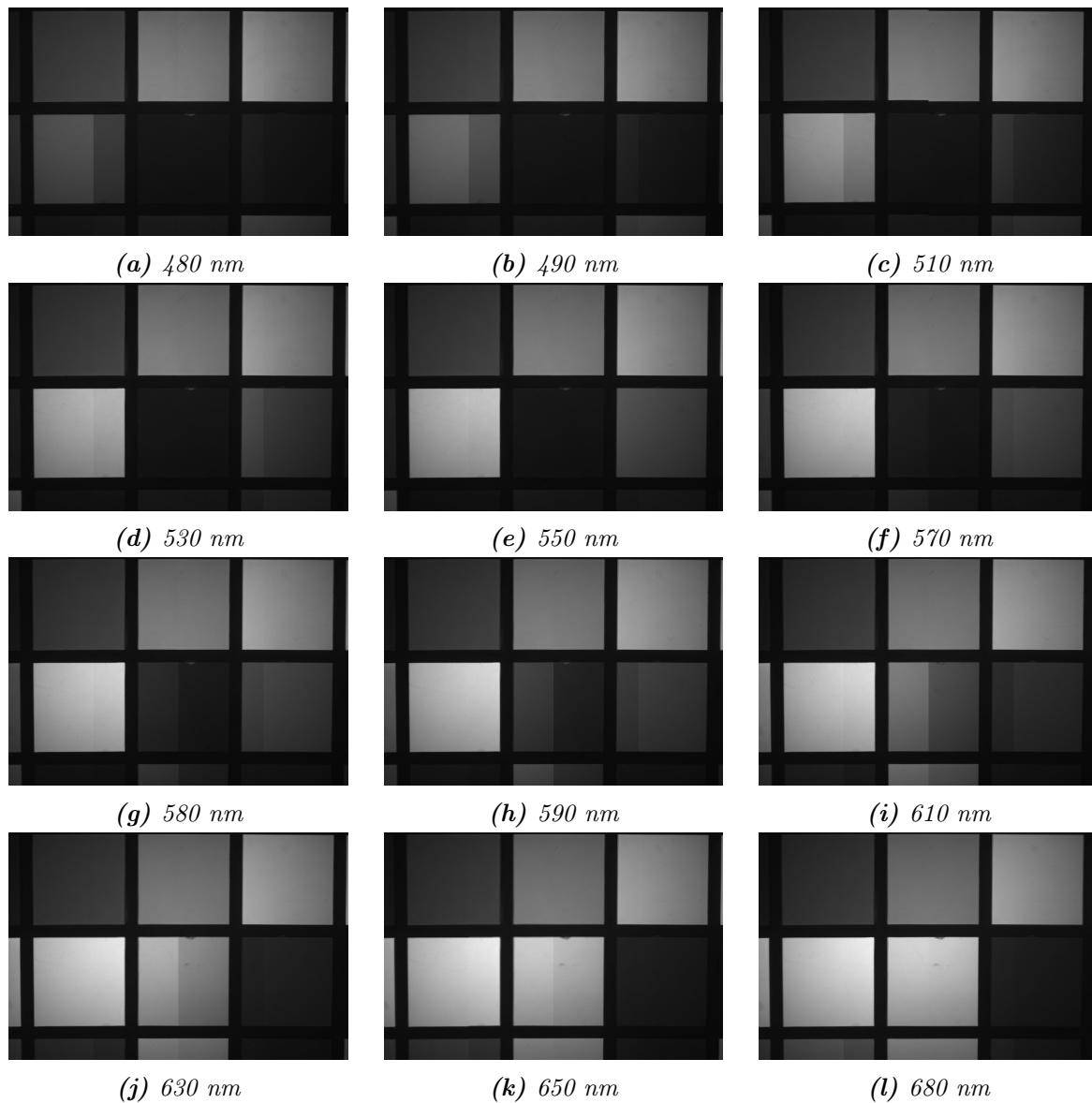
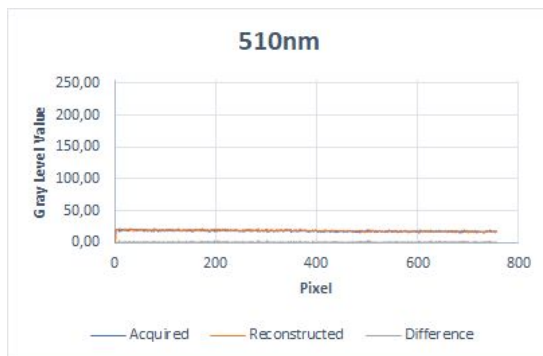
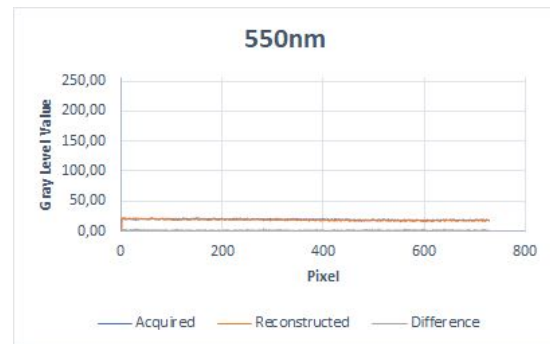


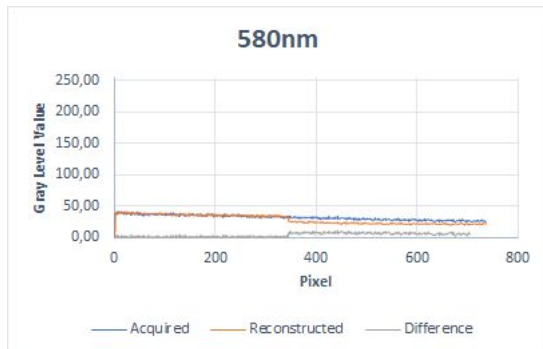
Figure 5.8: Reconstructed spectral images from 5.4 acquired spectral images with tomographic reconstruction.



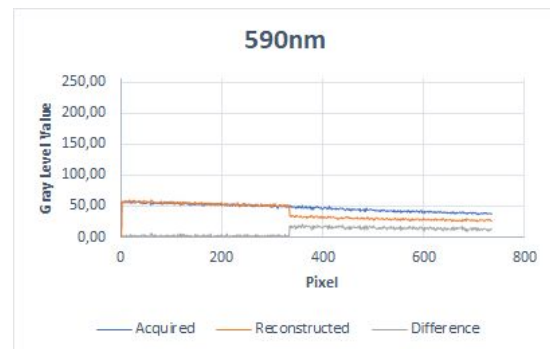
(a) Acquired image angle = -0.0034 ,
Reconstructed image angle = -0.0046



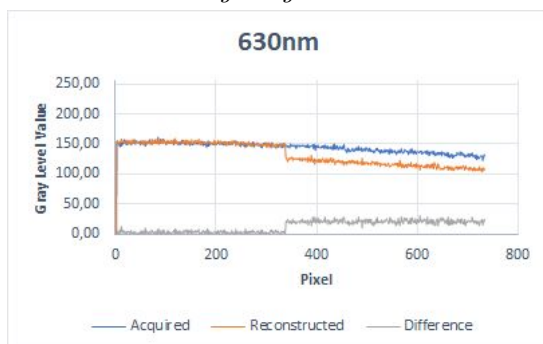
(b) Acquired image angle = -0.0039 ,
Reconstructed image angle = -0.0044



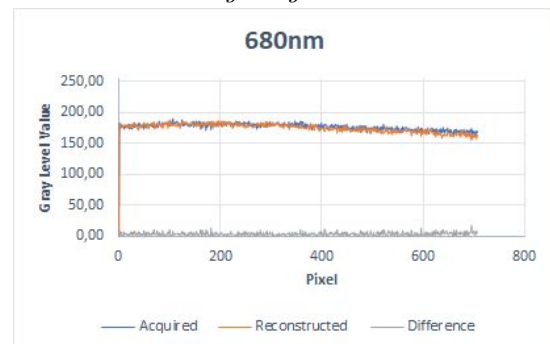
(c) Acquired image angle = -0.0177 ,
Reconstructed image angle = -0.0307



(d) Acquired image angle = -0.0276 ,
Reconstructed image angle = -0.0539

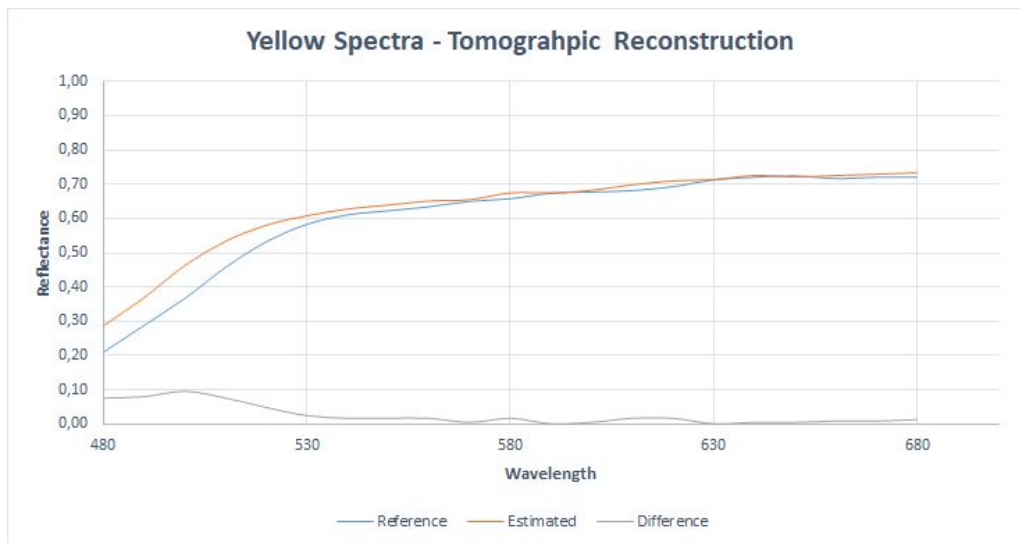


(e) Acquired image angle = -0.033 ,
Reconstructed image angle = -0.080

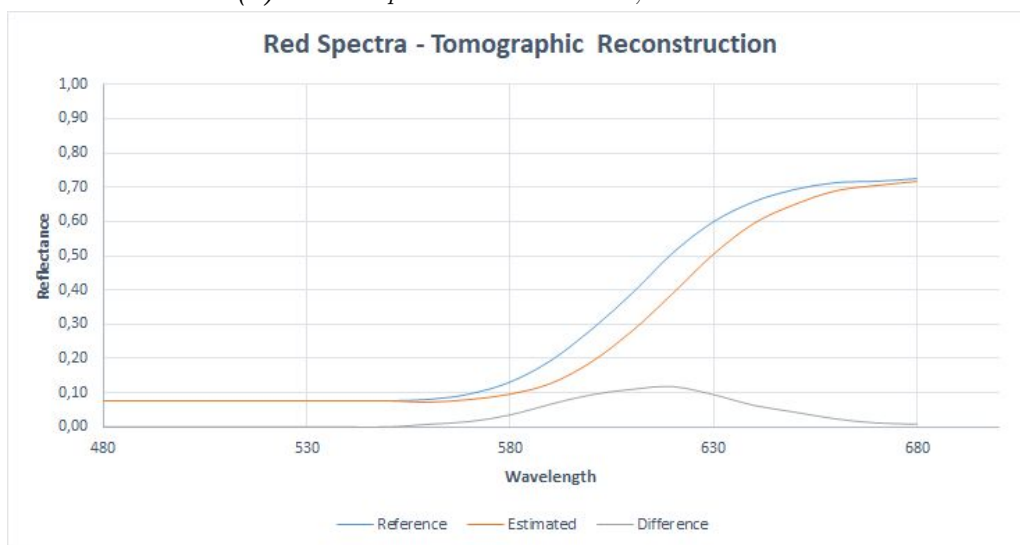


(f) Acquired image angle = -0.0183 ,
Reconstructed image angle = -0.026

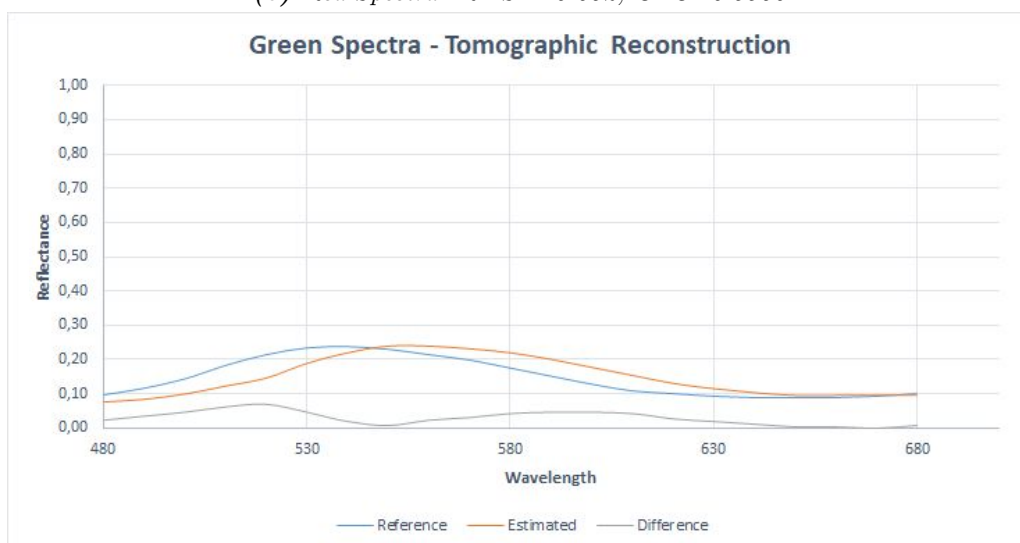
Figure 5.9: Spatial profiles of a row for the red patch target from 5.4 with tomographic reconstruction.



(a) Yellow Spectra. $RMSE=0.038$, $GFC=0.9986$



(b) Red Spectra. $RMSE=0.052$, $GFC=0.9950$



(c) Green Spectra. $RMSE=0.036$, $GFC=0.9747$

Figure 5.10: Reference and estimated spectra from 5.4 with tomographic reconstruction.

5.4 Reconstruction Method based on Image Interpolation

This reconstruction method serves the same purpose as the first one, that is to provide images that correspond to a single specific wavelength across the whole region of the scanned area of the filter. The algorithm that is going to be developed based on image interpolation. As mentioned in chapter 2, interpolation is the process of determining the values of a function at positions lying between its samples. This process achieved by fitting a continuous function through the discrete input samples. In terms of digital image, the process of interpolation is to find the information for undefined pixels or missed pixels in an image based on the information provided by given pixels, so that the interpolated image is as close to the actual one as possible. The given information can be anything, such as x or y coordination, color, gray level or density.

This method for the reconstruction of the spectral cube is based on the information provided by the reference spectra, each of them consists of different sampled points. Using this information we can reconstruct the spectrum for every pixel of the imaged scene, and in this way we reconstruct spectral images from the spectra. In our experiments, we used both linear and spline interpolation and we compare the results of the two methods. Having the acquired spectral cube, with tuning steps 5 nm and 10 nm, we used the aforementioned interpolation methods to compute the information for undefined pixels in the images. In particular, we used the sampled gray level values of the image pixels and the associated wavelength bands as input of the interpolation algorithm. The interpolation algorithm computes the pixel gray level values for the whole spectral region of the scanned area of the filter (450 to 700 nm) with spectral resolution of 1 nm. In this way, now, we have spectral information (a full spectrum) for every pixel of the scene. Using the information provided by the interpolation algorithm we obtain the reconstructed spectral cube consisted of a stack of images each one captured at a different wavelength.

There are two implementations of the algorithm. The first one based on linear interpolation, while the second one on spline interpolation. Linear interpolation is the simplest method of getting values at positions in between the data points. The points are simply joined by straight line segments. Each segment (bounded by two data points) can be interpolated independently. This interpolation method results in discontinuities at each point, and often a smoother interpolating function is desirable. Splines are piecewise polynomials with pieces that are smoothly connected together. Since the cubic spline provides the best trade-off between performance and computation efficiency in spline families, it is the most often used in practice. Cubic spline interpolation is a fast, efficient and stable method that offers true continuity between the segments. As such it requires more than just the two endpoints of the segment, but also the two points on either side of them. Apparently, it has better response in both pass-band and stop-band comparing with the linear function. It is, also, very special since the coefficients are chosen to give a smooth transition as we pass from one point to the next. This smooth behavior is

accomplished by computing the polynomial coefficients for each interval using more than just the adjacent data points.

5.4.1 Acquired Spectral Cube Images

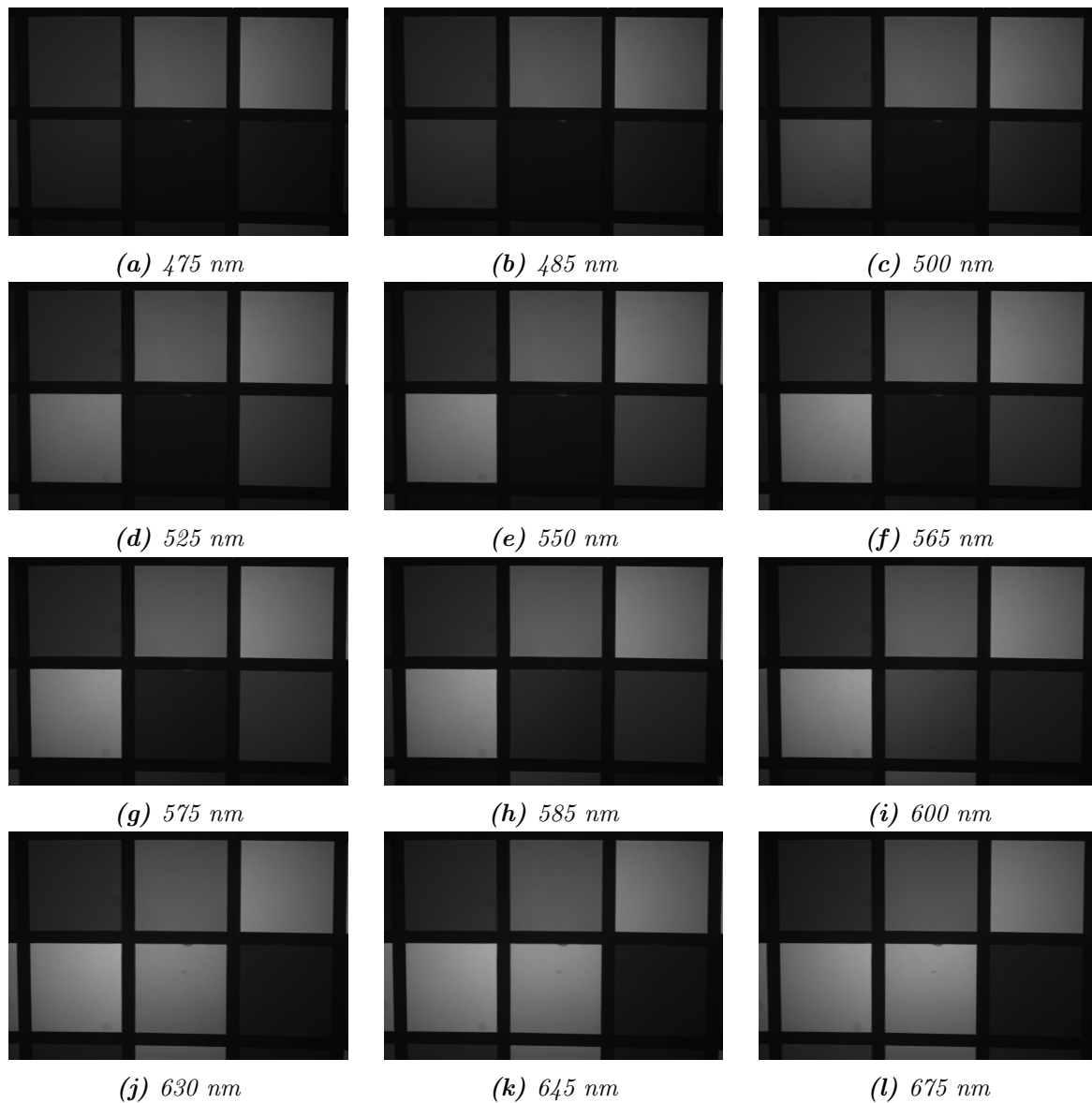


Figure 5.11: Acquired spectral images \leftrightarrow 5 nm tuning step.

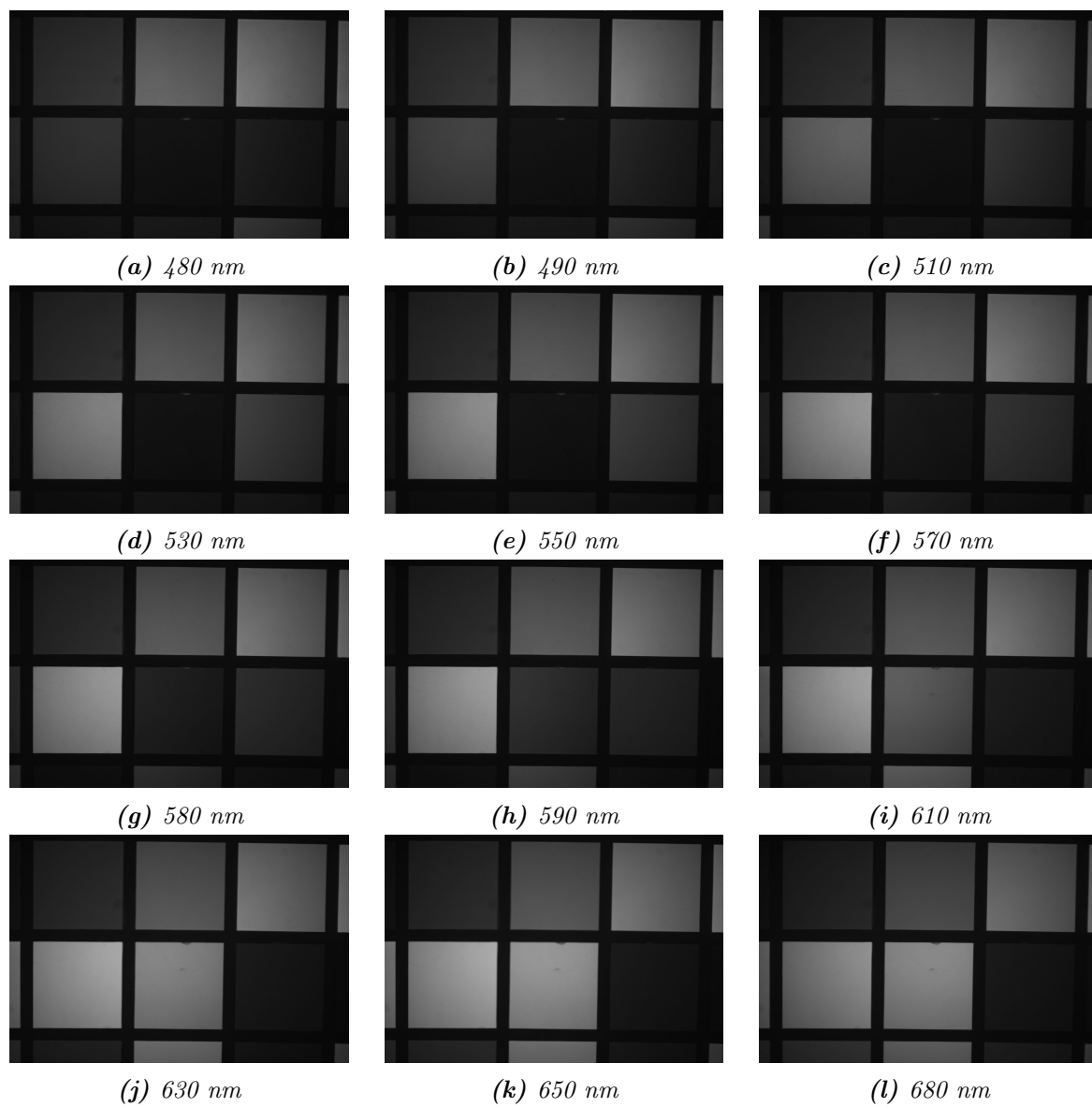


Figure 5.12: Acquired spectral images \mapsto 10 nm tuning step.

5.4.2 Reconstructed Spectral Cube Images

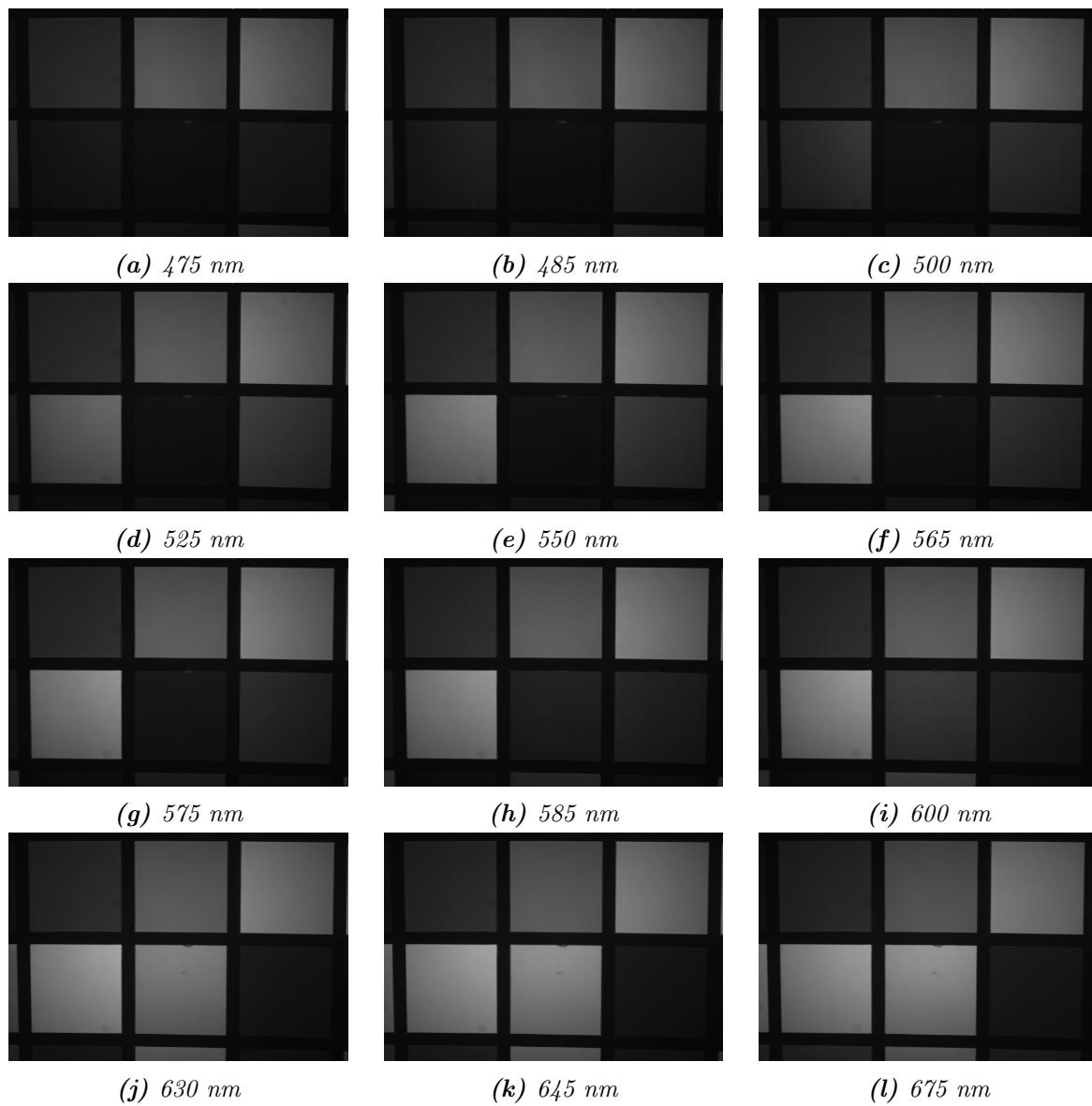
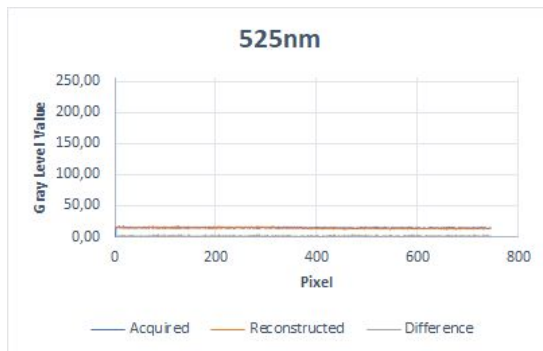
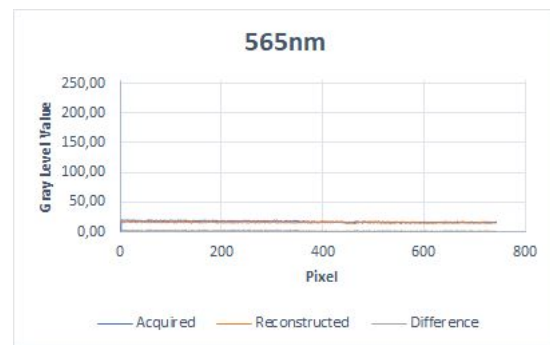


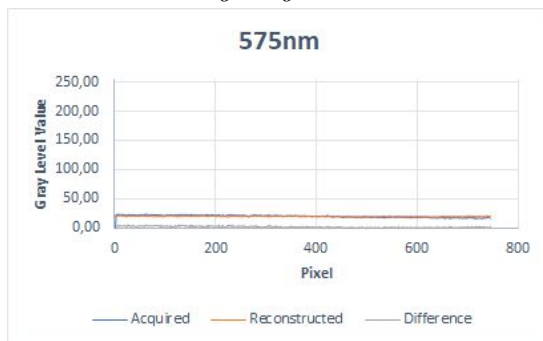
Figure 5.13: Reconstructed images from 5.11 acquired spectral images with linear interpolation.



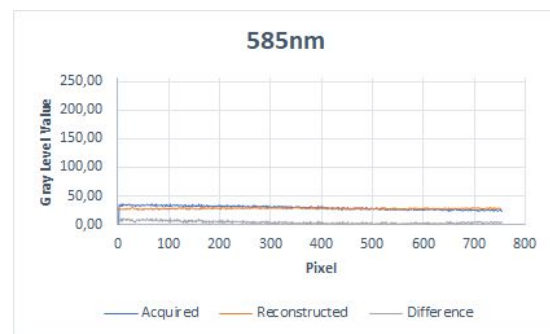
(a) Acquired image angle = -0.00196 ,
Reconstructed image angle = -0.00192



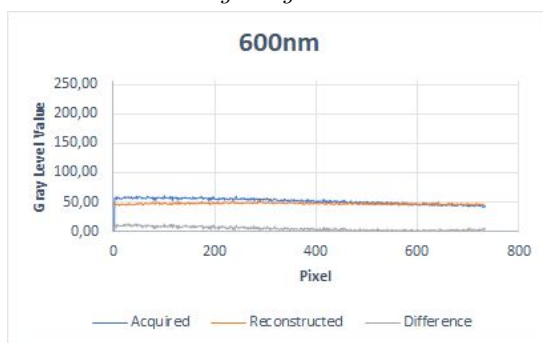
(b) Acquired image angle = -0.00517 ,
Reconstructed image angle = -0.00153



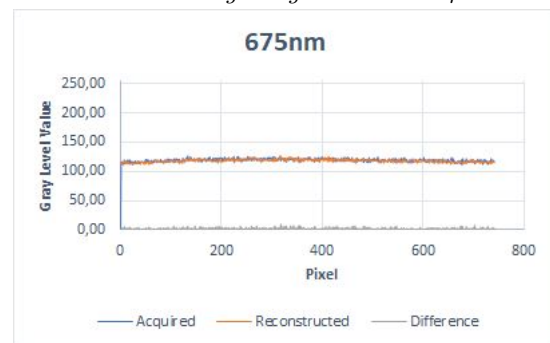
(c) Acquired image angle = -0.0083 ,
Reconstructed image angle = -0.0012



(d) Acquired image angle = -0.0014 ,
Reconstructed image angle = -0.00004

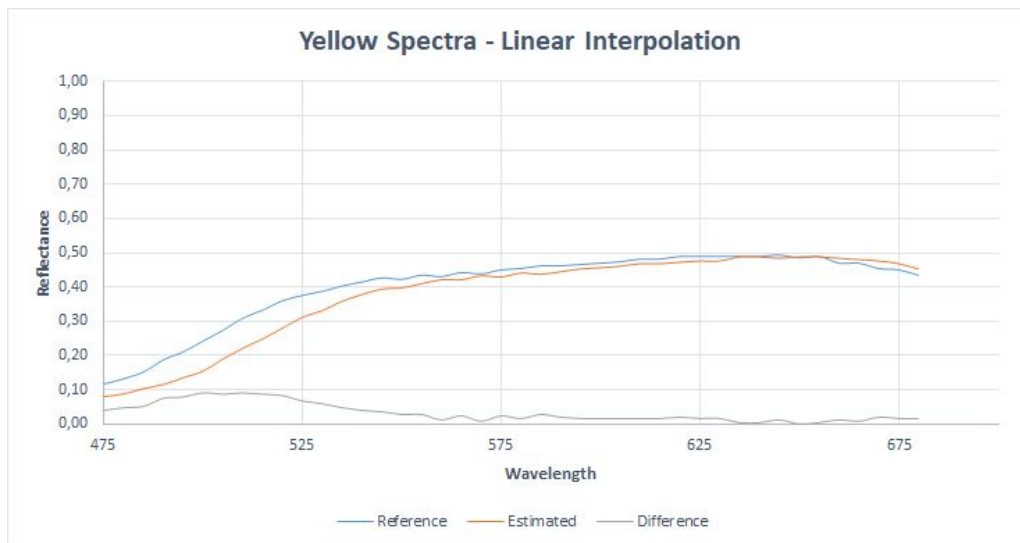


(e) Acquired image angle = -0.02 ,
Reconstructed image angle = -0.002

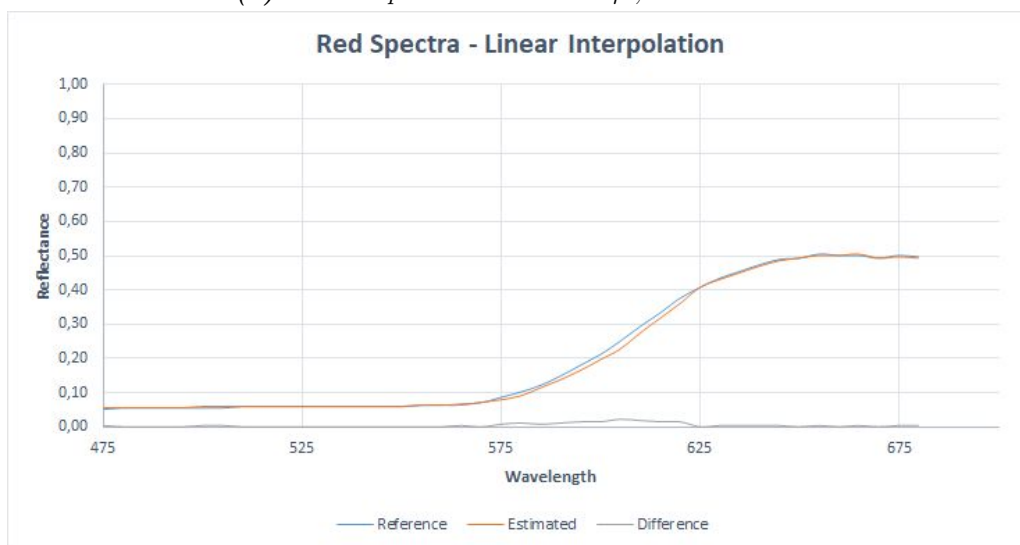


(f) Acquired image angle = -0.0009 ,
Reconstructed image angle = -0.0006

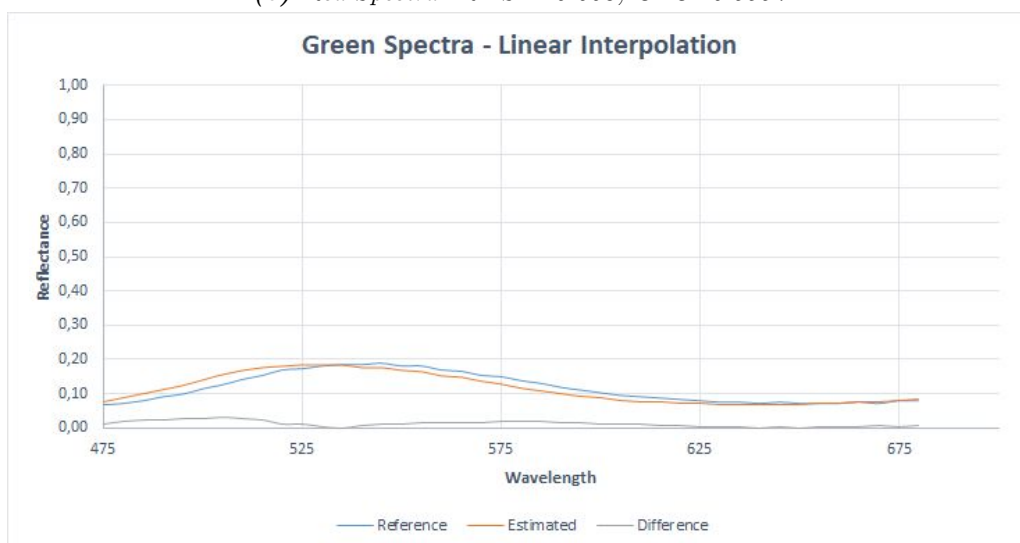
Figure 5.14: Spatial profiles of a row for the red patch target from 5.11 with linear interpolation.



(a) Yellow Spectra. $RMSE=0.043$, $GFC=0.9959$



(b) Red Spectra. $RMSE=0.008$, $GFC=0.9997$



(c) Green Spectra. $RMSE=0.015$, $GFC=0.9926$

Figure 5.15: Reference and estimated spectra from 5.11 with linear interpolation.

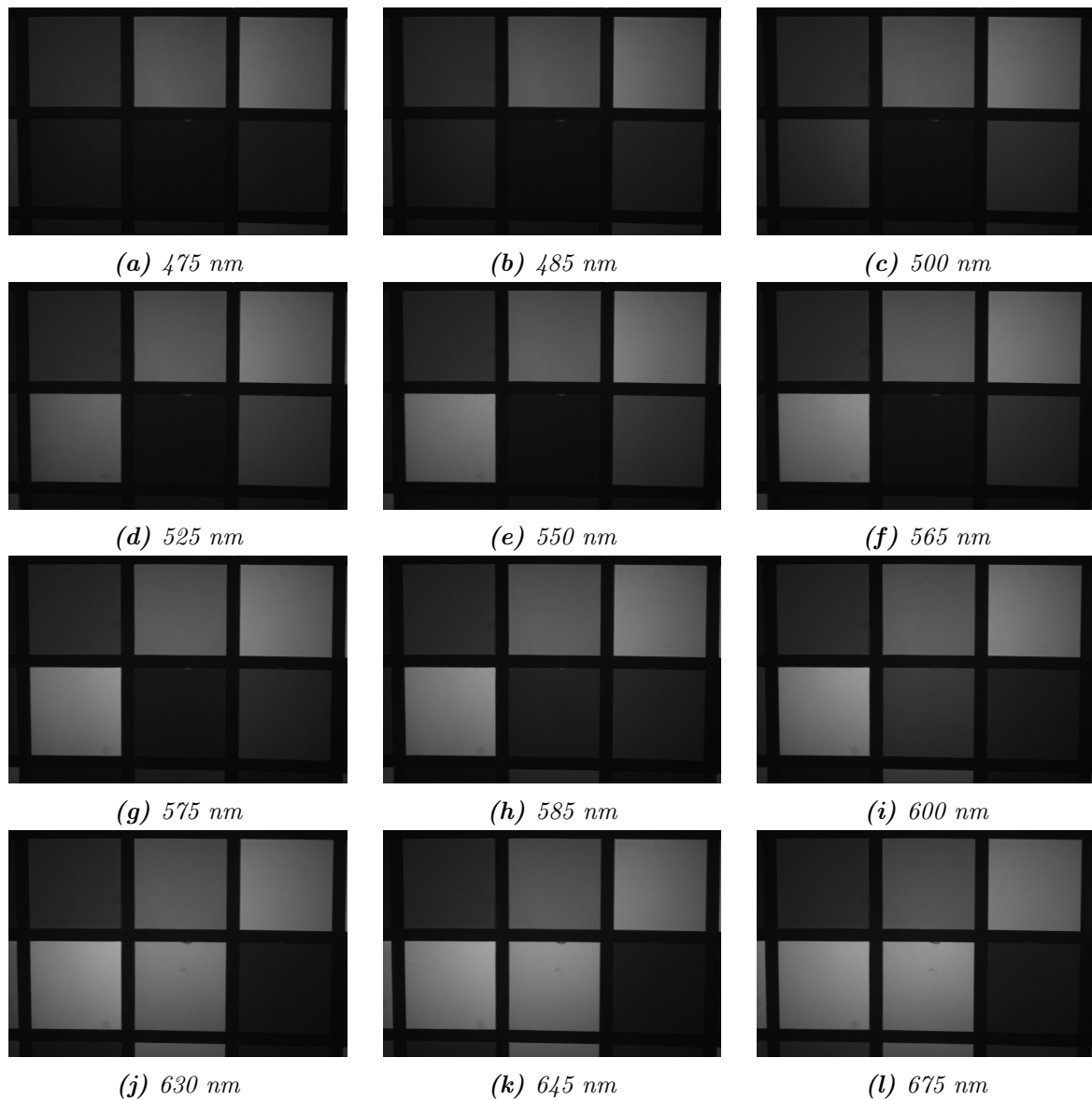
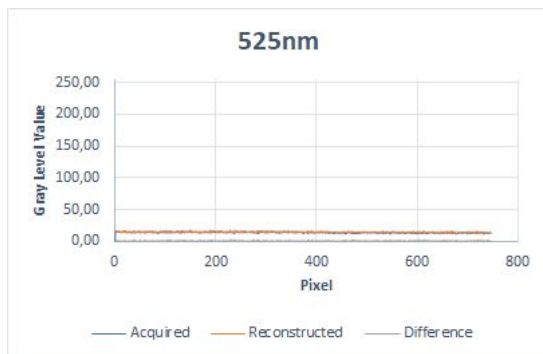
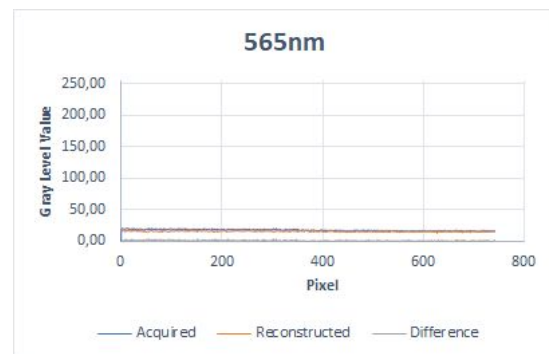


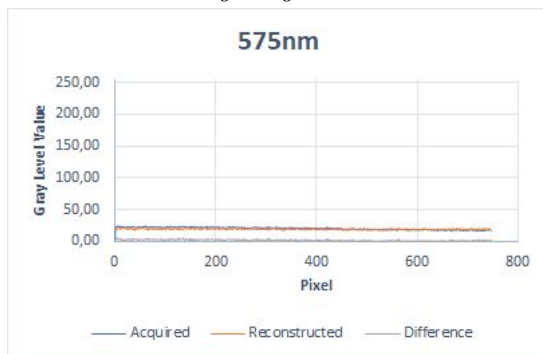
Figure 5.16: Reconstructed images from 5.11 acquired spectral images with spline interpolation.



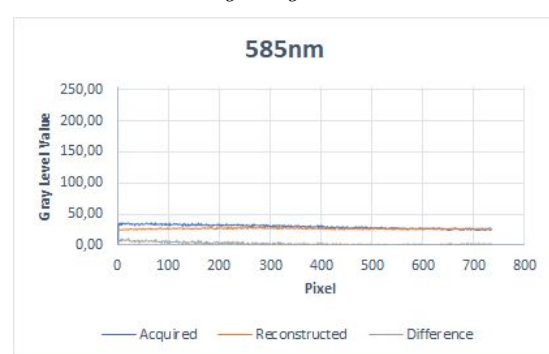
(a) Acquired image angle = -0.00196 ,
Reconstructed image angle = -0.00193



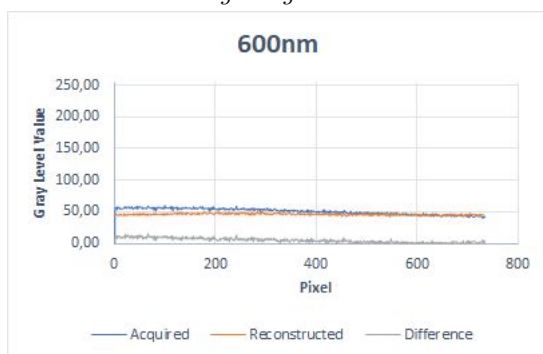
(b) Acquired image angle = -0.0051 ,
Reconstructed image angle = -0.0015



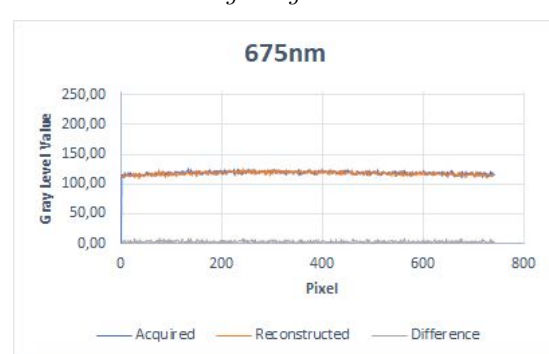
(c) Acquired image angle = -0.0083 ,
Reconstructed image angle = -0.0016



(d) Acquired image angle = -0.014 ,
Reconstructed image angle = -0.00009

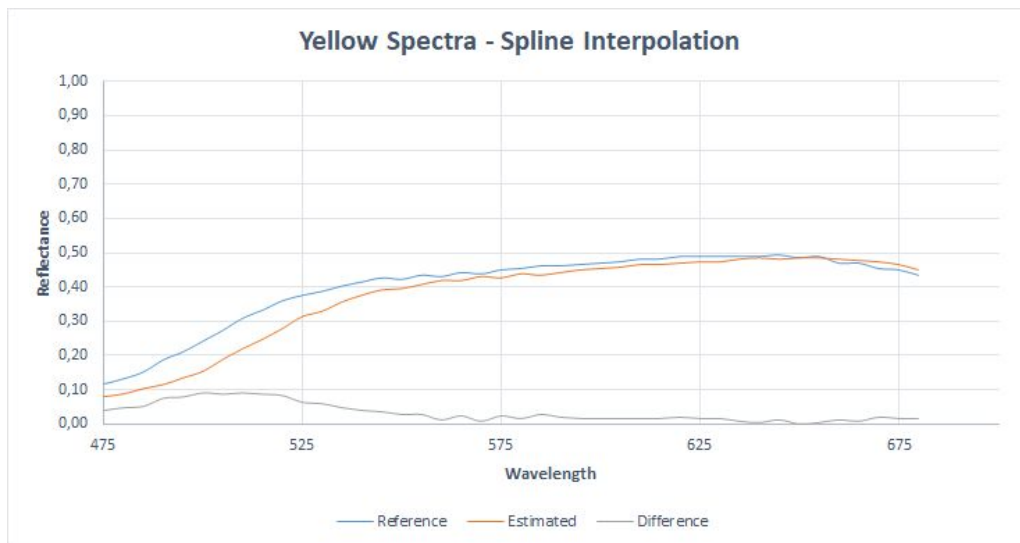


(e) Acquired image angle = -0.02 ,
Reconstructed image angle = -0.002

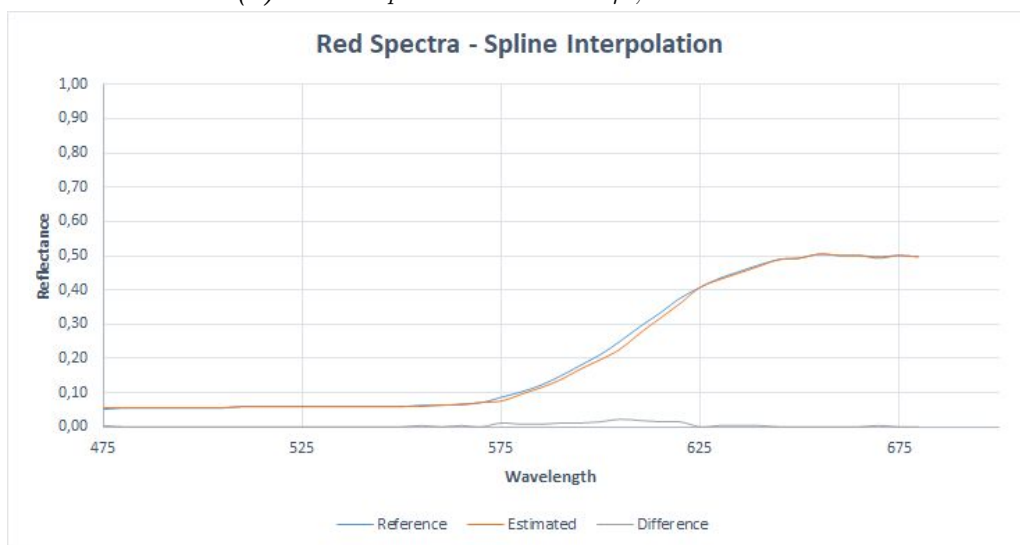


(f) Acquired image angle = -0.0009 ,
Reconstructed image angle = -0.00089

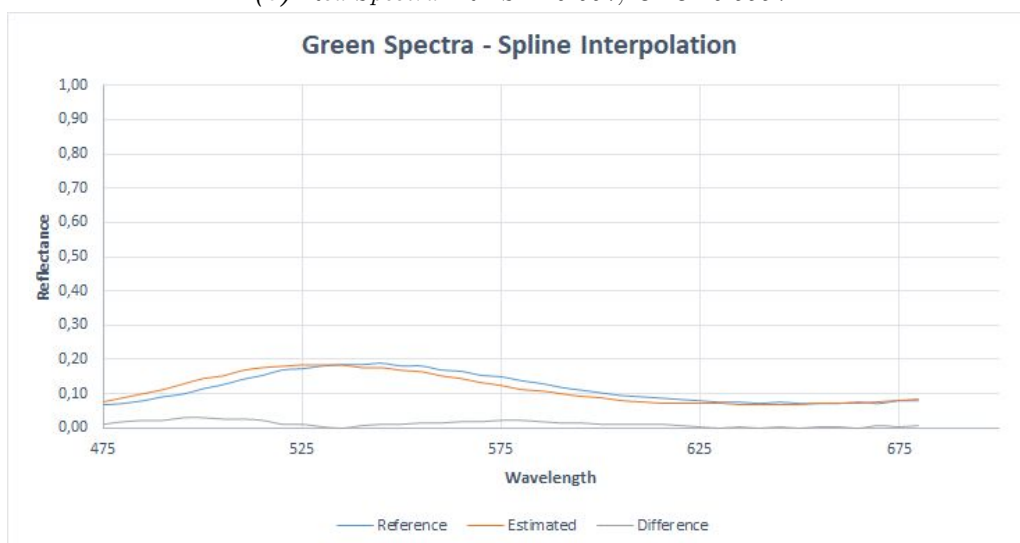
Figure 5.17: Spatial profiles of a row for the red patch target from 5.11 with spline interpolation.



(a) Yellow Spectra. $RMSE=0.043$, $GFC=0.9959$



(b) Red Spectra. $RMSE=0.007$, $GFC=0.9997$



(c) Green Spectra. $RMSE=0.016$, $GFC=0.9918$

Figure 5.18: Reference and estimated spectra from 5.11 with spline interpolation.

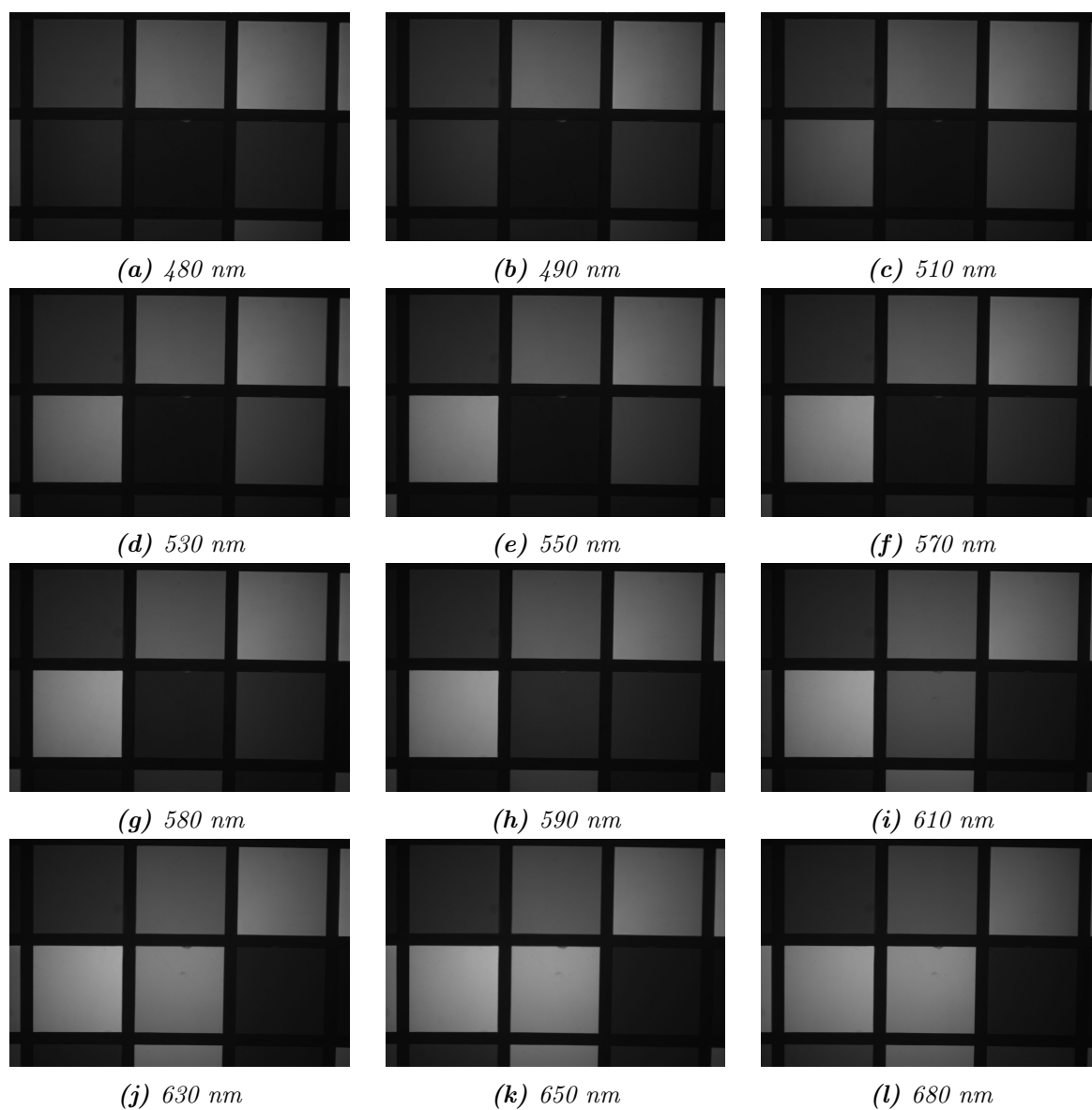
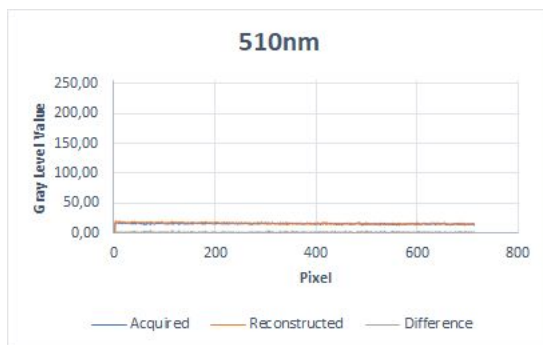
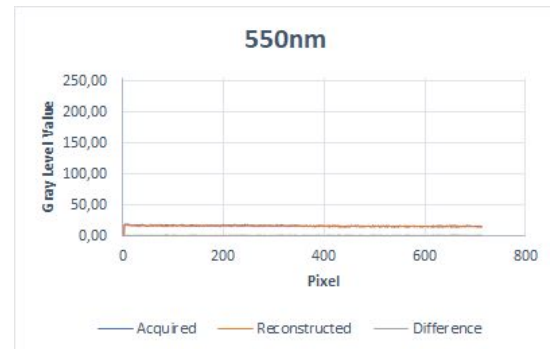


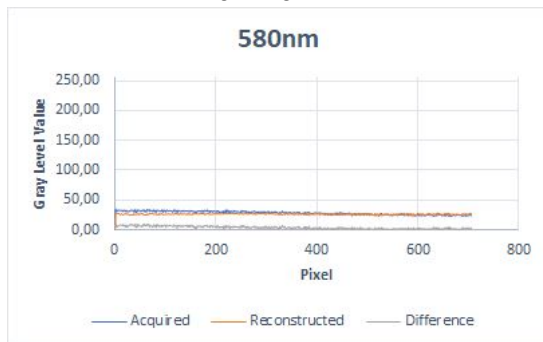
Figure 5.19: Reconstructed images from 5.12 acquired spectral images with linear interpolation.



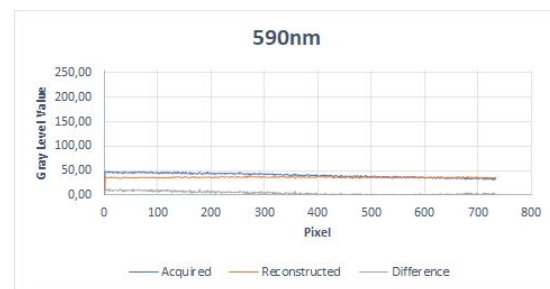
(a) Acquired image angle = -0.0027 ,
Reconstructed image angle = -0.0039



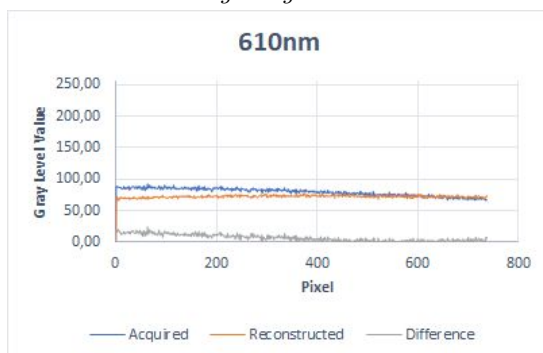
(b) Acquired image angle = -0.0029 ,
Reconstructed image angle = -0.0028



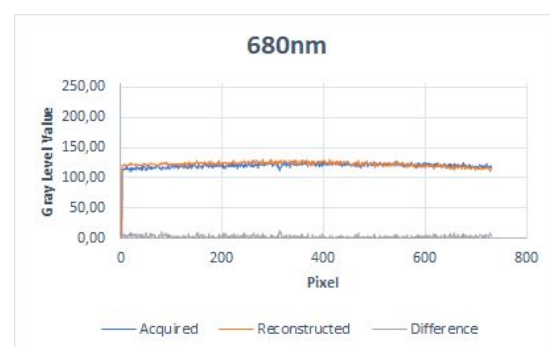
(c) Acquired image angle = -0.013 ,
Reconstructed image angle = -0.0009



(d) Acquired image angle = -0.02 ,
Reconstructed image angle = -0.0001

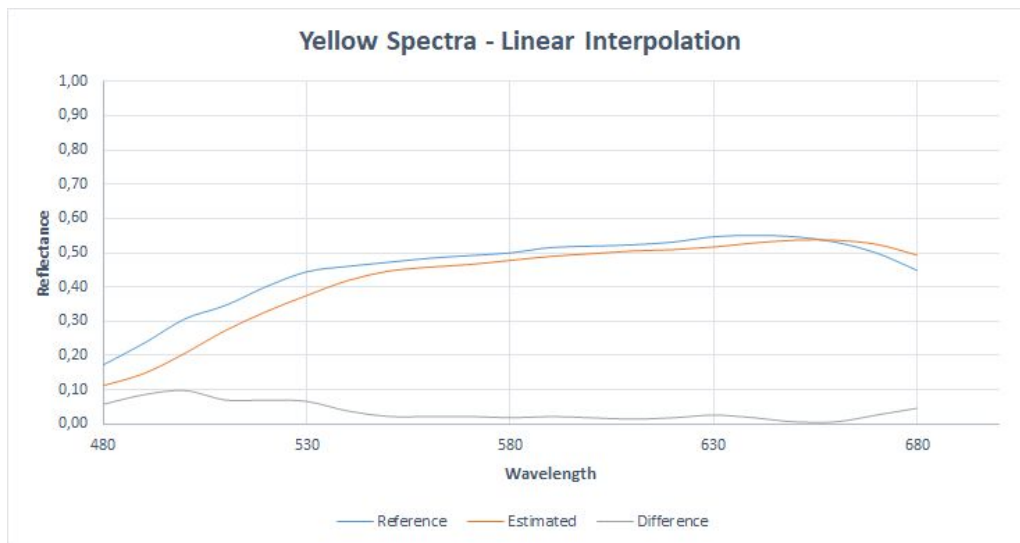


(e) Acquired image angle = -0.026 ,
Reconstructed image angle = -0.0019

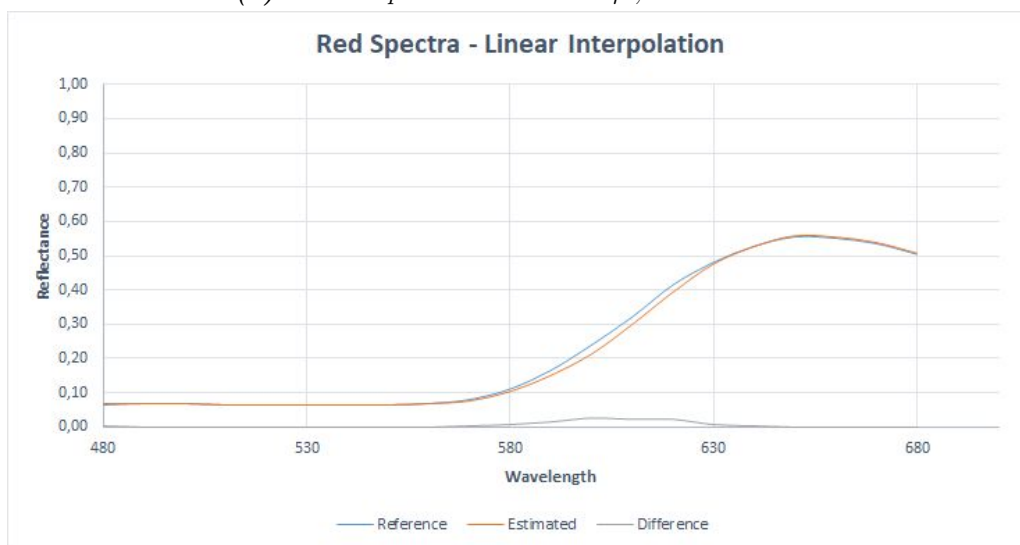


(f) Acquired image angle = -0.0052 ,
Reconstructed image angle = -0.0077

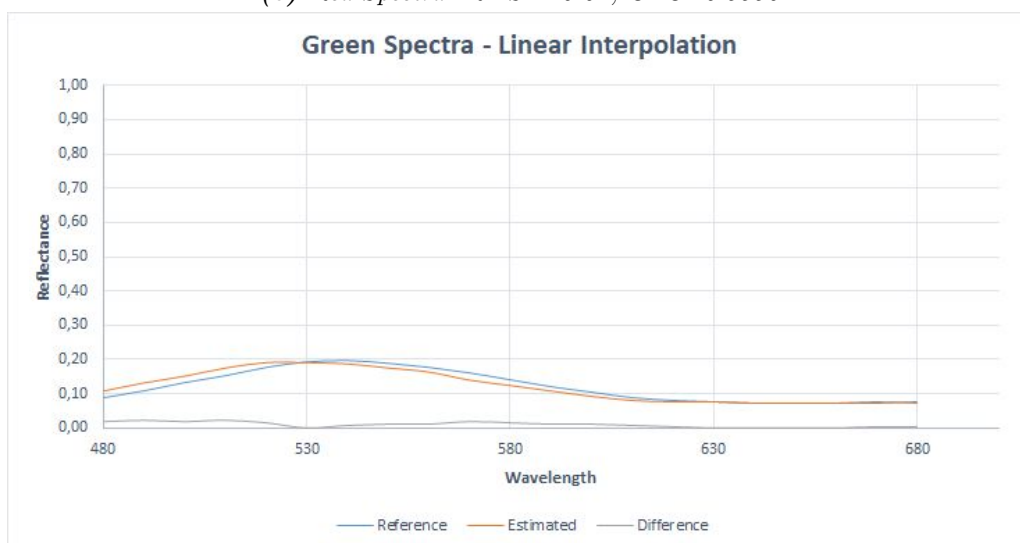
Figure 5.20: Spatial profiles of a row for the red patch target from 5.12 with linear interpolation.



(a) Yellow Spectra. $RMSE=0.046$, $GFC=0.9961$



(b) Red Spectra. $RMSE=0.01$, $GFC=0.9996$



(c) Green Spectra. $RMSE=0.013$, $GFC=0.9951$

Figure 5.21: Reference and estimated spectra from 5.12 with linear interpolation.

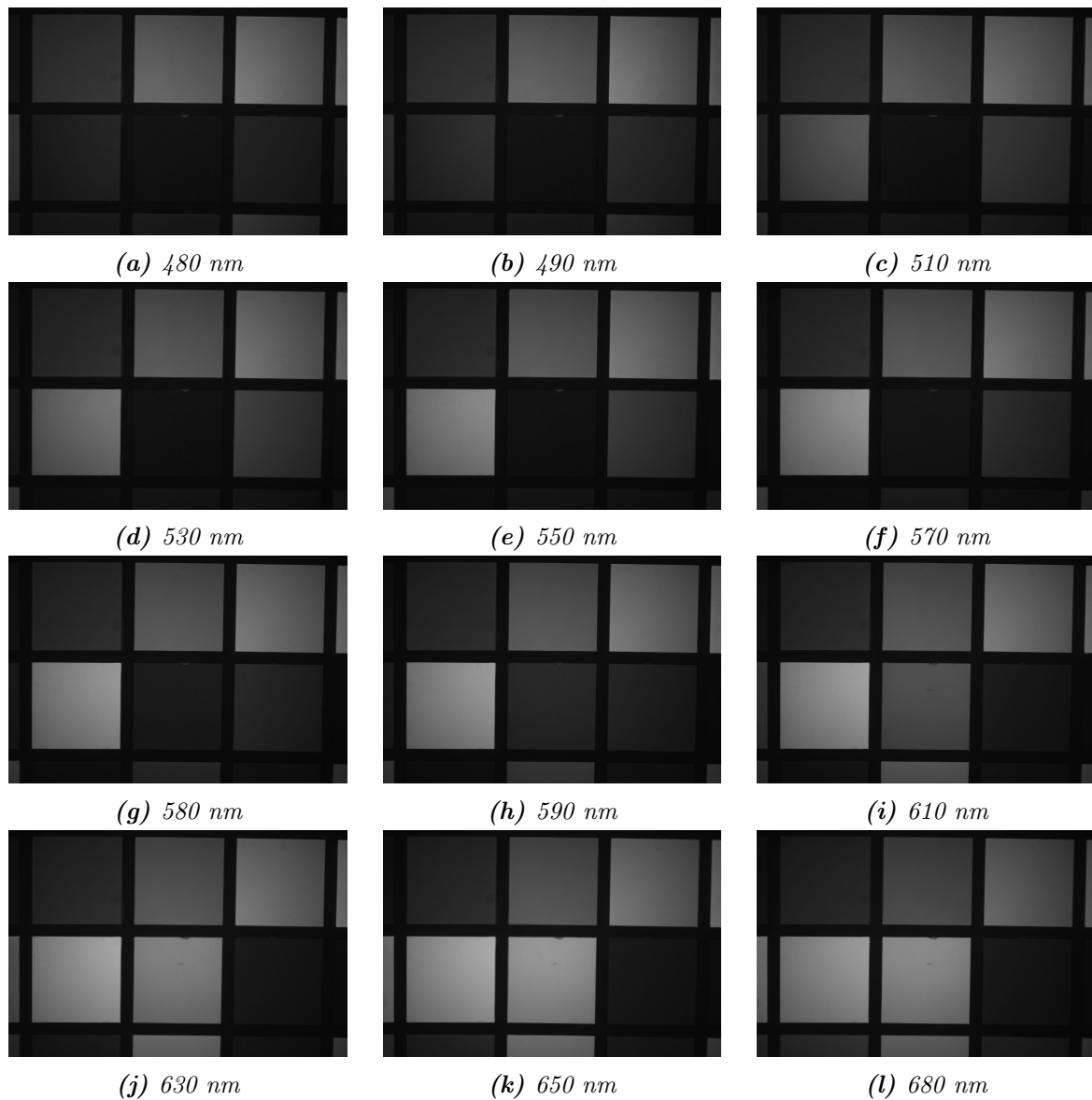
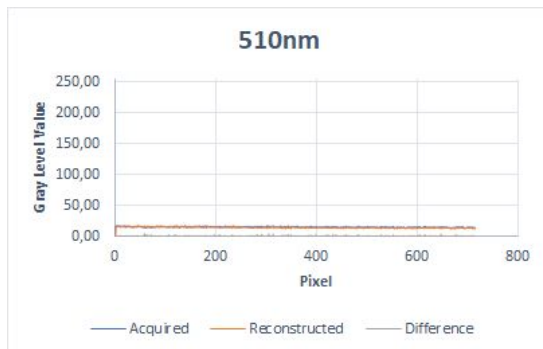
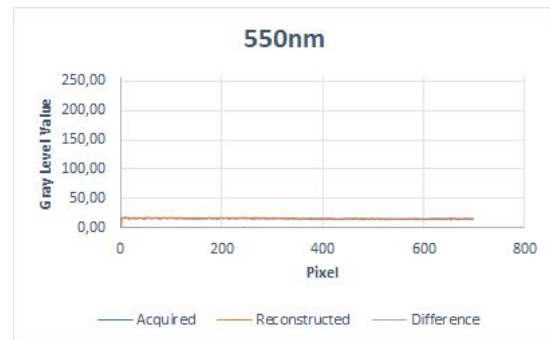


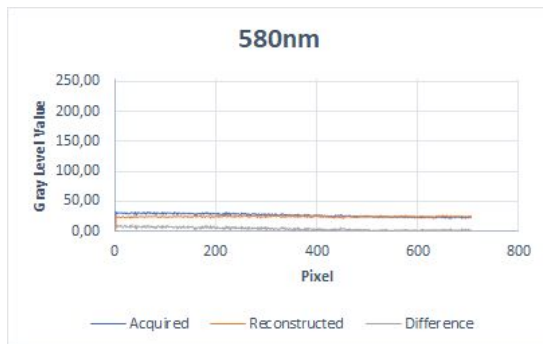
Figure 5.22: Reconstructed images from 5.12 acquired spectral images with spline interpolation.



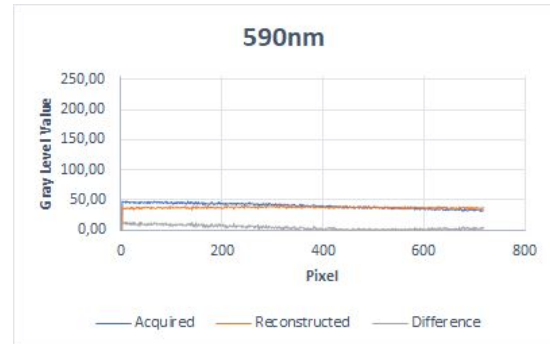
(a) Acquired image angle = -0.0027 ,
Reconstructed image angle = -0.0037



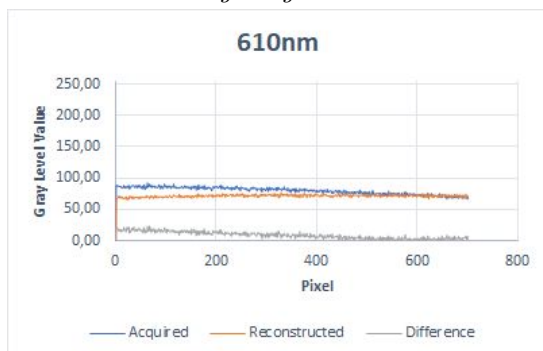
(b) Acquired image angle = -0.0029 ,
Reconstructed image angle = -0.0025



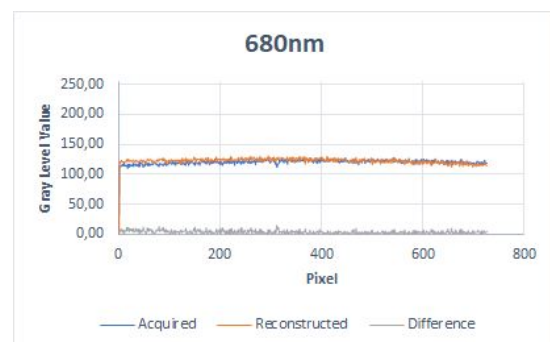
(c) Acquired image angle = -0.013 ,
Reconstructed image angle = -0.0005



(d) Acquired image angle = -0.02 ,
Reconstructed image angle = -0.0001

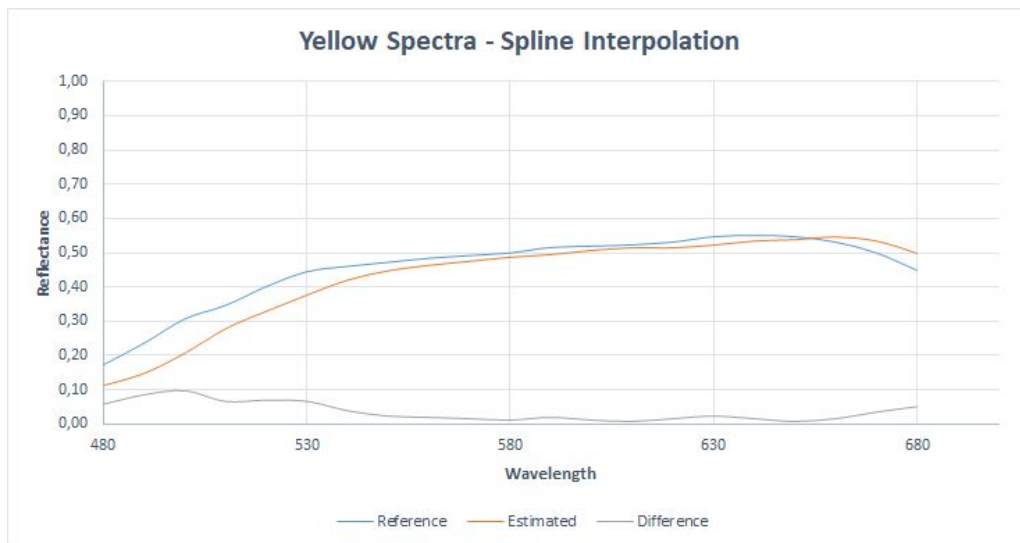


(e) Acquired image angle = -0.025 ,
Reconstructed image angle = -0.0033

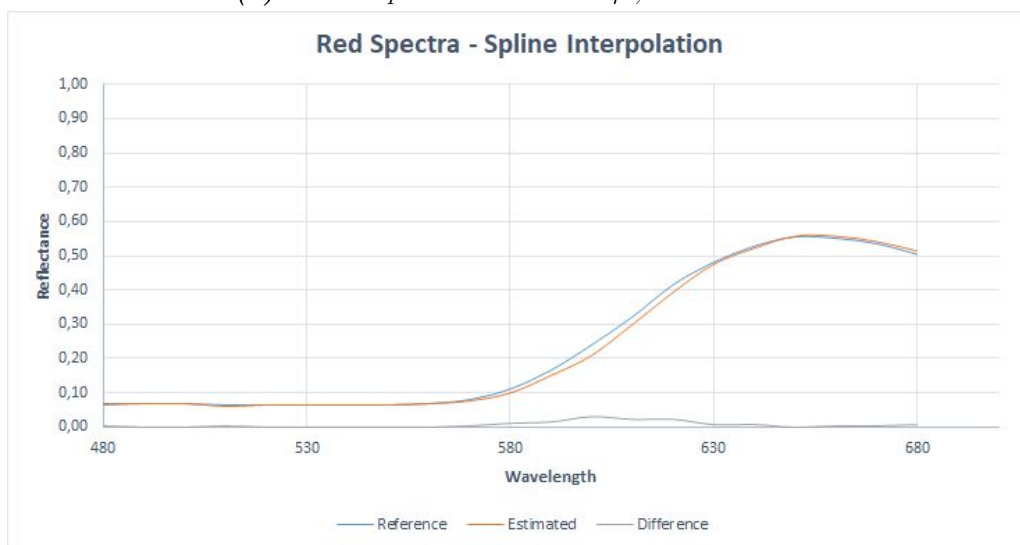


(f) Acquired image angle = -0.0054 ,
Reconstructed image angle = -0.0074

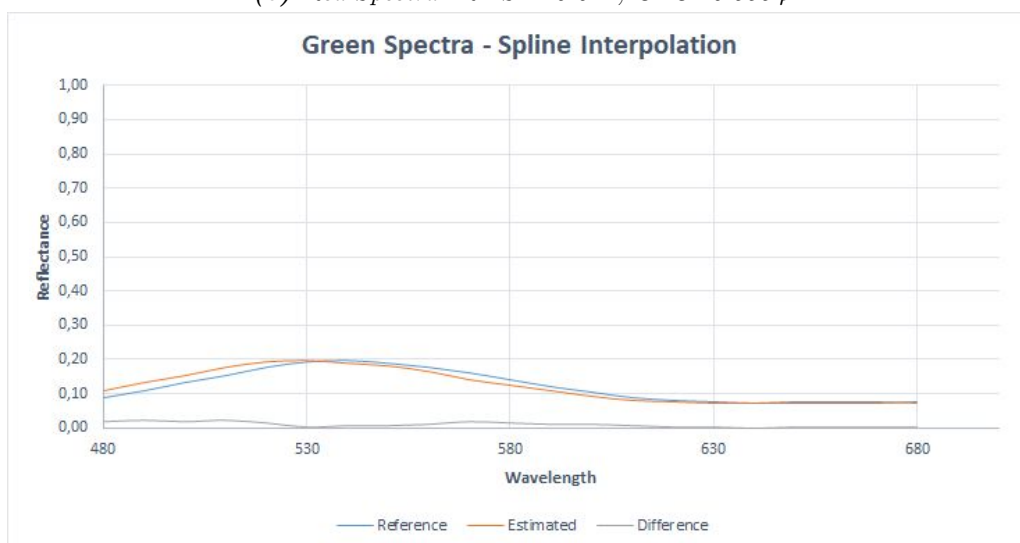
Figure 5.23: Spatial profiles of a row for the red patch target from 5.12 with spline interpolation.



(a) Yellow Spectra. $RMSE=0.045$, $GFC=0.9959$



(b) Red Spectra. $RMSE=0.011$, $GFC=0.9994$



(c) Green Spectra. $RMSE=0.013$, $GFC=0.9952$

Figure 5.24: Reference and estimated spectra from 5.12 with spline interpolation.

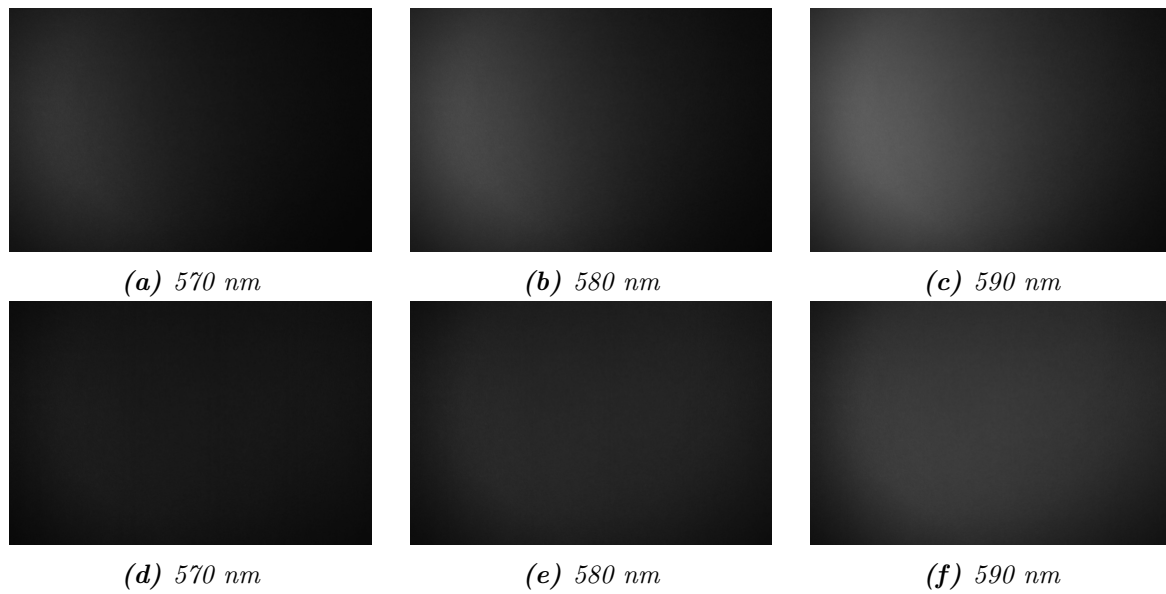


Figure 5.25: Acquired (a-c) & reconstructed (d-f) spectral images of the red patch target

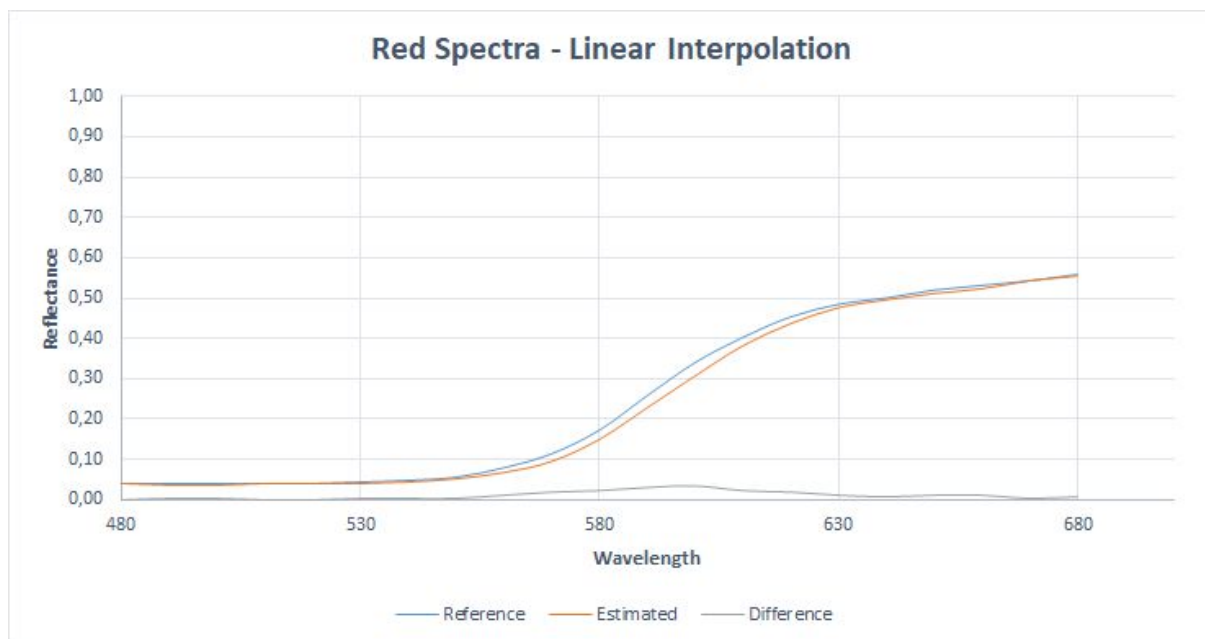
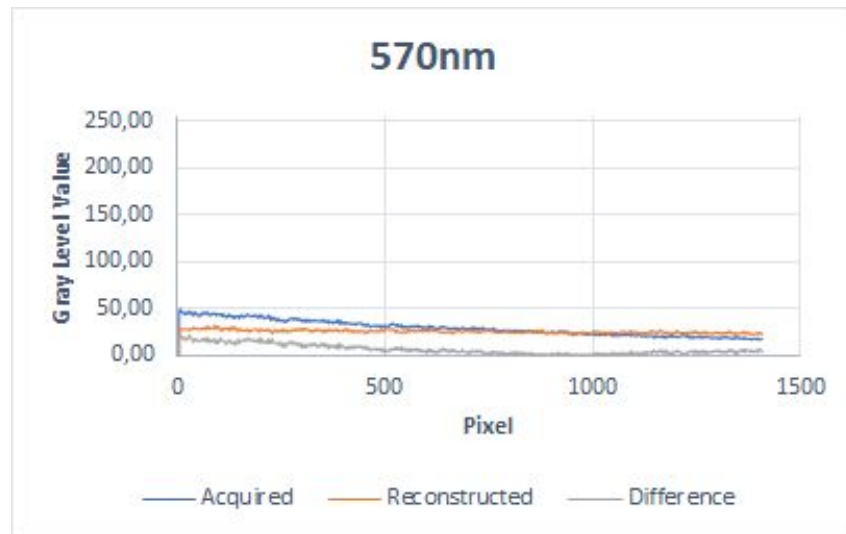
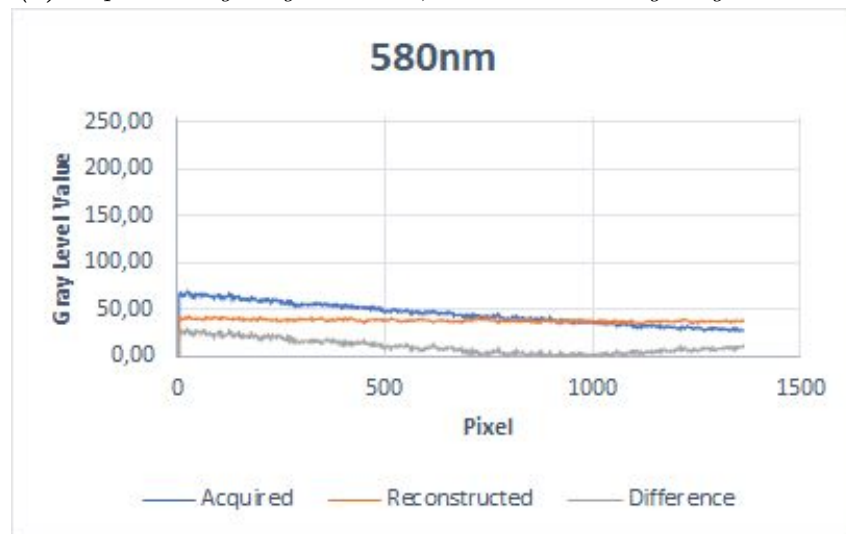


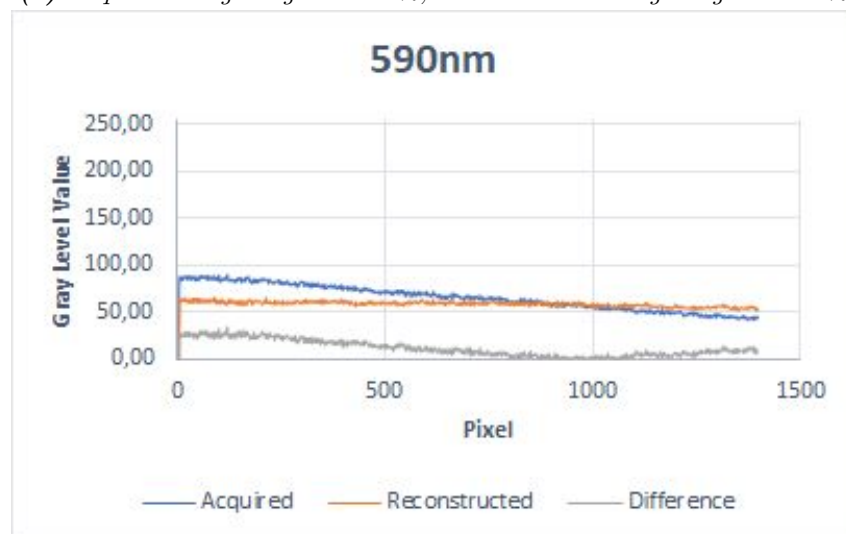
Figure 5.26: Reference vs. Estimated Spectra. $RMSE=0.015$, $GFC=0.9994$



(a) Acquired image angle = -2.0% , Reconstructed image angle = -0.3%



(b) Acquired image angle = -2.9% , Reconstructed image angle = -0.2%



(c) Acquired image angle = -3.3% , Reconstructed image angle = -0.5%

Figure 5.27: Spatial profiles of a row for the red patch target with linear interpolation

5.5 Results

It is expected that the patch targets would behave differently while the filter is scanning the target-image. This can be justified by the fact that yellow bands cause illumination of yellow patch, red bands of red patch, and green bands of green patch, respectively. Thus, illumination of a specific patch target is accompanied with a sense of darkness for the rest of the two others. The aforementioned alternation in illumination constitutes a good way to confirm the efficient function of the reconstruction algorithm at a first stage.

Judging by the above figures, the required alternation in illumination of patch targets achieved in both 5 nm and 10 nm tuning step. However, a problem derived, as far as the appearance and quality of the reconstructed images, using the tomographic reconstruction technique, are concerned. This refers to the observation of stripes across the reconstructed spectral images. Chances are that this malfunction regards to the improper separation of the spectral bands. Looking carefully at Fig. 5.5 and Fig. 5.8, we realize that smaller step is accompanied with improper separation of spectral bands. Being more specific, small step requires a large number of scanned images in order to form a reconstructed band and this fact allows the insertion of next bands of the variable filter that should be corresponded to other spectral images.

On the other hand, as we can see from the spectral metrics between the reference and estimated spectra, the reconstruction method based on image interpolation is almost excellent and we achieve very good results. But, looking carefully at the reconstructed images (using contrast enhancement), we can notice a kind of stripes in some spectral bands (565 – 595 nm) of the red patch target. In this spectral range, the spectral profile of the red patch target, as we can see from Fig. 5.18 for instance, exhibits a step increase of its reflectance. This step increment leads to the appearance of those stripes. With spline interpolation, this stripe effect tends to be eliminated thanks to the smooth behavior of cubic splines.

Furthermore, looking at Fig. 5.25.a-c there is a gradient in the gray level values over the acquired spectral images. This is due to the serial movement of the linearly variable filter, and that way each of the acquired spectral images consists of many spectral bands. After the reconstruction of the spectral cube, we have a new set of images, in which a single one wavelength is represented by each one of the new reconstructed images. So, looking at Fig. 5.25.d-f, the gray level values over the reconstructed images are flat. Fig. 5.27 demonstrates this difference between the acquired and reconstructed images.

5.6 Brief Summary

Fig. 5.28 provides a flowchart of all the procedures developed and presented in chapter 4 and 5. Each process is represented by a rounded-corner rectangle and constitutes a different phase of the total implementation.

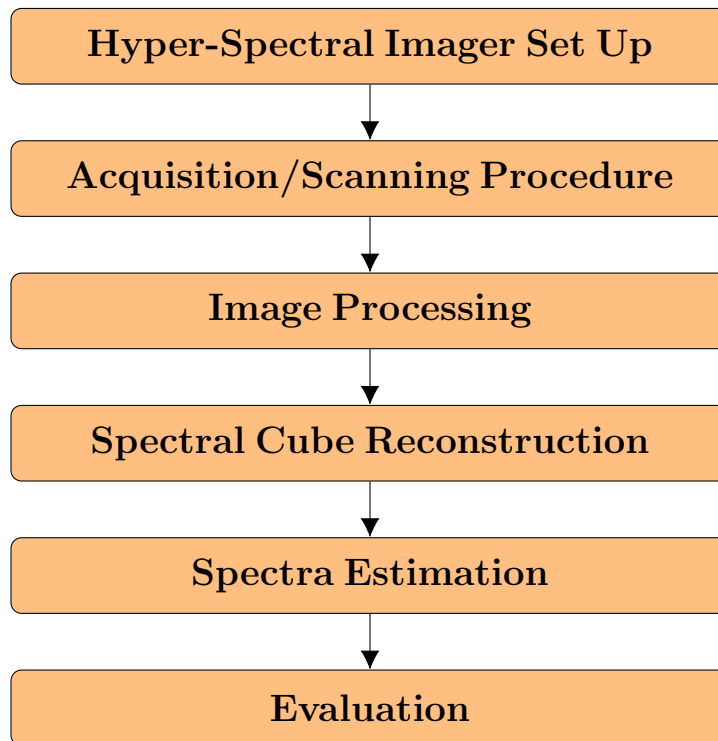


Figure 5.28: Flowchart of the HSI implementation

Chapter 6

Hyper-spectral Skin Imaging

6.1 Introduction

Visual observation has an important role in dermatology as the skin is the most visible organ. This makes dermatology a good candidate for utilizing digital imaging and automatic diagnostic tools. Hyper-spectral imaging is now one of the most developed methods of visible light imaging. It enables to acquire data of an object in any spectral range set in the camera. This method is entirely non-contact and non-invasive, and measurements can be carried out remotely. With these advantages, hyper-spectral cameras are used in many fields of technology and medicine. In particular, they are used in dermatology. The issue of dermatological research concerns spectral skin analysis in almost all cases.

The surface of the body is an excellent area for deployment of optical research methods, and HSI technology is being applied in ever more applications in dermatology for non-invasively targeting cancer detection, skin oxygenation mapping for diabetic ulcers, spectral unmixing of fluorescently labeled antigens, and more.

6.2 Tissue Optics Principles

The human skin presents a complex heterogeneous medium, where the blood and pigment content are spatially distributed variably in depth. The human skin is named *cutis*, and is composed of two layers; a top layer called *epidermis* and a bottom layer called *dermis*. Below dermis, there is a subcutaneous fat layer.

Information about skin physiology, morphology, and composition can be obtained non-invasively by optical imaging methods. When light interacts with tissue, it is usually altered in some way before being remitted and detected by an image sensor. Photons can be scattered because of

the refractive index fluctuations on a microscopic level by collagen fibers or by membranes, have their polarization altered after multiple scattering events, or be absorbed by molecules such as hemoglobin or melanin.

The epidermis varies in thickness from 0.3 mm to 1.5 mm, and consists of a multilayer plate epithel. Almost all of the cells in epidermis, around 90%, are keratinocytes. The epidermis is further divided into layers called strata. These layers are the basale layer, the spinous layer, the granular layer and the corneum layer, as seen in Fig. 6.1. Melanin is found in the epidermis in the form of red/yellow pheomelanin and/or brown/black eumelanin that absorbs very broadly in the visible spectrum with higher values for shorter wavelengths.

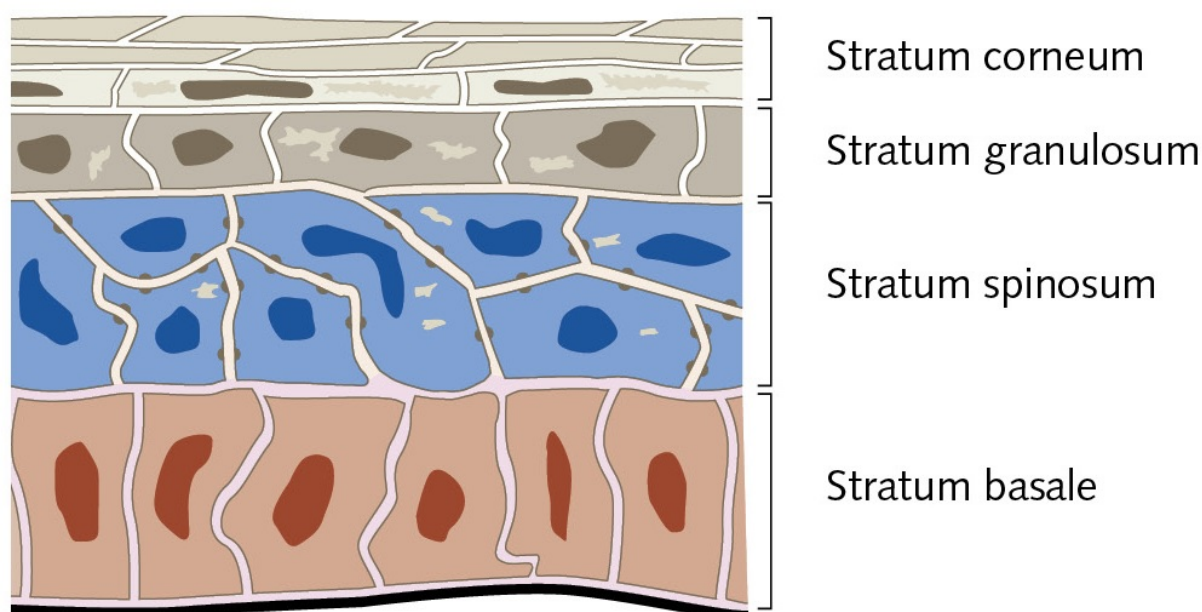


Figure 6.1: *The composition of epidermis*

The dermis, which is located below the epidermis, varies in thickness from 1.4 mm to 4 mm. Dermis consists of collagen and elastic fibers, and is divided into two layers, where the lower is called the reticular dermis and the upper is called the papillary dermis. An illustration of the composition of dermis can be seen in Fig. 6.2. The layers are composed of connective tissues, blood vessels, and nerves. In the blood cells there are several natural chromophores, primarily hemoglobin, which absorbs blue and green light and gives blood its reddish color. Other chromophores present can include bilirubin and β -carotene that when found in the dermis contribute to the yellowish or olive tint of human skin.

Fig. 6.3 displays the absorption spectra of major skin constituents that have a distinctive spectral absorption signature.

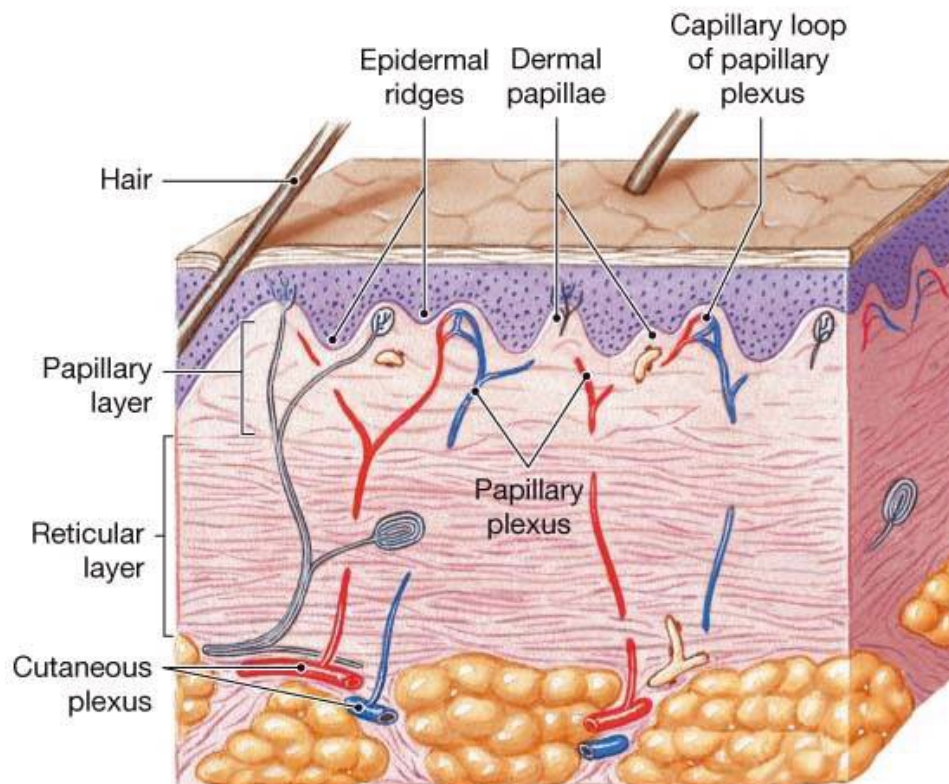


Figure 6.2: The composition of dermis

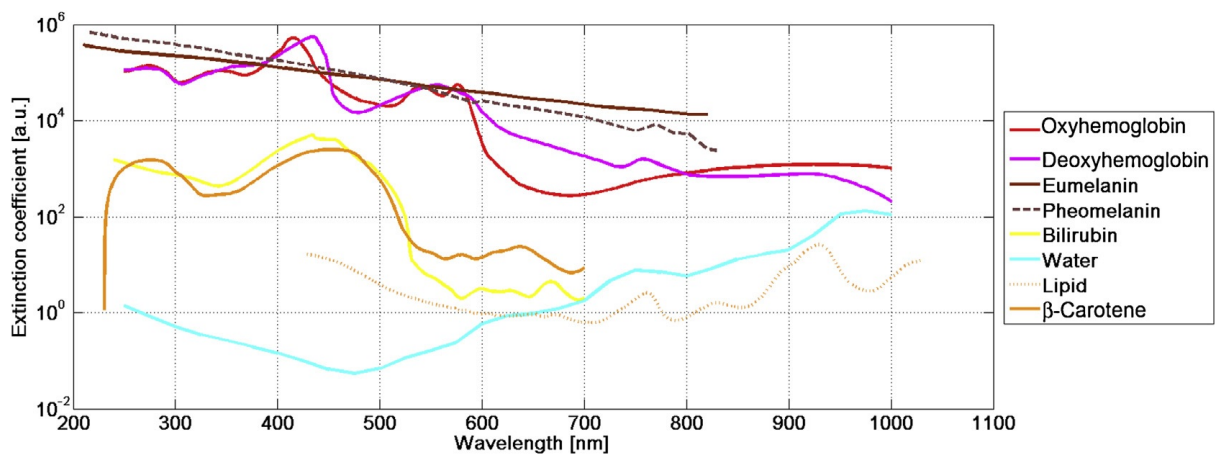


Figure 6.3: Absorption spectra of skin constituents

Light entering tissues can also have its wavelength distribution shifted by interaction at the atomic or molecular levels, producing fluorescence or Raman signals. Interpreting these changes can provide diagnostically useful information about the underlying structure of the tissue, provided that there is a plausible biological rationale for the change. Changes in the spectral

characteristics in different wavelength regions produce a distinguishable spectral signature that reflects the underlying biology.

Spectral imaging technology has a unique capability for skin characterization because it can take advantage of the spatial relationships among the different tissue absorption spectra in a neighborhood. Spectral data cube analysis can incorporate complex spectral-spatial models that can provide more accurate classification of image features specific to a targeted disease. The technology unlocks new capabilities in medicine by which spatial and functional relationships among biologically active molecules can be observed, helping to non-invasively identify and quantify changes in living organisms, and enhancing histopathological and fluorescent biomarker image analyses to improve biological knowledge of diseases.

The penetration depth of light into biological tissues depends on how strongly the tissue absorbs and scatters light. High melanin concentration at the topmost layer of skin (epidermis) absorbs light in the ultraviolet (UV) and visible range, leading to low penetration depth for wavelengths shorter than 600 nm. In the wavelength range from 600 to 1300 nm, skin has sufficiently weak absorbers to permit significant light penetration. Because of this characteristic, this wavelength range is often called the *therapeutic window*. Fig. 6.4 shows a schematic of light penetration depth at different wavelengths for human skin.

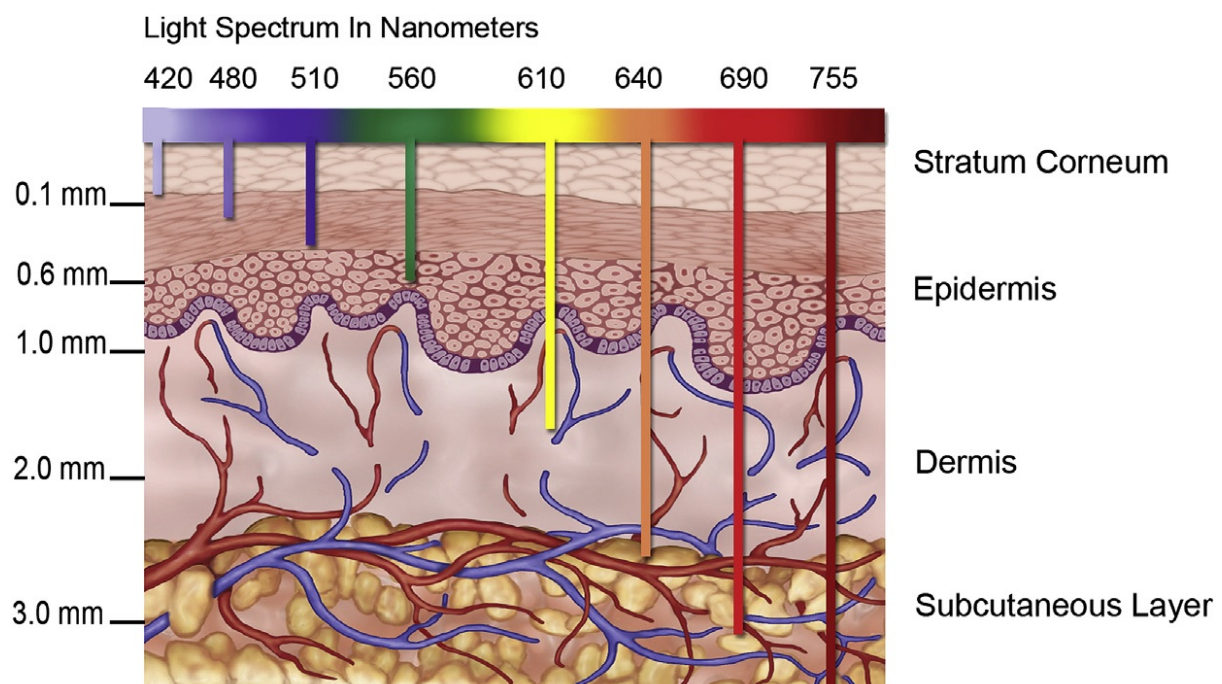


Figure 6.4: The penetration of light of different wavelengths in the skin

6.3 Spectral Imaging for Skin Assessment

Biomedical optics is one of the fastest growing areas of research. Biomedical imaging has become a powerful tool for diagnostics and monitoring of human health condition. The non-ionizing nature of light applied for investigation and detection of abnormalities in human tissue make this area very attractive for development of new diagnostic techniques and modalities. The optical spectra provide biochemical and morphological information about the tissue under investigation based on its absorption, reflectance, fluorescence and elastic scattering properties.

In recent years, optical spectroscopies have become the basis for a high level of research activity directed toward the development of novel, non-invasive technologies for tissue diagnostics, frequently dubbed “optical biopsy”, which is perhaps something of an oxymoron, since “biopsy” refers specifically to the removal of tissue, whereas the implication of “optical” is that tissue is not removed. The motivation is to eliminate the need for surgical removal of biopsy tissue samples; rather, some form of spectral analysis of the tissue is recorded **in vivo** by an imaging system placed on or near the surface of the tissue in question. A diagnosis of the tissue is then attempted based on the optical measurements. The intent of these systems is to provide diagnostic signatures, **in situ**, non-invasively and in real-time. The different skin components (such as melanin, hemoglobin, oxy-hemoglobin and water) behave differently in the infrared part of the electromagnetic spectrum. However, the human eye is not sensitive to this spectral range. Hyper-spectral images acquired in the visible to near-infrared spectrum may help experts to differentiate benign from malignant lesions.

6.3.1 Cutaneous Melanoma

Cutaneous melanoma currently represents 5% of newly diagnosed cancers in men and 6% in women; it is the leading fatal illness affecting the skin and is responsible for 80% of deaths from skin cancer. It is hard to distinguish visually melanomas from non-malignant nevi. Early signs of melanoma appearance include changes in the shape or in the color of existing moles or in the formation of a new lump. The **ABCDE** rule (**A**, Assymetry, **B**, Border irregularity, **C**, Color variation, **D**, Diameter, and **E**, Evolving) helps in lesion diagnosis. By now, biopsy sampling from melanoma (which may increase the risk of spreading metastases) is the main method for making a precise diagnosis of the malformation. More patient-friendly non-invasive primary diagnostics would be preferable.

Hyper-spectral imaging is a non-contact optical technique with a promising potential for in vivo skin diagnostics. Using narrow-band filtering at different wavelengths, a set of spectral images of the same skin location is taken. Each pixel of the image contains information about the corresponding skin spot at a specific wavelength, and a diffuse reflection spectrum for every pixel

can be obtained by processing the set of hyper-spectral images. Usually, hyper-spectral images are acquired in a visible and infrared wavelength region (e.g. 400 – 1000 nm). The penetration depth of optical radiation in the skin tissues depends on wavelength, so diffuse reflectance from skin at broadband illumination may provide morphological information from different depths, and hyper-spectral imaging analysis makes it possible to extract this information. Advanced image processing allows mapping the main skin absorbing chromophores — oxy-hemoglobin, deoxy-hemoglobin, and melanin.

6.3.2 Melanoma Biology

Cutaneous melanoma is a malignant skin tumor of melanocytic origin, characterized by its high invasiveness and metastasis. In normal skin, melanocytes dwell in the basal layer of the epidermis and generally do not proliferate. Each melanocyte establishes contact with approximately 20 – 35 keratinocytes through its dendrites. Basal layer keratinocytes regulate melanocyte growth, morphology, proliferation, and expression of membrane-associated antigens through direct cell-cell contact. A nevus is formed by the aggregation of benign melanocytic cells. Melanoma is thought to develop and progress in a sequence of five steps:

1. **Benign melanocytic nevi:** controlled proliferation of normal melanocytes to produce a benign nevus
2. **Dysplastic nevi:** abnormal growth of melanocytes in a pre-existing nevus or new location resulting in a pre-malignant lesion with random cytologic atypia
3. **Radial growth phase (RGP) primary melanoma:** melanocytes acquire ability to proliferate horizontally in the epidermis and histologically show continuous atypia (melanoma **in situ**). E-cadherin¹ helps confine the cells intraepidermally but a few cells may invade the papillary dermis.
4. **Vertical growth phase (VGP) primary melanoma:** numerous biochemical events including the loss of E-cadherin and expression of N-cadherin allow malignant cells to invade basement membrane and proliferate vertically in the dermis as an expanding nodule with metastatic potential.
5. **Metastatic melanoma:** malignant melanocytes spread to other areas of body, usually first to lymph nodes then to skin, subcutaneous soft tissue, lungs and the brain.

However, melanoma may skip steps in its development. The typical stages of melanoma progression are shown in Fig. 6.5.

¹**Cadherins**, which are cell surface glycoproteins mediating cell-cell adhesion, play an important role in skin homeostasis and melanoma development. The cadherins have isotopes of E-, P-, and N-cadherin.

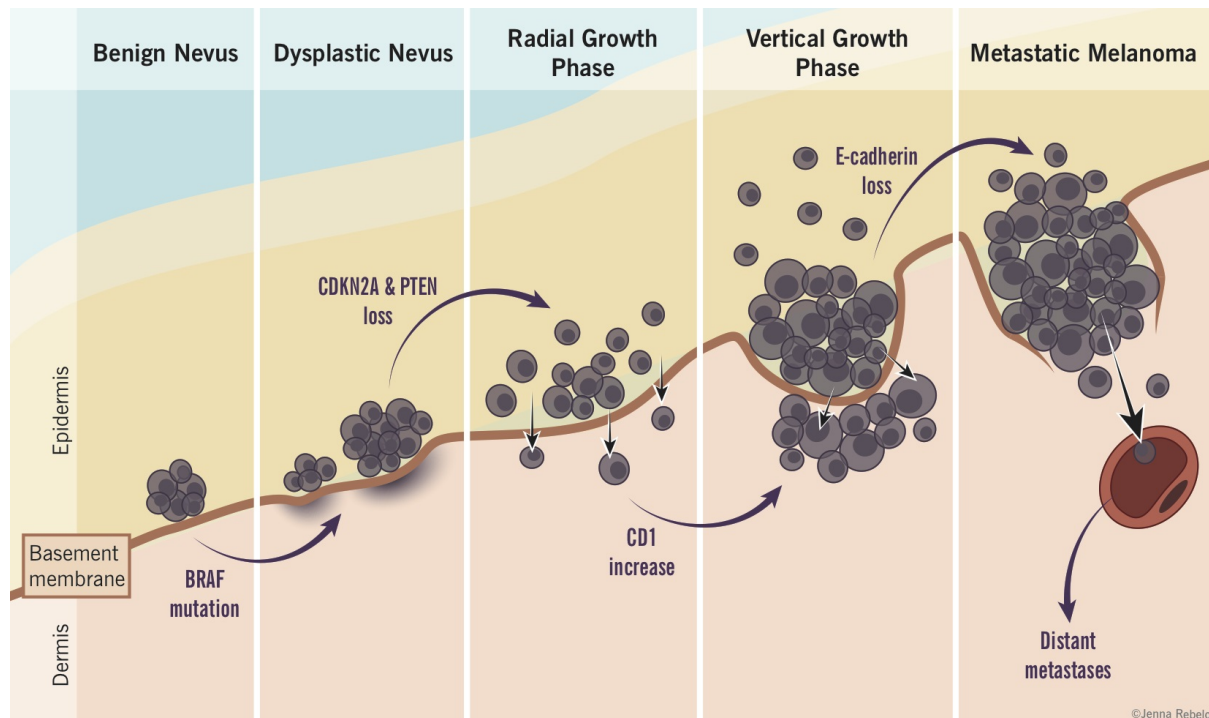


Figure 6.5: The stages of melanoma development

6.4 Experimental Procedure

The experimental tests carried out by the HSI system we presented in chapter 4. By using the aforementioned HSI system, we acquired a spectral cube of human (benign) nevi. The wavelength range of the scanning procedure is 450 – 1000 nm, with 10 nm tuning step. Consequently, we used the reconstruction techniques, described in chapter 5, to reconstruct the nevi spectral cube. Acquired and reconstructed spectral images are following, as well as estimated and reference spectra.

6.4.1 Acquired Spectral Cube Images

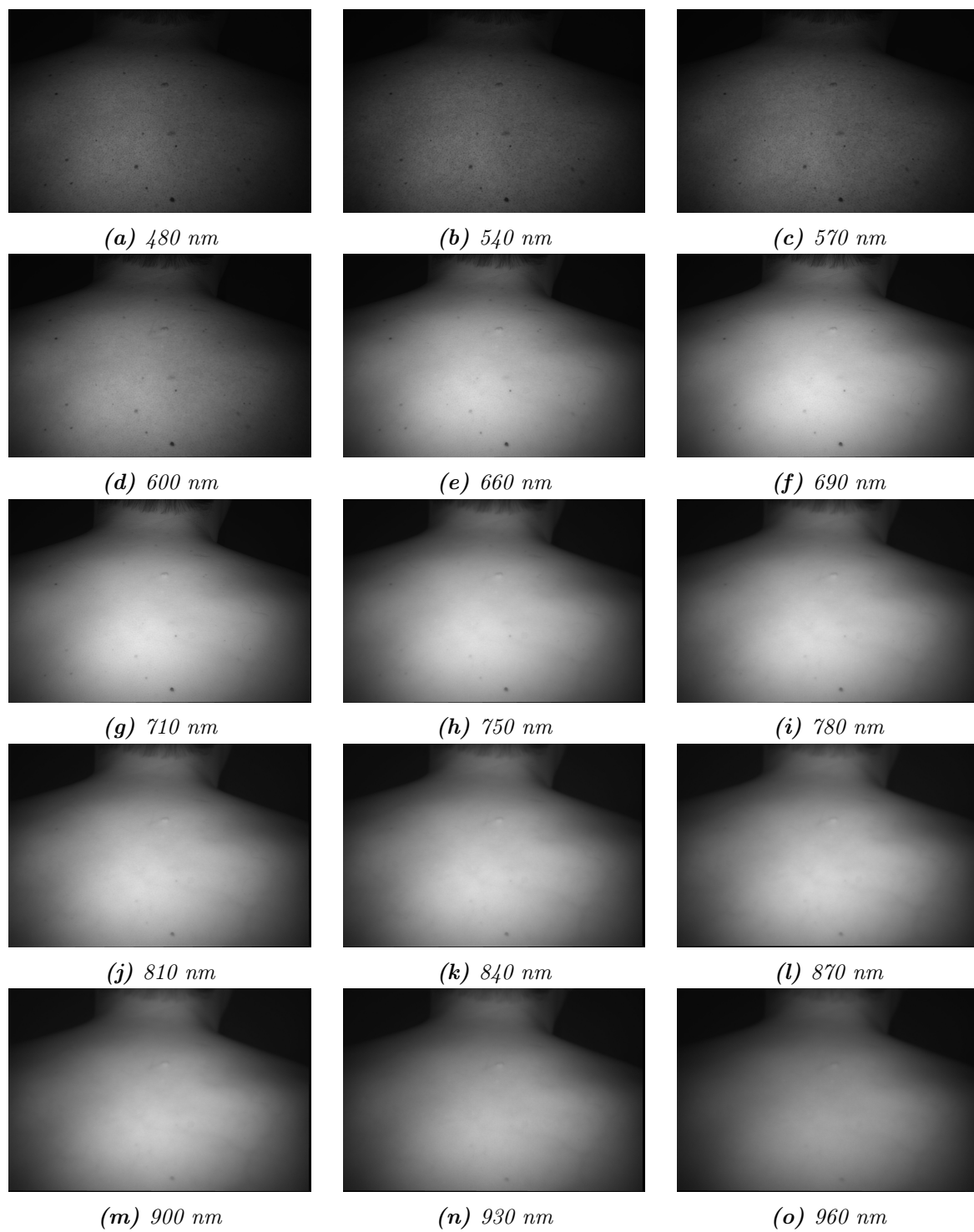


Figure 6.6: Acquired spectral images \rightarrow 10 nm tuning step.

6.4.2 Reconstructed Spectral Cube Images

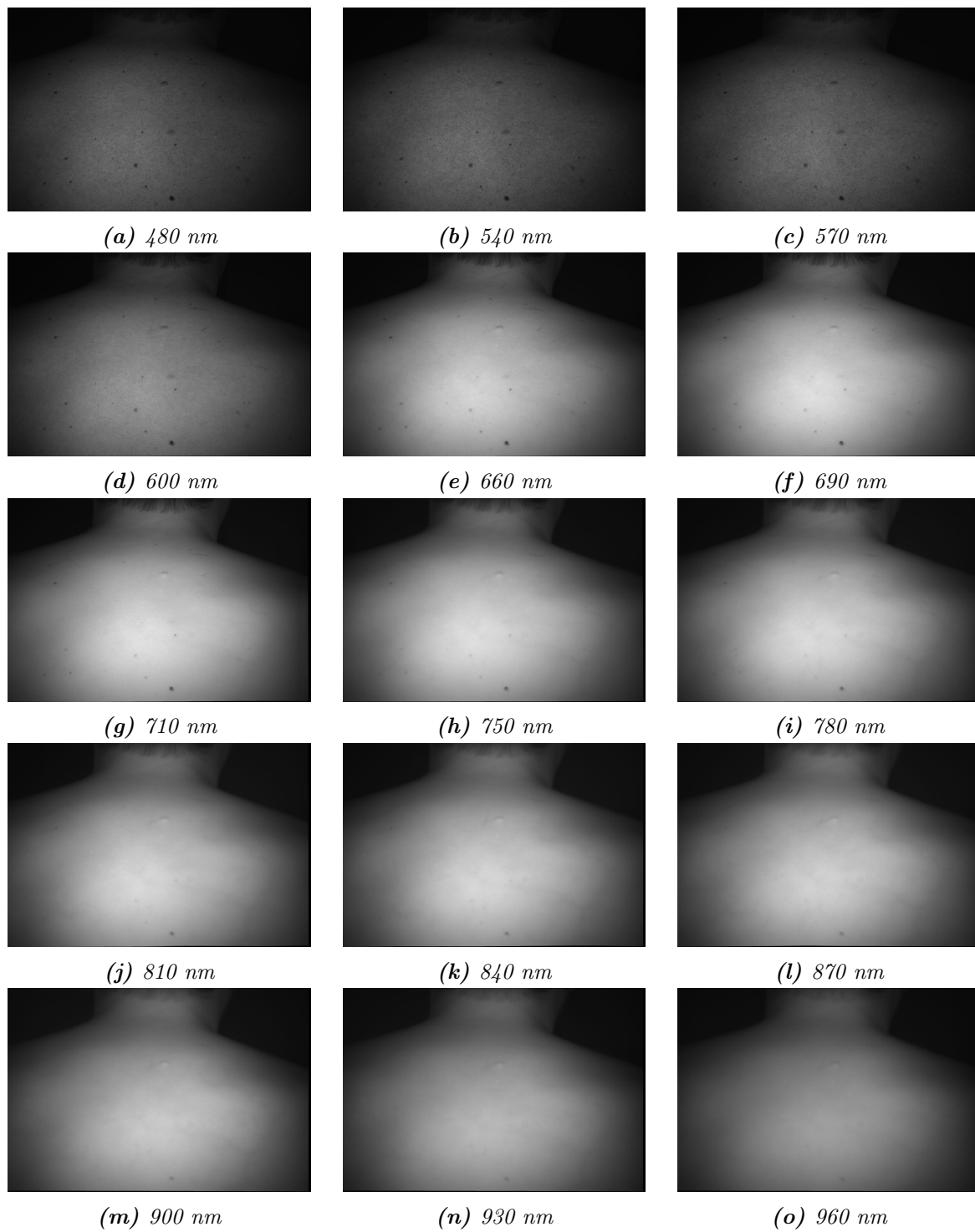
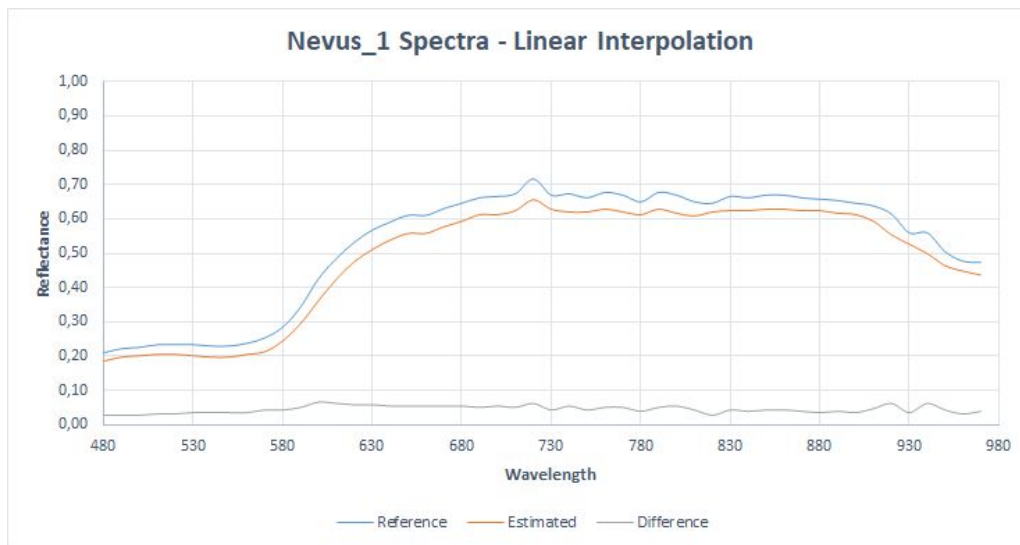
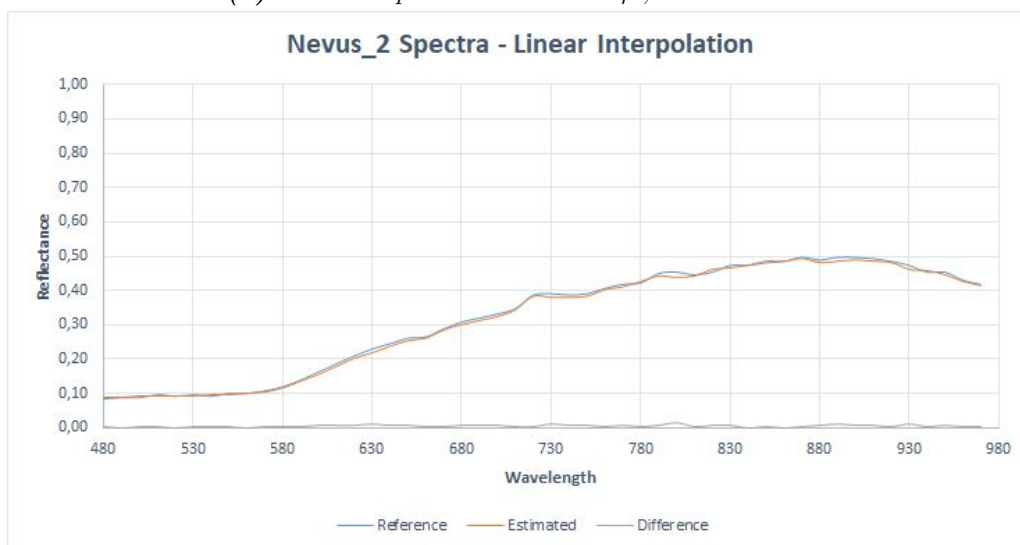


Figure 6.7: Reconstructed images from 6.6 acquired spectral images with linear interpolation.



(a) *Nevus 1 Spectra. RMSE=0.047, GFC=0.9997*



(b) *Nevus 2 Spectra. RMSE=0.007, GFC=0.9999*

Figure 6.8: Reference and estimated spectra from 6.6 with linear interpolation.

6.5 Results

The great advantage offered by spectral imaging is that the recording of lesions in different spectral regions allows observation of the lesion even in skin layers that can not be seen with the naked eye. In particular, the greatest diagnostic information provided by the near infrared region of the electromagnetic spectrum, as at this spectral region features of the lesions found in deeper skin layers can be estimated. This is particularly important, as melanin is found in different layers of the human skin and the presence or absence of melanin in skin layers is in many cases a factor of differentiation between lesions.

The accessibility of the skin to simple visual inspection and the relative ease of skin biopsy have retarded the adoption of high-tech diagnostic aids by dermatology relative to other specialties. These same attributes of visually distinct lesions and easy accessibility make the skin an excellent target for a myriad of non-invasive diagnostic technologies. The imperative to decrease melanoma deaths through early detection has prompted varied technologic approaches to improve diagnostic sensitivity while avoiding unnecessary excisions. Of the numerous evolving technologies, the optical-based approaches hold the greatest promise in the near-term. Eventually, it can be anticipated that multimodal imaging systems will significantly improve the accuracy of dermatologic diagnosis. Also, the spectral information acquired from HSI systems can serve as the basis for building spectral signatures for histological stages of melanoma development. In this way, spectral imaging may become an invaluable tool in the clinical setting for automated detection of early-stage melanoma.

Chapter 7

Conclusion and Future Work

The major advantage of hyper-spectral imaging is that an entire spectrum of information is acquired at every pixel of the object being examined. It is a non-destructive and non-invasive method, and hence could be used for on-line quality inspection and monitoring. The main advantage of hyper-spectral imaging is that it is possible to visualize the various biochemical components present in a sample based on spectral signature in a region of specific chemical composition where spectral properties may be similar.

Hyper-spectral imaging is complex because of the huge amount of data gathered, and it requires large storage capacity and fast computers to process and analyze the huge amount of data acquired. A major drawback in hyper-spectral imaging is the information overlap in adjacent slices, which makes the process of information extraction very challenging. The hyper-spectral imaging requires a relatively long time for image acquisition and processing, which makes it difficult to be implemented in real-time on-line applications.

Although the potential of hyper-spectral imaging seems unlimited, there are certain limitations, such as high cost of the equipment, the large quantity of data acquisition, and complicated data processing, has resulted in dragging the technology away from the actual installation in real-time applications in the commercial world. If the technical difficulties are overcome by very high-speed computers and readily available algorithms for spectral data processing, the usage of hyper-spectral imaging will become the most exploited and common technology in the near future.

In this thesis, we have studied the HSI system based on linearly variable filter theoretically and experimentally, and discussed different methods for reconstructing hyper-spectral images. The idea to successfully reconstruct the spectral cube in hyper-spectral imaging is central in this thesis. We developed a reconstruction technique based on image interpolation that is performing very satisfactorily at this moment when is being applied to real data. This approach leads to

a reconstruction method that obtains very good results. This method appears suitable for any kind of hyper-spectral camera and is not designed for a specific camera. The HSI system that has been presented so far is fully equipped with the functions of hyper-spectral scanning and reconstruction of spectral cubes. The image reconstruction relies heavily on good calibration. Calibration and configuration settings consist fundamental parts of this imaging system, which could find prospective application on medicine, agriculture, surveillance, mineralogy, astronomy and environment. The principal conclusion is that this type of imaging system is able to provide functional hyper-spectral and single-spectral images across the electromagnetic spectrum divided into many more close bands, beyond the scope of human eye. The spectral response of the depicted visual material/sample conveys useful information as far as its composition and behavior are concerned in multidimensional spaces, which is strictly associated with non-invasive and non-destructive analysis.

The image reconstruction should be as fast as possible. Despite the fact that the HSI system is provided with live display of the hyper-spectral scanning procedure, the image reconstruction procedure is not real-time. It requires the completion of the hyper-spectral scanning process first. Hyper-spectral images, although providing abundant information of the object, also bring high computational burden to data processing. Curse of dimensionality is a fact for these structures of data. The fact that the development of an accurate spectral cube reconstruction method is completed within the requirements of this thesis, does not indicate that there is not any potential of further improvement and perfection. For further work on the HSI system and the reconstruction technique, it is recommended to investigate the possibility of applying parallel computing to the image reconstruction in order to cut down on processing time. Furthermore, to evaluate the difference between the reference/observed spectrum and the estimated spectrum more complicated measures than Euclidean Distance could be used, such as Goodness-of-Fit Coefficient (GFC) [36]. Last but not least, an intrusion to the hardware of the HSI system could be done. Being more specific, attempts to reduce the distance between the linearly variable filter and the image sensor could be conducted. In this way, physical phenomena, such as consecutive reflections and alternations in direction of light, which enhance the vulnerability of the system during the scanning procedure, are likely to be eliminated.

Appendix A

Algorithms

A.1 Reconstruction Algorithm based on Diagonal Connection of Spectral Bands

```
1 % Tomographic Reconstruction Algorithm
2
3 clc
4 close all;
5 clear all;
6
7 % For the image slicing
8 [fimgname,pimgname] = uigetfile({'*.png'},'Select Images','Multiselect','on');
9
10 % Load excel files containing wavelength information for each pixel of the
11 % acquired spectral images
12 [fxlname,pxlname] = uigetfile({'*.xls;*.xlsx'},'Select Excel Files','Multiselect','on');
13 slicing(fimgname,pimgname,fxlname,pxlname);
14
15 % For the reconstruction of the spectral cube
16 [fimgname,pimgname] = uigetfile({'*.png'},'Select Slices','Multiselect','on');
17 prompt = {'Enter wavelength for reconstruction: '};
18 wavelength = inputdlg(prompt);
19 reconstruction(fimgname,pimgname,wavelength);
20
21 % Local functions
22
23 % This function performs the slicing of the acquired spectral images
24 function slicing(fimgname,pimgname,fxlname,pxlname)
25 wavelength=450:5:700;
26 for i = 1:size(fimgname,2)
27     % Read image
28     imageI{i} = imread([pimgname fimgname{1,i}]);
29     excel{i} = xlsread([pxlname fxlname],['pic' num2str(i)]);
30     % Slice image
31     h = size(imageI{i},2)/size(excel{i},1);
32     img = cell(size(excel{i},1),1);
```

```

33     for k = 1:size(excel{i},1)
34         img{k} = imageI{i}(:,(k-1)*h+1:k*h,:);
35         imwrite(img{k},['slice' num2str(wavelength(1,i)) '_' num2str(k) '.png']);
36     end
37 end
38 end
39
40 % This function performs the reconstruction of the spectral cube
41 function reconstruction(fimname,pimname,wavelength)
42 for i = 1:size(fimname,2)
43     % Read image
44     imageI{i} = imread([pimname fimname{1,i}]);
45 end
46 % Concatenate slices to construct the final image
47 fimg = cat(2,imageI{1,8},imageI{1,7},imageI{1,6},imageI{1,5},imageI{1,4},imageI{1,3},
48           imageI{1,2},imageI{1,1});
49 imwrite(fimg,['fimg' num2str(wavelength{1,1}) '.png']);
50 end

```

A.2 Reconstruction Algorithm based on Image Interpolation

```

1 % Reconstruction Algorithm based on Image Interpolation
2
3 clc
4 close all;
5 clear all;
6
7 % Read acquired spectral images
8 [fimname,pimname] = uigetfile({'*.png'},'Select Images','Multiselect','on');
9 for i = 1:size(fimname,2)
10     imageI{i} = imread([pimname fimname{1,i}]);
11 end
12
13 % Convert acquired spectral images to double precision
14 for i = 1:size(imageI,2)
15     imageId{i} = im2double(imageI{1,i});
16 end
17
18 % Load excel files containing wavelength information for each pixel of the
19 % acquired spectral images
20 [fxlname,pxlname] = uigetfile({'*.xls;*.xlsx'},'Select Excel Files','Multiselect','on');
21 for i = 1:size(fimname,2)
22     excel{i} = xlsread([pxlname fxlname],['pic' num2str(i)]);
23 end
24
25 % Assign wavelength bands to image pixels for every acquired spectral image
26 for i = 1:size(excel,2)
27     imageL{i} = myfun(excel{1,i});
28 end
29
30 % Matrices with spatial and spectral information for every pixel of every
31 % acquired spectral image

```

```

32 for i = 1:size(excel,2)
33     imageAcq{i} = cat(3,imageId{1,i},imageL{1,i});
34 end
35
36 % Delete matrices that are no longer needed
37 clear imageI imageId excel imageL
38
39 % Pre-allocate memory for the following arrays
40 % Array for the reconstructed spectral cube
41 table_2 = int16(zeros(251,2,2080*3096));
42 % If you want the reconstructed spectral cube to be a cell array then
43 % uncomment the following two rows
44 % table2c = squeeze(num2cell(table_2,[1 2]))';
45 % clear table_2
46 % Array for the acquired spectral cube
47 table_1 = zeros(size(imageAcq,2),2,2080*3096);
48 table1c = squeeze(num2cell(table_1,[1 2]))';
49 clear table_1
50
51 % Variable declaration
52 a1 = 0;
53 counter = 0;
54
55 % Temporary matrix
56 m1 = zeros(size(imageAcq,2),2);
57
58 % Construction of the acquired spectral cube
59 for r = 1:2080
60     for c = 1:3096
61         if a1 == 0
62             counter = c;
63         else
64             counter = a1 + c;
65         end
66         for i = 1:size(imageAcq,2)
67             m1(i,:) = [imageAcq{i}(r,c,1) imageAcq{i}(r,c,2)];
68             table1c{counter} = m1;
69         end
70         if c == 3096
71             a1 = a1 + c;
72         end
73     end
74 end
75
76 % Delete matrices and variables that are no longer needed
77 clear a1 counter imageAcq
78
79 % Variable declaration
80 a1 = 0;
81 counter = 0;
82
83 % Temporary matrix
84 inter_2 = zeros(251,2);
85
86 % Construction of the reconstructed spectral cube

```

```

87 for r = 1:2080
88     for c = 1:3096
89         if a1 == 0
90             counter = c;
91         else
92             counter = a1 + c;
93         end
94         lambda = table1c{counter}(:,2);
95         greyValue = table1c{counter}(:,1);
96         % Linear or spline interpolation to find grey values for every
97         % single wavelength between 450nm and 700nm
98         inter = round(interp1(lambda, greyValue, 450:1:700, 'linear'));
99         column = 450;
100        for row = 1:251
101            if inter(row) < 0
102                inter_2(row,:) = [0, column];
103            else
104                inter_2(row,:) = [inter(row), column];
105            end
106            column = column + 1;
107        end
108        table_2(:, :, counter) = int16(inter_2(:, :));
109        % If you want to use the cell array type for the reconstructed
110        % spectral cube then uncomment the following row
111        % table2c{counter} = int16(inter_2(:, :));
112        if c == 3096
113            a1 = a1 + c;
114        end
115    end
116 end
117 % If you use the cell array type for the reconstructed spectral cube, then
118 % uncomment the following row to convert the cell array to a 3D matrix
119 % table_2 = cat(3, table2c{:});
120
121 % Get the preferred reconstructed image
122 createImage();
123
124 % Local functions
125
126 % This function assigns wavelength to image pixels (for every acquired
127 % spectral image)
128 function [img] = myfun(file)
129 img = zeros(2080, 3096);
130 for k = 1:size(file, 1)
131     for q = 1:2080
132         img(q, k) = file(k, 2);
133     end
134 end
135 end
136
137 % This function creates the final reconstructed images
138 function [fimg] = createImage_v2(lambda, table_2, start_lambda, interp_step, imageSize)
139 idx = ceil((str2double(lambda{1,1}) - str2double(start_lambda{1,1}) + 1) / str2double(
    interp_step{1,1}));
140 ftable = permute(table_2(idx, 1, :), [1 3 2]);

```

```
141 pfimg = reshape(ftable,[str2double(imageSize{1,2}) str2double(imageSize{1,1})]);
142 fimg = uint8(pfimg);
143 end
144
145 % This function calls the above function "createImage_v2" to create the
146 % reconstructed image you want (e.g. image at 510nm, image at 586nm,etc..)
147
148 function createImage()
149 prompt1 = {'Enter the first wavelength of the scanning procedure: '};
150 startWavelength = inputdlg(prompt1);
151 prompt2 = {'Enter the preferred wavelength: '};
152 prefWavelength = inputdlg(prompt2);
153 prompt3 = {'Enter the step of interpolation you used for the reconstruction: '};
154 interpStep = inputdlg(prompt3);
155 prompt4 = {'Size 1: ', 'Size 2: '};
156 dlg_title = 'Size of image';
157 imgSize = inputdlg(prompt4,dlg_title,[1, length(dlg_title)+30]);
158 createImage_v2(prefWavelength,table_2,startWavelength,interpStep,imgSize);
159 end
```

Bibliography

- [1] D. A. Boas, C. Pitris, and N. Ramanujam. *Handbook of Biomedical Optics*, chapter 7, pages 131–164. Taylor & Francis, 2011.
- [2] T. Vo-Dinh. *Biomedical Photonics Handbook*, Taylor & Francis, 2010.
- [3] C. Balas, K. Rapantzikos. “*Hyperspectral imaging: potential in non-destructive analysis of palimpsests*”. *IEEE-International Conference on Image Processing (ICIP)*, page 11–14, September 2005. Available [here](#).
- [4] H. Kalluri, S. Prasad, and L. M. Bruce. “*Fusion of Spectral Reflectance and Derivative Information for Robust Hyperspectral Land Cover Classification*”. *IEEE Workshop on Hyperspectral Image and Signal Processing: Evolution in Remote Sensing*, 2009. Available [here](#).
- [5] D. Manolakis, D. Marden, and G. Shaw. “*Hyperspectral Image Processing for Automatic Target Detection Applications*”. *Lincoln Laboratory Journal*, 14(1), 2009. Available [here](#).
- [6] W. Li, S. Prasad, J. E. Fowler, and L. M. Bruce. “*Locality-Preserving Dimensionality Reduction and Classification for Hyperspectral Image Analysis*”. *IEEE Transactions on Geoscience and Remote Sensing*, vol. 50, no. 4, pp 1185–1198, April 2012. Available [here](#).
- [7] V. V. Tuchin. “*Handbook of Coherent-Domain Optical Methods: Biomedical Diagnostics, Environmental Monitoring, and Materials Science*”. Springer-Verlag GmbH, 2013.
- [8] Jiahui Pan. “*Image Interpolation using Spline Curves*”. MEC572 term paper, fall, 2003. Available [here](#).
- [9] Miklos Poth. “*Image interpolation techniques*”. 2nd Siberian-Hungarian Joint Symposium On Intelligent Systems, 2004. Available [here](#).
- [10] Robert G. Keys. “*Cubic Convolution Interpolation for Digital Image Processing*”. *IEEE Transactions on Acoustics, Speech, and Signal Processing*, Vol. ASSP-29, No.6, December 1981, pp.1153-1160.

-
- [11] Hsieh S. Hou, Harry C. Andrews. “*Cubic Splines for Image Interpolation and Digital Filtering*”. IEEE Transactions on Acoustics, Speech, and Signal Processing, Vol. ASSP-26, No.6, December 1978, pp.508-517.
- [12] S. S. Rifman, D. M. McKinnon. “*Evaluation of digital correction techniques for ERTS images*”. TRW Report 20634-6003-TV-02, 1974.
- [13] K. W. Simon. “*Digital Image Reconstruction and Resampling for Geometric Manipulation*”. LARS Symposia, paper 67, 1975. Available [here](#).
- [14] Erik H. W. Meijering. “*Spline Interpolation in Medical Imaging: comparison with other convolution-based approaches*”. Proceedings of EUSIPCO 2000, M. Gabbouj and P. Kuosmanen, Eds. The European Association for Signal Processing, Tampere, vol. IV, pp. 1989-1996, 2000.
- [15] I. J. Schoenberg. “*Contribution to the problem of approximation of equidistant data by analytic functions*”. Quart. Appl. Math., 4, pp. 112-141, 1946.
- [16] Michael Unser. “*Splines: A Perfect Fit for Signal/Image Processing*”. Proceedings of the SPIE International Symposium on Medical Imaging: Image Processing (MI'02), 4684, Part I, pp. 225-236, San Diego CA, 2002.
- [17] A. Tsapras, E. Terzakis, A. Makris, E. Papadakis, G. Papoutsoglou, E. Papagiannakis, C. Tsatsanis, E. Stathopoulos, and C. Balas. “*Hyper-Spectral Imaging for Skin Cancer Diagnosis in Mice*”. 6th European Symposium on Biomedical Engineering, June 2008.
- [18] C. I. Chang. “*Hyper-spectral Data Processing: Algorithm Design and Analysis*”. Wiley, 2013.
- [19] C. A. Glasbey, G. W. Horgan. “*Image Analysis for the Biological Sciences*”. Wiley, July 1995.
- [20] T. C. Poon, P. P. Banerjee. “*Contemporary Optical Image Processing with MATLAB*”. Elsevier Science, 2001.
- [21] J. W. Woods. “*Multidimensional Signal, Image, and Video Processing and Coding*”. Academic Press, 2011.
- [22] J. R. Parker. “*Algorithms for Image Processing and Computer Vision*”. Wiley, 2010.
- [23] M. Petrou, C. Petrou. “*Image Processing: The Fundamentals*”. Wiley, 2010.
- [24] Warren J. Smith. “*Modern Optical Engineering*”. McGraw Hill, 2000.
- [25] Dimitris G. Manolakis. “*Hyperspectral Imaging Remote Sensing: Physics, Sensors and Algorithms*”. Cambridge University Press, 2016.

- [26] Y. Garini, I. Young, and G. McNamara. *"Hyperspectral Spectral Imaging: Principles and Applications"*. 2006 International Society of Analytical Oncology, 2006. Available [here](#).
- [27] Di Wu, Da-Wen Sun. *"Advanced applications of hyperspectral imaging technology for food quality and safety analysis and assessment: A review – Part I: Fundamentals"*. Elsevier Science, 2013.
- [28] Nahum Gat. *"Imaging Spectroscopy Using Tunable Filters: A Review"*. SPIE, 2000.
- [29] Henrik Fabricius, Oliver Pust. *"Linear Variable Filters for Biomedical and Hyperspectral Imaging Applications"*. 2014. Available [here](#).
- [30] D. L. Bongiorno, M. Bryson, D. G. Dansereau, S. B. Williams. *"Spectral characterization of COTS RGB cameras using a linear variable edge filter"*. SPIE, 2013.
- [31] J. Y. Hardeberg, H. Brettel, F. Schmitt. *"Spectral characterization of electronic cameras"*. SPIE, 1998.
- [32] R. Vadivambal, Digvir S. Jayas. *"Bio-Imaging: Principles, Techniques, and Applications"*. CRC Press, 2016.
- [33] C. Balas. *"A Novel Optical Imaging Method for the Early Detection, Quantitative Grading and Mapping of Cancerous and Precancerous lesions of Cervix"*. IEEE-Transactions on Biomedical Engineering, vol. 48, No 1 pp. 96-104, 2001.
- [34] L. V. Wang and W. Hsin-L. *"Biomedical Optics Principles and Imaging"*. Wiley, 2007.
- [35] Alejandro Ribes Cortes. *"Multispectral Analysis and spectral Reflectance Reconstruction of Art Paintings"*. domain_other. Télécom ParisTech, 2003. English. pastel-00000761. Available [here](#). 5
- [36] Javier Hernández-Andrés, Javier Romero, Juan L. Nieves, Raymond L. Lee. *"Color and spectral analysis of daylight in southern Europe"*. Journal of the Optical Society of America A. Vol. 18, Issue 6, pp. 1325-1335, 2001.
- [37] Michael R. Hamblin, Pinar Avci, Gaurav K. Gupta. *"Imaging in Dermatology"*. Elsevier Science, 2016.
- [38] R. R. Anderson, J. A. Parrish. *"The optics of human skin"*. J Invest Dermatol 1981;77(1):13-9.
- [39] J. M. Schmitt, G. Kurmar. *"Turbulent nature of refractive-index variations in biological tissue"*. Optics Letters Vol. 21, Issue 16, pp. 1310-1312, 1996.
- [40] J. R. Weber, D. J. Cuccia, B. J. Tromberg. *"Modulated imaging in layered media"*. Conf Proc IEEE Eng Med Biol Soc 2006;Suppl:6674-6.

- [41] J. Zhao, H. Lui, D. McLean, H. Zeng. “*Real-time Raman spectroscopy for non-invasive skin cancer detection - preliminary results*”. Conf Proc IEEE Eng Med Biol Soc 2008;2008:3107-9.
- [42] Petya Pavlova, Ekaterina Borisova, Lachezar Avramov, Elmira Petkova and Petranka Troyanova (2011). “*Investigation of Relations Between Skin Cancer Lesions’ Images and Their Reflectance and Fluorescent Spectra, Melanoma in the Clinic - Diagnosis, Management and Complications of Malignancy*”, Prof. Mandi Murph (Ed.), ISBN: 978-953-307-571-6, InTech, Available [here](#).
- [43] Irving J. Bigio, Judith R. Mourant. “*Ultraviolet and visible spectroscopies for tissue diagnostics: fluorescence spectroscopy and elastic-scattering spectroscopy*”. Phys. Med. Biol. 42 (1997) 803-814.
- [44] Klaus Wolff, Richard A. Johnson, Arturo P. Saavedra. “*Fitzpatrick’s Color Atlas & Synopsis of Clinical Dermatology*”. McGraw-Hill Professional, 2016.
- [45] B. D’Alessandro, A. P. Dhawan. “*Multispectral Transillumination Imaging of Skin Lesions for Oxygenated and Deoxygenated Hemoglobin Measurement*”. Proceedings of IEEE EMBS (2010), pp. 6637-6640.
- [46] B. D. Montgomery, G. M. Sadler. “*Punch biopsy of pigmented lesions is potentially hazardous*”. Can. Fam. Physician 55(1), 24 (2009).
- [47] I. Diabele, I. Kuzmina, A. Lihachev, J. Kapostinsh, A. Derjabo, L. Valeine, J. Spigulis. “*Clinical evaluation of melanomas and common nevi by spectral imaging*”. Biomedical Optics Express 467, Vol. 3, No. 3, 2012.
- [48] B. Farina, C. Bartoli, A. Bono, A. Colombo, M. Lualdi, G. Tragni, R. Marchesini. “*Multispectral imaging approach in the diagnosis of cutaneous melanoma: potentiality and limits*”. Phys. Med. Biol. 45(5), pp. 1243-1254, 2000.
- [49] Estee L. Psaty, Allan C. Halpern. “*Current and emerging technologies in melanoma diagnosis: the state of the art*”. Clinics in Dermatology, Volume 27, Issue 1, pp. 35-45, 2009.
- [50] M. Herlyn. “*Lessons from melanocyte development for understanding the biological events in naevus and melanoma formation*”. Melanoma Research, 2000. 10(4): pp. 303-12.
- [51] F. Meier. “*Molecular events in melanoma development and progression*”. Frontiers in Bioscience: a Journal and Virtual Library, 1998. 3: pp. D1005-10.
- [52] G. Li, M. Herlyn. “*Dynamics of intercellular communication during melanoma development*”. Molecular Medicine Today, 2000. 6(4): pp. 163-9.